DESIGN AND FABRICATION OF BORON-CONTAINING III-NITRIDES BASED HIGH ELECTRON MOBILITY TRANSISTORS

A Thesis
Presented to
The Academic Faculty

by

Vinod Ravindran

In Partial Fulfillment
of the Requirements for the Degree
Doctor of Philosophy in the
School of Electrical and Computer Engineering

Georgia Institute of Technology
May 2013

DESIGN AND FABRICATION OF BORON-CONTAINING III-NITRIDES BASED HIGH ELECTRON MOBILITY TRANSISTORS

Approved by:

Professor P. Douglas Yoder,
Committee Chair
School of Electrical and Computer Engineering
Georgia Institute of Technology

Professor Russel D. Dupuis
School of Electrical and Computer Engineering
Georgia Institute of Technology

Professor Abdallah Ougazzaden,
Advisor
School of Electrical and Computer Engineering
Georgia Institute of Technology

Professor Nico F. Declercq
School of Mechanical Engineering
Georgia Institute of Technology

Professor David S. Citrin
School of Electrical and Computer Engineering
Georgia Institute of Technology

Date Approved: January 16th 2013

DEDICATION

To my parents,

my grandparents,

Diba, Sylvain,

and Margot.

ACKNOWLEDGEMENTS

This research has been done within the UMI Georgia Tech-CNRS lab in partnership with Thales. It was both funded by the Agence Nationale de la Recherche et de la Technologie (ANRT) through a *CIFRE* contract, and by the Agence Nationale de la Recherche (ANR) through the *GABORE* project (in partnership with Thales III-V lab, Marcoussis, and the Institut d'Electronique de Microélectronique et de Nanotechnologie, or IEMN, Lille).

First, I would like to thank my two advisors, Prof. Abdallah Ougazzaden and Dr. Marie-Antoinette di Forte-Poisson, for giving me the opportunity to conduct successfully this Ph.D in an international research environment connecting both academia and industry.

My sincere thanks also go to members of my committee: Prof. P. Douglas Yoder, Prof. David S. Citrin, Prof. Russel D. Dupuis and Prof. Nico F. Declercq. They have been extremely helpful, supportive, even with their sharp questions! I am indebted to Prof. P. Douglas Yoder, who helped me at the very beginning of my Ph.D. with simulations, but also at the very end to process paperwork overseas.

I am also extremely grateful to our partners of the IEMN, especially Prof. Ali Soltani. Ali has given me an unwavering support, not only as a seasoned researcher, but also as a friend. Nothing would have been possible without his help.

I also take the opportunity to thank Prof. Jean-Marc Raulot for all his *ab initio* calculations and insightful discussions.

This Ph.D thesis has represented a significant achievement and played a pivotal role in my short adult life. Beyond science, it has been a once-in-a-lifetime chance

to learn about myself, and test once more my determination. Yet, I cannot imagine how I could have done it without the help of so many friends.

First, I do not forget all the Ph.D. students who crossed my path at Georgia Tech Lorraine: Mohamed, Frédéric, Wui Hean, Konstantinos, Sarah, Peter (and his late *Mme Peugeot*), Renaud, and many more. Most importantly, my greatest supporter was Damien. He has been a great friend, spent endless nights debating with me and helped me so much for this Ph.D. thesis.

Very close, but geographically separated (a few meters), post-doctorates also became good friends. I would like to thank especially Malek for the countless guidance counseling sessions. Thank you also Matthieu (or Prof. Bloch) to show us what a virtuous path can be...

I would like also to acknowledge the staff of Georgia Tech Lorraine for all their help: Sandrine, Francis, Jean-Jacques, Christine, and many others that are too many to be acknowledged here.

I am deeply grateful to my parents, for everything they did in their life solely for our well-being, and for their support all along these years of studies. I also want to thank my sister Diba, and her husband Sylvain, for their useful advice towards a happy life. Finally, I also want to dedicate this thesis to my grandparents who, back in India, always viewed education as a priority.

Nota Bene: Even though she got on board later than others, I was extremely fortunate to meet Margot in the course of my Ph.D. to accompany me until the end of this degree.

TABLE OF CONTENTS

DEDICATION . . . . . **iii**

ACKNOWLEDGEMENTS . . . . . **iv**

LIST OF TABLES . . . . . **x**

LIST OF FIGURES . . . . . **xi**

ACRONYMS . . . . . **xviii**

SUMMARY . . . . . **xxi**

I INTRODUCTION **1**

II NITRIDE MATERIALS AND HIGH ELECTRON MOBILITY TRANSISTORS **7**

2.1 Nitride materials 8

2.1.1 Crystal structure 9

2.1.2 Growths and Substrates 15

2.1.3 Pseudomorphic growth of nitride compounds 20

2.2 *High electron mobility transistors* with III-N alloys 20

2.2.1 The HEMT and III-V materials 20

2.2.2 The AlGaN/GaN HEMT 22

2.2.3 Growth direction and Polarity 24

III GROWTH AND CHARACTERIZATION OF HEMT STRUCTURES 26

3.1 Growth of semiconductor devices 26

3.1.1 The MOVPE principle 26

3.1.2 The MOVPE machine 26

3.2 Characterization of semiconductor structures 28

3.2.1 The AFM 28

3.2.2 The XRD 30

3.2.3 SIMS analysis 31

3.2.4 The PL setup 32

3.2.5 PL measurements on standard substrates 36
3.2.6 The Transmission Electron Microscopy 39
3.2.7 The Scanning Electron Microscopy 40
3.3 Electrical characterization of HEMTs 43
3.3.1 Hall effect 43
3.3.2 The Van der Pauw technique 44
3.3.3 Capacitance-voltage measurements 45
3.3.4 Mercury probe measurements 47

IV BORON-BASED NITRIDE ALLOYS 48

4.1 Introduction to boron-based nitrides 48
4.2 Growth of BGaN 51
4.3 Structural analysis of BGaN layers 52
4.4 Electrical characterization of BGaN 57

V SIMULATION OF HEMT DEVICES AND DUAL-PURPOSE BGAN HEMT 59

5.1 The Schrödinger-Poisson equation and *ab initio* calculations 59
5.1.1 Solving Schrödinger's equation 60
5.1.2 Solving Poisson's equation 63
5.1.3 The Schrödinger-Poisson *solver* 66
5.1.4 Adding polarization to Poisson's equation 66
5.2 Polarization study in nitrides 68
5.3 Simulation of AlGaN/GaN HEMT 70
5.4 AlGaN/GaN HEMT with BGaN thin layers 74
5.4.1 Limiting leakage in the buffer 74
5.4.2 Implementing BGaN 77
5.4.3 Polarization in BGaN 78
5.4.4 Dual-purpose BGaN layers for AlGaN HEMTs 79

VI EXPERIMENTAL WORK: OPTIMIZATION OF HEMT GROWTH 84

6.1 Growth of thick AlGaN layers 84

6.2 Standard AlGaN/GaN HEMT growth (first HEMT campaigns) . . . 87

6.2.1 Growths performed 87

6.2.2 Structural and morphological results 88

6.2.3 Device results 92

6.2.4 Regrowth interface 94

6.3 Introduction of AlGaN in the buffer (second HEMT campaigns) . . 95

6.3.1 XRD analysis 96

6.3.2 AFM analysis 98

6.3.3 Capacitance-voltage measurements 99

6.3.4 SIMS analysis 101

6.3.5 Device results 102

6.4 Reproducibility of standard HEMTs growth (third HEMT campaign) 102

6.5 Standard HEMTs growth on following series 105

VII EXPERIMENTAL WORK: BORON HEMT STUDY 107

7.1 Study of thick BGaN layers 108

7.1.1 Growth of BGaN layers 108

7.1.2 Hall measurements on BGaN layers 108

7.1.3 Optical characteristics of BGaN layers 109

7.2 Employ of thin BGaN layers 112

7.2.1 Growths of Series 5 and 6 112

7.2.2 Review of structural quality of Series 5 and 6 113

7.2.3 BGaN as a compensation layer 117

7.2.4 BGaN as back-barrier 118

7.2.5 TEM measurements 119

7.3 Device results 122

7.3.1 Series 7 - Introduction of a GaN cap layer 122

7.3.2 Processing of devices 123
7.3.3 Characterization and preliminary results 125
7.3.4 Evidence of the effect of BGaN layers on microwave performance of conventional AlGaN/GaN HEMT 128

VIII CONCLUSION 134

8.1 Contribution 134
8.2 Perspectives 136
8.2.1 Growth optimization 136
8.2.2 Choice of substrate 137
8.2.3 Characterization of BGaN 137
8.2.4 New designs 138

APPENDIX A — LIST OF HEMTS GROWN 140

APPENDIX B — AB INITIO CALCULATIONS PERFORMED ON NITRIDE COMPOUNDS 146

REFERENCES 150

VITA 161

LIST OF TABLES

1 Comparison of different semiconductor materials for high-power/-frequency applications. 9

2 Physical constants of nitrides used for the calculation of the polarization. Parameters e_{31} and e_{33} are the piezoelectric coefficients, C_{13} and C_{33} are the elastic constants and P_{sp} is the spontaneous polarization. 68

3 Specifications for a Fe-doped semi-insulating GaN standard templates on sapphire substrate (source: *Lumilog*). 87

4 Data derived from Hall measurements on Series 1 samples. No structure exhibits distinctive marks of a HEMT behavior with a well-confined gas. 93

5 AFM measurements on Series 5 (all BB/CL layers comprise 1% of boron). 114

6 AFM measurements on Series 6 (all BB layers comprise 1% of boron). 115

7 Data derived from CV measurements using mercury probes and comparing the standard AlGaN/GaN structure T572 to structures with a BGaN compensating layers (all BB/CL layers comprise 1% of boron). 118

8 Data derived from CV measurements using mercury probes and comparing the standard AlGaN/GaN structure T572 to structures with a BGaN back-barriers in Series 5 (all BB layers comprise 1% of boron). 119

9 Data derived from CV measurements using mercury probes and comparing the standard AlGaN/GaN structures T602 and T603 to structures with a BGaN back-barriers in Series 6 (all BB layers comprise 1% of boron). 120

10 Data derived from Hall measurements, under illumination, on processed structures of Series 5 (all BB layers comprise 1% of boron). . . 126

11 Data derived from Hall measurements, under illumination, on processed structures of Series 6 (all BB layers comprise 1% of boron). . . 127

12 Data derived from Hall measurements, under illumination, on processed structures of Series 7 (all BB layers comprise 1% of boron). . . 128

LIST OF FIGURES

1 Application of millimeter waves for wireless local area networks thanks to interference free channels. Long distance communications are hindered by atmosphere absorption at these wavelengths (water at 22.235 GHz and 183.3 GHz, and the oxygen lines at 60 GHz and 118.75 GHz), hence allowing these networks to work independently and without interfering with either each other or with satellite communications [1] . 2

2 Use of semiconductor materials for wireless transmissions (inspired from [2]). GaN materials are at the crossroads between high frequencies and high energies applications. Their potential for millimeter-wave range remains untapped. 4

3 Contribution of the different dipole moment in the generation of a spontaneous polarization in GaN materials when the structure is strained. 10

4 Orientations in nitrides with *a*- and *m*-planes projected on the (0001) basal plane (inspired from [3]) 11

5 The wrtzite structure of nitride compounds, example of GaN - schematic drawing of the wrtzite crystal structure with *Ga-face* on top (left) and the wrtzite unit cell associated (right). 11

6 The polarization in nitride compounds - spontaneous polarization (left) and the addition of the piezoelectric polarization (right). 12

7 Strain and stress components for a typical configuration of the top layer of a HEMT structure in a wrtzite crystal. 14

8 The band diagram of GaN (extracted from [4]). 16

9 Band-edge structure near k=0 for GaN. 16

10 Lattice parameters and thermal characteristics of a number of the prospective substrate materials for nitride growth and their lattice mismatch with GaN (extracted from [3]). 18

11 Growth of III-N material on a sapphire substrate (inspired from [5]) . 19

12 Tilt and twist of grains when grown on lattice mismatched substrate (inspired from [6]) 19

13 Epitaxial growth of a tensile/compressive strained or unstrained layer. 21

14 An example of related art technology - InP-based III-V HEMT with the associated conduction band profile (inspired from [7]). 22

15 Nitride HEMT - Polarization and the 2DEG. 23

16 Ga-face and N-face growth of GaN 25

17 The principle of MOVPE - here illustrated for the epitaxy of GaN layers with N_2 as the carrier gas. 27

18 Schematic of the T-shape reactor used in our lab for the growth of nitrides. 28

19 Principle of AFM (inspired from [8]) 29

20 Description of the localization of AFM image measurements on a typical quarter of a disk sample made out from a diced substrate. 30

21 X-ray diffraction measurements principle (inspired from [8]) 31

22 The principle of Secondary Ion Mass Spectroscopy. 32

23 Schematic of the photoluminescence setup used in our lab. 35

24 Operating mechanism schematic of the LN_2 Janis Research VNF-100 cryostat (credit to Chris Bishop) 36

25 PL measurements, using a 244 nm laser beam, on a standard semi-insulating GaN Fe-doped substrate on sapphire (STINS GaN09542) at both room and low (77K) temperatures, from 300 to 700 nm. The GaN peak is observed in both figures along with the yellow luminescence characteristic of nitrides. At low temperature, there are 3 clearly visible peaks (labelled A, B and C). The major peak is related to the GaN and peaks B and C are probably related to impurities or donor- or shallow-acceptor bound excitons. 38

26 TEM instrument *Jeol 2200FS* at LPN (left), schematic views of its microscopy principle (center) and illustration with a HAADF imaging (right) (courtesy of LPN). 41

27 Schematic of SEM principle with constituting electron optics (inspired from [9]). 42

28 Schematic of the Hall effect occurring in semiconductor samples under a magnetic field (B) (Lorentz force components are represented for the case of electrons). 43

29 Van der Pauw method. 45

30 Principle of capacitance-voltage measurements. 46

31 Bandgap versus lattice parameter with representation of usual nitrides compounds (straight lines) and boron nitride materials (dashed lines). Boron alloys-related branches are represented only for illustration and are not based on concrete results. The bowing of BGaN translates results obtained in [10]. 50

32 (a) Sudden degradation of the surface morphology observed with *in-situ* reflectance for a total pressure of 450 Torr in the reactor at different values of the TEB/III ratio. (b) Optimal thickness evolution as function of the TEB/III ratio for a total pressure of 100 or 450 Torr in the reactor [11]. 52

33 BGaN boron composition (%) versus TEB/III ratio (%) for two different pressures in the reactor [12]. 53

34 (a): HAADF-STEM picture of a 400 nm thick BGaN layer containing 0.7% of boron. (zone axis is $< 1120 >$) and (b) 2D Fourier transform pattern of the HAADF-STEM image in (a). The wrtzite reflections as well as the zinc-blende one are present. The specific 111 ZB is circled in red. (c) The BGaN layer image reconstructed by mean of inverse Fourier transform evidences zinc-blende insertions in the BGaN material [13]. 54

35 HAADF-STEM picture of a 1 mm thick BGaN layer containing 1.7% of boron [13]. 55

36 (a) HAADF-STEM picture of a single cluster in a 1000 nm thick BGaN layer containing 1.7% of boron (the thin foil was prepared along the $< 1120 >$ zone axis), (b) diffraction pattern of the image. Wrtzite pattern as well as zinc-blende are present, (c) inverse Fourier transform image realized with the specific wrtzite spots 1100 and 1120 and (d) inverse Fourier transform picture obtained with the cubic 111 and 220 spots [13]. 56

37 Electrical characterization of 600 nm thick BGaN layers on AlN template: resistivity as function of the boron composition. The inset shows the measured density of carriers and the mobility as function of the boron composition [14]. 58

38 Iteration process for the Schrödinger-Poisson *solver*. 67

39 Polarization evolution in an AlGaN/GaN heterostructure. 69

40 Polarization evolution in an InGaN/GaN heterostructure. 70

41 Simulation of an $Al_{0.25}GaN_{0.75}$/GaN structure, with 0.25 of Al in barrier, for different thicknesses doping level of the barrier. 71

42 Simulation of the confinement of an AlGaN/AlN/GaN/InGaN/GaN HEMT structures with different InGaN back-barriers - the maximum of the density profiles corresponds to the AlN/GaN interface (based on [15]). 72

43 Simulation of the confinement of an AlGaN/AlN/GaN/InGaN/GaN HEMT structures with different InGaN back-barriers - the maximum of the density profiles corresponds to the AlN/GaN interface (based on [15]). 73

44 Simulation of the confinement of AlGaN/GaN HEMT structures with different InGaN back-barriers - depth limits for 90% or 99% of the electrons. 74

45 Simulation of an AlGaN/GaN HEMT with an InGaN back-barrier. . 76

46 Polarization evolution in a BGaN/GaN heterostructure. 79

47 Examples of AlGaN/GaN HEMT with and without a BGaN BB employed for simulations: (a) thin BGaN BB, (b) thick BGaN BB and (c) graded BGaN BB. 80

48 Conduction band profile and carriers density for AlGaN/GaN HEMTs with and without a thin BGaN BB from the top surface to the buffer. In (b), the raise of the conduction band with the BGaN BB offers an electrostatic barrier to electrons that reduces the spreading of the electrons in the 2DEG as illustrated in (a). The grey-colored area corresponds to the thin BGaN layer which also represent a resistive barrier to electrons, hence preventing leakage in the buffer. 81

49 Conduction band profile and carriers density for AlGaN/GaN HEMTs with and without a thick or graded BGaN BB from the top surface to the buffer. In (b), raises of the conduction band with BGaN BB offer an electrostatic barrier to electrons that reduces the spreading of the electrons in the 2DEG as illustrated in (a). The grey-colored area corresponds to the thick/graded BGaN layer which also represent a resistive barrier to electrons, hence preventing leakage in the buffer. . 82

50 (a) Incorporation efficiency of aluminium in the solid phase as function of V/III ration for constant TMAl/III ratio equal to 25%. (b) Al-mole ratio in the solid phase (x) as function of TMAl/III ratio for a V/III ratio of 900. 86

51 Series 1: standard AlGaN/GaN HEMT structures ; T334 (left) and T335 (right). 88

52 Series 1: HEMT structures comprising BGaN layers ; T336 (left), T337 (center) and T344 (right). 89

53 Morphology of the structure T335. (a) AFM image on a $5\mu m \times 5\mu m$ window showing the good morphological quality and (b) SEM image of the surface where distinctive holes, known as V-defects, can be observed (SEM performed at the IEMN). 90

54 Schematic of V-defects originating from a dislocation core [16]. 91

55 Morphology of structure T336 containing BGaN: (a) the AFM image on a $5\mu m \times 5\mu m$ window shows a degraded surface composed of 10-100 nm large grains ; (b) scan $\omega - 2\theta$ XRD measurement exhibiting the absence of thickness-related interference fringes around the diffraction peak for AlGaN. 92

56 *Spirou* mask used for electrical characterizations with its schematic (left) and a SEM picture obtained of the mask deposited on a HEMT (right). 92

57 SIMS profiles of impurities concentrations in the T334 structure (measurements were done at a partner lab named GEMaC - CNRS Bellevue, France). In a dynamic mode, the sputtering time translates into depth and the number of counts per second of secondary ions represents their relative density at a given depth 3.2.3. A distinctive spike of Si is observed at the regrowth interface. 94

58 (a) X-ray diffraction spectrum of HEMT structure AlGaN/GaN T406 ; (b) X-ray diffraction spectrum of HEMT structure AlGaN/GaN/AlGaN T408 ; (c) reciprocal-space mapping (RSM) along 114 of HEMT structure AlGaN/GaN/AlGaN T403. The alignement of the different areas corresponding the different layers implies that all layers are fully strained on GaN. 97

59 AFM measurements on Series 2 structures with a $5\mu m \times 5\mu m$ window. 98

60 (a) C-V measurements on structure T406 at different frequencies in 10-400kHz range ; (b) Zoom view of the residual capacitance in the buffer ; (c) C-V measurements on structure T408 at different frequencies in 10-400kHz range ; (d) Carrier density deduced from C-V measurements of structure T406. 100

61 (a) SIMS depth profiles of HEMT structure AlGaN/GaN T406 with caesium primary ion beam ; (b) SIMS depth profiles of HEMT structure AlGaN/GaN/AlGaN T408 with caesium primary ion beam. 101

62 (a) Compared 2theta/omega X-ray diffraction spectrum of HEMT structures AlGaN/GaN T406, T445, T449 and T450 ; (b) AFM measurements on structure T445 with a $5\mu m \times 5\mu m$ window showing a very smooth surface roughness of 1nm. 103

63 (a) C-V measurements on structure T445 at different frequencies in 10-400kHz range ; (b) Carrier density deduced from C-V measurements of structure T445 ; (c) C-V measurements on structure T448 at different frequencies in 10-400kHz range ; (d) Carrier density deduced from C-V measurements of structure T448. 104

64 (a) C-V measurements on structure T449 at different frequencies in 10-400kHz range ; (b) Carrier density deduced from C-V measurements of structure T449 ; (c) C-V measurements on structure T450 at different frequencies in 10-400kHz range ; (d) Carrier density deduced from C-V measurements of structure T450. 105

65 Resistivity in BGaN and AlGaN thick layers as function of boron or aluminium incorporation, respectively. 109

66 Photoluminescence at room temperature of BGaN structures of the first batch. 110

67 Photoluminescence at room temperature of BGaN structures of the second batch. Dark arrows point at the main exciton transition of GaN and magenta arrows point at the peak corresponding to BGaN. 112

68 SEM measurements on Series 6 structures with $100\mu m \times 100\mu m$ and $5\mu m \times 5\mu m$ windows, respectively. 115

69 XRD and RSM measurements on Series 6 structures. 116

70 STEM-HAADF measurements on structures T574 and T575 comprising a BGaN BB at a distance from the channel of 10 or 20 nm, respectively. The theoretical distance from the channel of the BGaN BB is displayed in red. As the BGaN BB are too thin, they are not visible since the contrast limit is reached. 121

71 Schematic principle of surface traps formation. 123

72 FIB cross-sectional view of T-shaped gates manufactured with foot print size of (a) 100 nm and (b) 250 nm. 125

73 Current-Electric Field characteristics between two electrodes performed on GaN buffer layer without and with BGaN BB (GaN (40nm)/$B_{0.01}Ga_{0.99}N$ (1nm)/GaN buffer layer). 129

74 $I_{DS}(V_{GS})$ measurements on DC and pulsed regimes on a device without (a,b) and with (c,d) an ultra-thin BGaN BB barrier. (a,c) DC measurements and pulsed with quiescent point at (V_{GS},V_{DS}) : (0 V, 0 V); (b,d) DC measurements and pulsed with quiescent point at ((V_{GS},V_{DS}): (0 V, 0 V), (-8 V, 0 V), and (-8 V, 15 V). 132

75 Bandgap versus lattice parameter - BInGaN. 139

76 Structures of SERIES 2. 141

77 Structures of SERIES 3. 142

78 Structures of SERIES 5 - First Part. 142

79 Structures of SERIES 5 - Second Part. 143

80 Structures of SERIES 6. 144

81 Structures of SERIES 7. 145

82 Relevant elastic constants, Born effective charges and piezoelectric constants calculated using the PAW method with either LDA or GGA for GaN. Data are compared to results reported by Shimada *et. al.* [17], Karch *et. al.* [18] and Kim *et. al.* [19]. 147

83 Relevant elastic constants, Born effective charges and piezoelectric constants calculated using the PAW method with either LDA or GGA for AlN. Data are compared to results reported by Shimada *et. al.* [17], Karch *et. al.* [18] and Kim *et. al.* [19]. 148

84 Relevant elastic constants, Born effective charges and piezoelectric constants calculated using the PAW method with either LDA or GGA for BN. Data are compared to results reported by Shimada *et. al.* [17], Karch *et. al.* [18] and Kim *et. al.* [19]. 149

ACRONYMS

f_t	Cut-Off Frequency
f_{max}	Maximum Oscillation Frequency
I_{DS}	Drain-Source Current
L_G	Gate Length
L_{GD}	Gate-Drain Length
$L_{G,eff}$	Effective Gate Length
LN_2	Liquid Nitrogen
R_a	Arithmetic Average Roughness
R_q	Root Mean Square Roughness
V_{DS}	Drain-Source Voltage
V_{GS}	Gate-Source Voltage
v_{eff}	Effective Electron Velocity
2DEG	Two-Dimensional Electron Gas
AC	Alternative Current
AFM	Atomic Force Microscopy
Al	Aluminium
AlN	Aluminium Nitride
B	Boron
BB	Back-Barrier
BN	Boron Nitride
C-V	Capacitance-voltage
DC	Direct Current
DH-HEMT	Double-Heterostructure High Electron Mobility Transistor
EDX	Energy Dispersive X-ray
FDM	Finite Difference Method

FET	Field-Effect Transistors
FIB	Focused Ion Beam
Ga	Gallium
GaAs	Gallium Arsenide
GaN	Gallium Nitride
HAADF	High Angle Annular Dark Field
HEMT	High Electron Mobility Transistor
I-V	Current-voltage
In	Indium
InN	Indium Nitride
InP	Indium Phosphide
MBE	Molecular Beam Epitaxy
MESFET	Metal-Semiconductor Field-Effect Transistors
MMIC	Monolithic Millimiter-wave Integrated Circuits
MOCVD	Metal Organic Chemical Vapor Deposition
P.A.E.	Power Added Efficiency
PL	Photoluminescence
RF	Radio-Frequency
RMS	Root Mean Square
RSM	Reciprocal Space Mapping
SEM	Scanning Electron Microscopy
SIMS	Secondary Ion Mass Spectrometry
SiC	Silicon Carbide
TD	Threading Dislocation
TEM	Transmission Electron Microscopy
TLM	Transmission Line Method
TRM	Through-Reflect-Match

VCSEL	Vertical Cavity Surface Emitting Laser
XRD	X-Rays Diffraction
ZnO	Zinc Oxide

SUMMARY

GaN-based HEMTs are among the most promising candidates for high-power and high-frequency applications; a niche for millimeter-wave technologies. Nitride materials indeed outperform other mainstream III-V materials (InP or GaAs) because of several properties, including wider bandgaps, high peak and saturation velocities, large breakdown voltages, together with good thermal conductivities. Nonetheless, the state-of-the-art of nitrides is not yet industrially mature to exploit the entire millimeter-wave range.

A way to push further performance is to develop innovative designs, notably by exploring novel materials. The purpose of this research was therefore to investigate the use of boron-containing III-nitrides in *high electron mobility transistors* (HEMTs).

The study was first conducted theoretically, through solving the Schrödinger-Poisson equation. Key parameters and relevant equations were derived to implement BGaN materials in our simulations. A GaN/ultrathin-BGaN/GaN heterojunction was showed to provide an electrostatic barrier to electrons and to improve the confinement of the two-dimensional electron gas. GaN back-barrier layers happen to limit leakage in the GaN buffer thanks to two effects: (i) a polarization-induced band discontinuity and (ii) a resistive barrier originating from excellent insulation properties of BGaN.

The study was then, experimentally, several growth campaigns were carried out that led to the fabrication of devices. First, we confirmed the key characteristics of BGaN materials by electrical and optical measurements. Second, we demonstrated the evidence of a significant enhancement of performance of standard AlGaN/GaN

structures by the introduction of a BGaN layer in the buffer layer.

Compared to conventional AlGaN/GaN HEMTs, structures grown with BGaN back-barriers showed a significant improvement of static performances, transport properties, and trapping effects involving a limited current collapse in dynamic regime.

CHAPTER I

INTRODUCTION

Power amplification has been critical to the widespread adoption of landline phone communications. It is now an essential component of wireless transmissions, which have become a prominent part of our everyday lives over the last decades. The development of power amplifiers started a century ago with vacuum tubes[1], followed by the advent of the transistor that revolutionized all these technologies, and led to the rapid development of computers[2].

Solid-state power devices, such as semiconductor transistors, are now crucial to keep up with current technological standards, which require smaller size, reduced cost, and better power consumption. They have allowed the telecom industry to thrive, and they are currently employed for diverse purposes [21]. Research now has a great interest in high-power and high-frequency devices as demand grows for millimeter-wave applications that are ranging from 30 to 300 GHz, as illustrated in Fig 1. High-speed wireless local area networks, automotive and space communications, or *last-mile* wireless links require solid-state amplifiers for optimal power efficiency and minimum size.

This research focuses primarily on a certain type of field effect transistor known as *high electron mobility transistor* (HEMT), a core component of *monolithic millimeter-wave integrated circuits* (MMICs), which plays a major role in solid-state amplification and high-frequency circuits. The specificity of HEMTs is the use of a heterointerface

[1]Wireless transmissions already existed before, we can mention spark-gap transmitters that use to prevail for maritime communications.

[2]One of the first electronic computers was the ENIAC built in 1946 with about 18,000 triodes, and which consumed 178 kW [20].

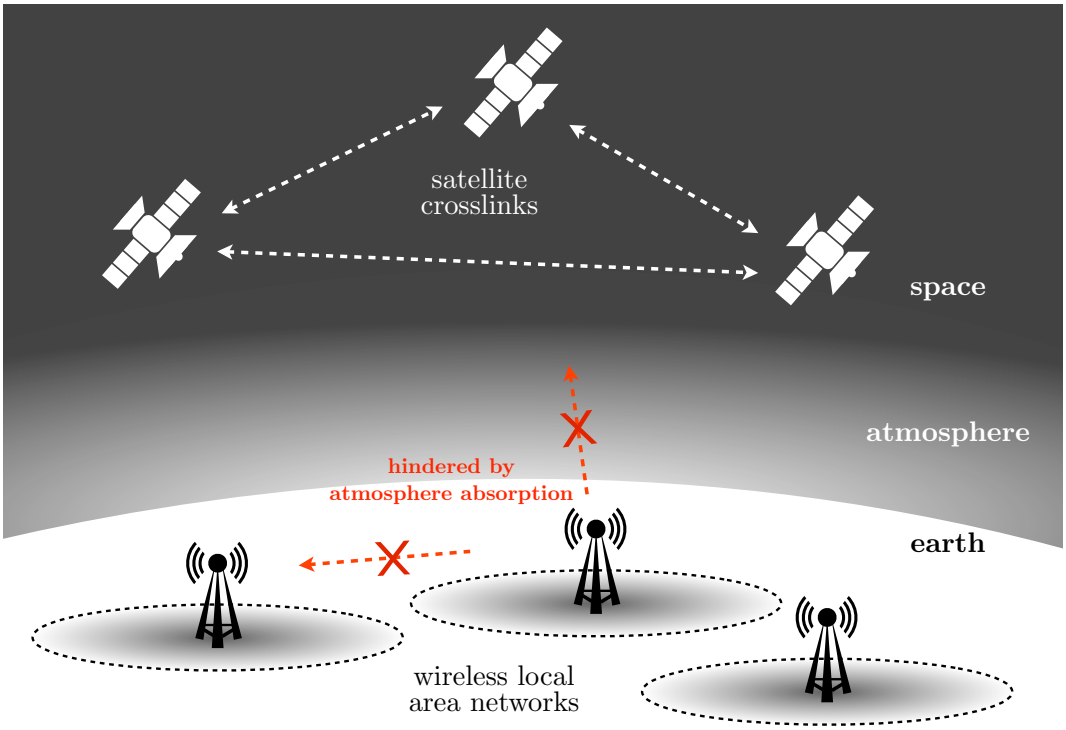

Figure 1: Application of millimeter waves for wireless local area networks thanks to interference free channels. Long distance communications are hindered by atmosphere absorption at these wavelengths (water at 22.235 GHz and 183.3 GHz, and the oxygen lines at 60 GHz and 118.75 GHz), hence allowing these networks to work independently and without interfering with either each other or with satellite communications [1]

leading to the existence of a fixed two-dimensional electron gas (2DEG). The semiconductor components of HEMT structures has to be realized by epitaxy. Most of the realizations today are based on III-V compounds because of their superior features compared to other semiconductor materials classically used in microelectronics, such as silicon [22]. Specifically, nitride semiconductors, or III-N compounds, are currently attracting most of the attention because of properties that make them more suitable for high-power and high-frequency applications, including wide bandgap, high peak and saturation velocities, large breakdown voltages, and better thermal conductivities (see Section 2.1.0.1) [23].

The transistor structure that exploits the most of all these characteristics is the GaN-based HEMT, which has the monopoly for microwave-domain applications [23]. Most transistors of this type developed so far were aimed at applications below 30 GHz, but researchers' objective is to go above and reach the millimeter-wave frequencies (see Fig. 2[3]). As for other HEMTs, nitride structures possess a 2DEG, which arises at the heterointerface between AlGaN and GaN [24]. This 2DEG is a direct consequence of large polarization effects occurring in nitride materials. Compared to conventional III-V HEMTs (based on InP or GaAs), it does not require any donor layer that would degrade the mobility through impurity scattering. HEMTs particularly stand out for their ability to handle high power densities up to 30-40 W/mm [25] (compared to 3-4 W/mm in GaAs [26]) while achieving record cut-off frequencies above 300 GHz to date [27].

Although conventional AlGaN/GaN HEMTs have been extensively studied, there are still linearity issues related to electron trapping either in the buffer or the passivation layer. Moreover, the scientific community is now looking for ways to further

[3] *Nota*: HFET (or heterojunction field effet transistor) usually corresponds to a heterostructure where transport occurs in a doped material.

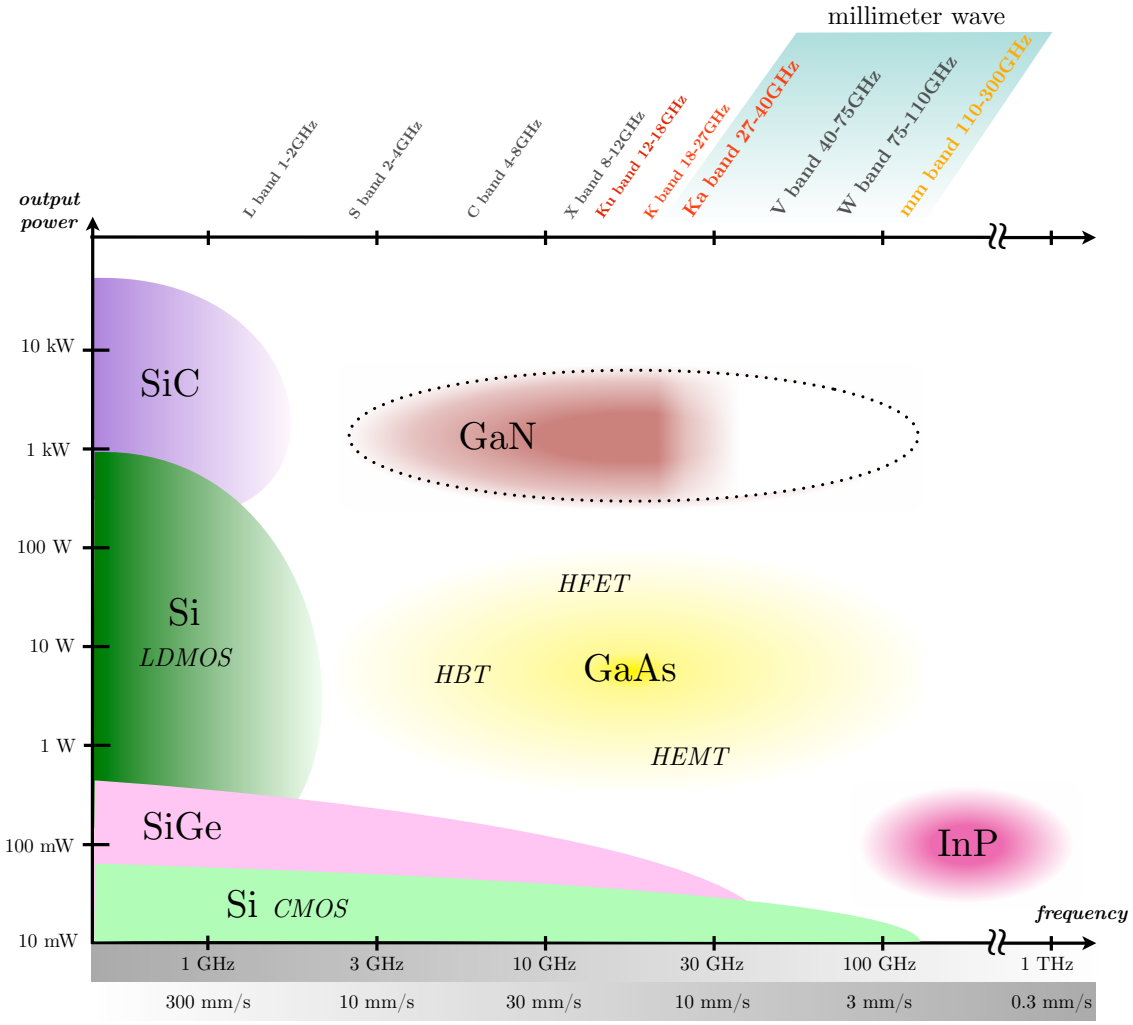

Figure 2: Use of semiconductor materials for wireless transmissions (inspired from [2]). GaN materials are at the crossroads between high frequencies and high energies applications. Their potential for millimeter-wave range remains untapped.

increase the maximum frequency and the power-handling capability to reach new microwave bands (e.g. K_a band [28]) or reduce the size of antennas, respectively. Such advances have been possible with the introduction of new design, process or manufacturing technologies such as field plates, mushroom-shaped gates, passivation, etc. [23]. One strategy to enhance performances is to increase the mobility and lower scattering effects encountered by electrons of the 2DEG, or even improve the confinement electrons in the channel. Simultaneously, the resistivity should be increased in the buffer to prevent leakage of carriers from the 2DEG. Consequently, research continues looking for innovative designs; in addition to the AlGaN/GaN HEMT structure, alternate designs have been reported such as AlGaN/InGaN/GaN double-heterojunctions [29], AlGaN/AlN/GaN HEMTs [30], AlN/GaN HEMTs [31], N-face grown GaN/AlGaN HEMTs [32], or InAlN/GaN HEMTs [33], which show very promising results [34].

In the present work, we propose to investigate the use of boron-containing III-nitride materials in nitride HEMTs to improve performance. The study is conducted both theoretically, through simulations, and experimentally, with the growth of semiconductor materials for the fabrication of devices.

This dissertation is organized as follows.

In Chapter 2, we first introduce nitride materials and their singular properties as well as their growth. Then, we briefly review the principles of HEMT and the specific principle of operation of AlGaN/GaN structures. The role played by polarization in nitrides is emphasized at it plays a major role in the appearance of a 2DEG.

In Chapter 3, we present metal-organic vapor phase epitaxy (or MOVPE) growths performed at our lab as well as major tools (such as X-ray diffraction, atomic force microscopy, etc.) critical for the characterization of structures.

In Chapter 4, we focus on boron-based nitride compounds and how they can be used for band engineering. We then review past results obtained by our group,

which support our research, in particular the observation of a bandgap bowing in BGaN materials and the appearance of a high resistivity for little boron alloying. In addition, a structural analysis of this ternary alloy allow us to precisely see the behavior of boron within the GaN matrix.

The theoretical and experimental contributions of this thesis are described in subsequent chapters. Chapter 5 discusses simulations of nitride HEMT structures. We first review the theoretical background and present the solver used for determining band structures. We then review results obtained on standard AlGaN/GaN structures and later investigate the employ of BGaN layers in conventional nitride HEMT to help confining carriers in the 2DEG.

Experimental work regarding standard AlGaN/GaN structures, grown for the first time at our lab, is discussed in Chapter 6. Several campaigns of structures were grown to assess our capability to achieve device quality and its reproducibility based on morphological and structural analyses and electrical characterizations.

In Chapter 7, we present research aimed at applying experimentally innovative designs based on BGaN layers. We focus on characterizations of bulk BGaN layers to corroborate key parameters used for our earlier simulation study. We then review results from several growth campaigns introducing BGaN layers in the buffer of conventional AlGaN/GaN HEMT through characterization and device measurements. Several parameters were varied to evaluate its impact: its location with respect to the buffer, its distance from the AlGaN/GaN interface, its thickness and its boron incorporation.

Finally, Chapter 8 summarizes our conclusions and details future research directions.

CHAPTER II

NITRIDE MATERIALS AND HIGH ELECTRON MOBILITY TRANSISTORS

Silicon is a cheap, abundant and easy-to-process material that was critical for the semiconductor industry boom. It is still the best choice for nowadays information technologies or data storage. However, it is not suitable for high speed and high performance applications for instance in the microwave domain. It is in fact advanced materials, such as III-V compounds, that have allowed the defense and telecommunication industries to thrive thanks to the remarkable properties of these semiconductors. In fact, GaAs or InP, which are part of the medium direct bandgap semiconductors, provide larger (power)×(bandwidth) product values with good thermal conductivities, and have been crucial for the development of optoelectronics.

In the last two decades, on the other hand, nitride materials have played a disruptive role in the advent of solid-state lightning at new wavelengths [35] and electronic devices capable of handling high frequencies and high power levels even in extreme conditions (high temperature, high radiation, etc.) [36]. Moreover, size reduction, reliability, and efficiency are considerably enhanced, as observed with MMICs, where passive elements and interconnects are fabricated on the same semiconductor substrate as the active devices. Thus, MMICs, which use nitride HEMTs, are much less bulky. Yet, for certain microwave applications, they are still not competitive enough against conventional circuit assemblies such as vacuum tubes in terms of cost-efficiency and compactness[1] [37].

Gallium nitride (GaN), aluminium nitride (AlN), indium nitride (InN), and related

[1]We can mention the example of microwave ovens.

ternary alloys surpass other mainstream III-V materials because of several factors, including wider direct bandgaps, high peak and saturation velocities, large breakdown voltages, and better thermal conductivities. Moreover, nitride materials have unique piezoelectric properties that have motivated the scientific community to use them in HEMT structures [38].

2.1 Nitride materials

2.1.0.1 III-V and nitride materials

Table 1 gives an overview of the figures of merit of typical materials used in solid-state electronics. We first observe that GaAs or InP have the greatest mobility values. It explains why they have been so far the favorite materials for transistors working at very high frequencies. Metal-semiconductor field effect transistors (MESFETs) based on GaAs used to prevail until HEMT heterostructures surpassed them. Optimized GaAs MESFETs only showed a maximum operating frequency (f_{max}) of 160 GHz, whereas latest records reported were up to 1 THz for an InP HEMT and close to 500 GHz for the associated MMIC [39]. Yet, figures such as the thermal conductivity and the critical breakdown voltage show their limitation to sustain high energies. Alternately, nitrides grown in a wrtzite structure allow band engineering[2] between 0.7 and 6.2 eV (values associated with InN and AlN, respectively), which implies high bandgap to withstand high power levels and also explains their resilience towards very large breakdown voltages[3]. Their excellent electron-transport properties, i.e. very large peak saturation velocity and mobility, enable operation at high frequencies. Besides, a good thermal conductivity is a key factor for heat transfer engineering and for manufacturing size reduction of devices. Finally, even though SiC surpasses GaN

[2]Band engineering is the control and judicious combination of materials of different bandgap values to generate a wide range of physical phenomena or enhance certain electrical or optical properties.

[3]As a rule of thumb, the maximum power sustainable is approximately proportional to the fourth power of the band gap energy.

Table 1: Comparison of different semiconductor materials for high-power/-frequency applications.

	Si	GaAs (AlGaAs/InGaAs)	InP (InAlAs/InGaAs)	4H SiC	GaN (AlGaN/GaN)
Band gap (eV))	1.1	1.42	1.35	3.26	3.39
Electron Mobility ($cm^2\ V^{-1}\ s^{-1}$)	1500	8500	10000	700	1500
2DEG sheet electron density (cm^{-2})	NA	$< 4{\times}10^{12}$	$< 4{\times}10^{12}$	NA	$> 1{\times}10^{13}$
Saturated peak electron velocity ($\times 10^7$ cm/s)	1	2.1	2.3	2	3
Critical breakdown field (MV/cm)	0.3	0.4	0.5	2	3.3
Thermal conductivity ($W.cm^{-1}\ K^{-1}$)	1.5	0.5	0.7	4.5	< 1.7
Relative dielectric constant (ε_r)	11.8	12.8	12.5	10	9.0

for thermal management, it cannot be directly employed for a HEMT structure as no suitable heterostructure material has been found (it is used though as a substrate, see Section 2.1.3). Until now, the performance of SiC has only been exploited in MESFET structures [40]. One solution could be to use SiAlC or SiInC as illustrated in a patent filled by Northrop Grumman [41]. Note that SiC remains the best substrate for GaN HEMTs when heat transfer is the most critical design constraint.

2.1.1 Crystal structure

As far as the crystal structure is concerned, nitrides are grown in their thermodynamically stable *wrtzite* phase, which is part of the hexagonal crystal system. As seen in Fig. 5, there are two separate sublattices of hexagonal close-pack types (HCP), one made with an element from the group $IIIA$ (3^{th} column of the periodic table, i.e. Ga, Al, In, or B), and the other made with nitrogen (i.e. N, group VA, 5^{th} column of the periodic table). They are shifted from each other by 5/8 of the lattice parameter of

the unit cell along the $< c >$ axis[4], and both intricated in such a way that each atom is tetrahedrally coordinated with four atoms of the other sublattice. It is interesting to note that the c-axis ([0001], vertical direction in Fig. 5) lacks an inversion plan. Nitride materials are therefore non-centrosymmetric crystals.

Gallium nitride's atomic bond is also polarized as a result of the strong difference in electronegativity between its two constituting elements[5]. This property, together with the low symmetry of the wrtzite crystal structure, leads to the presence of a *spontaneous* polarization along the $< c >$ axis [42].

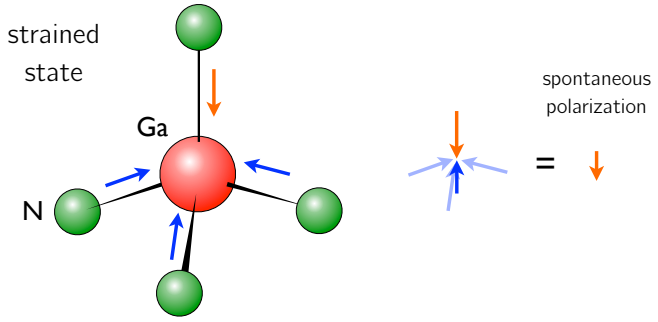

Figure 3: Contribution of the different dipole moment in the generation of a spontaneous polarization in GaN materials when the structure is strained.

2.1.1.1 Polarization in nitrides

Additionally, when the structure is under either a tensile or compressive strain, the dipolar momentum of the Ga-N bond is altered. This dipolar momentum decreases when the bond becomes smaller, i.e. when the crystal is under compressive stress along the $< c >$ axis. However, this decrease of each dipolar momentum in the 4 bonds of the tetraedral structure is overcompensated by the angular bending of the 3 bends, which are not parallel to the $< c >$ axis. Therefore, the global effect of compressive strain along $< 0001 >$ leads to an increase of the dipolar momentum

[4]It is the vertical axis (or [0001]), which also happens to be the growth direction.
[5]It remains also true for any other nitride binary compound.

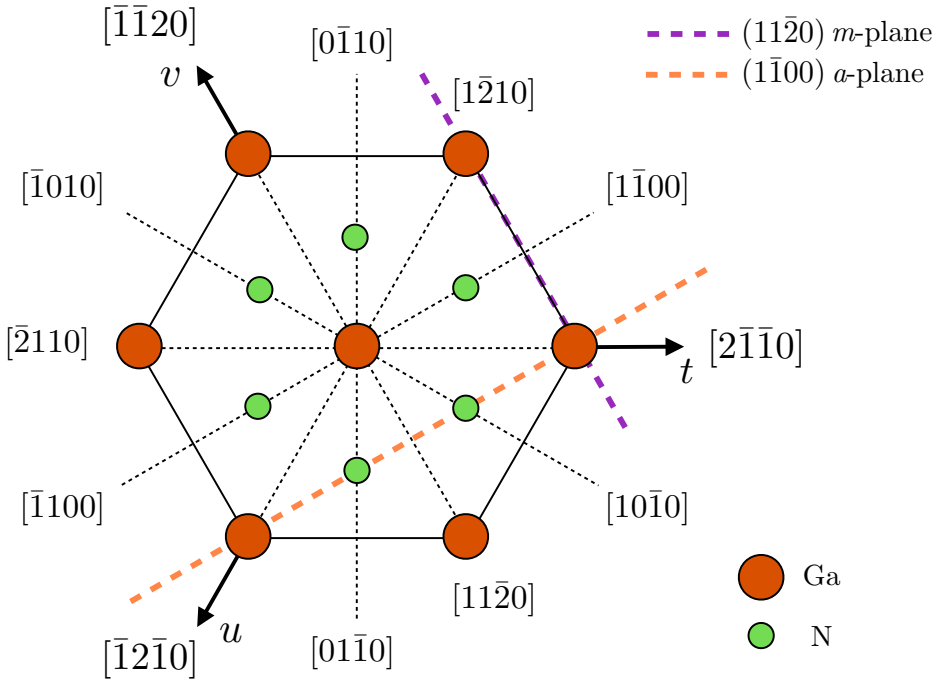

Figure 4: Orientations in nitrides with a- and m-planes projected on the (0001) basal plane (inspired from [3])

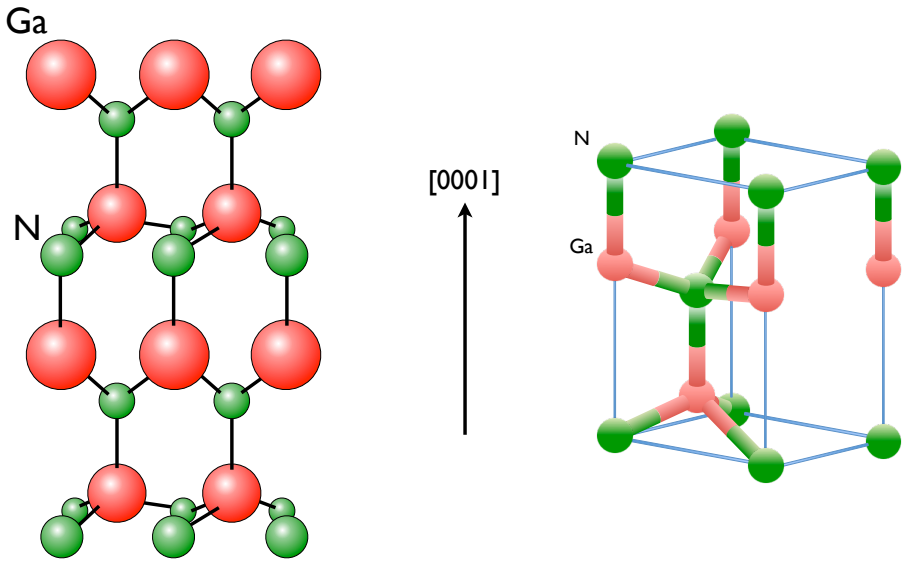

Figure 5: The wrtzite structure of nitride compounds, example of GaN - schematic drawing of the wrtzite crystal structure with *Ga-face* on top (left) and the wrtzite unit cell associated (right).

directed towards $< 0001 >$ III direction. Hence, an extra *piezoelectric* polarization (see Fig. 6) appears in addition to the already existing *spontaneous* polarization. As we will see later, this very peculiar property is of particular interest for electronics, and nitrides are unique in that their polarization is five times higher than other III-V compounds.

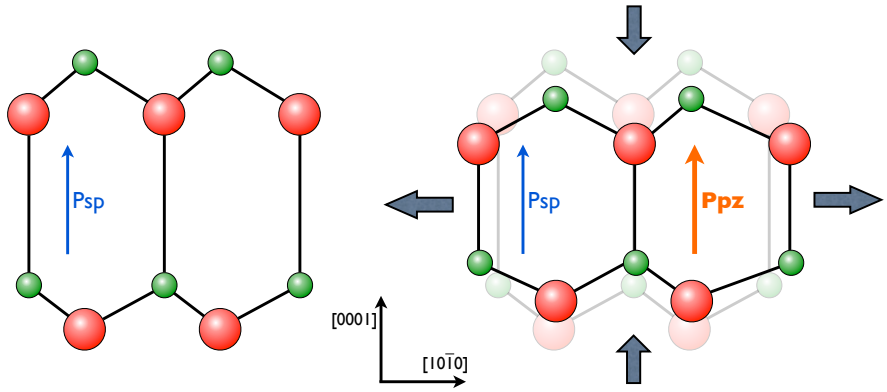

Figure 6: The polarization in nitride compounds - spontaneous polarization (left) and the addition of the piezoelectric polarization (right).

To calculate the piezoelectric field in nitrides, either the piezoelectric tensor **e** or the piezoelectric modulus **d** must be known. The relationship between these two is through the elastic tensor **C** as follows:

$$\mathbf{e} = \mathbf{dC} \tag{1}$$

The polarization vector can be derived by two equations:

$$\vec{P}^{\,pz} = \mathbf{e}\,\varepsilon \quad \text{or} \quad \vec{P}^{\,pz} = \mathbf{d}\,\sigma \tag{2}$$

with ε the strain tensor and σ the stress tensor.

Notations can be simplified employing Voigt's abbreviated notations as follows:

$$xx = 1 \quad yy = 2 \quad zz = 3 \quad yz = 4 \quad xz = 5 \quad xy = 6$$

where x, y, and z denotes respectively orthogonal $[2\bar{1}\bar{1}0]$,$[01\bar{1}0]$, and [0001] directions.

$$\begin{bmatrix} \sigma_{xx} \\ \sigma_{yy} \\ \sigma_{zz} \\ \sigma_{yz} \\ \sigma_{xz} \\ \sigma_{xy} \end{bmatrix} = \begin{bmatrix} \sigma_1 \\ \sigma_2 \\ \sigma_3 \\ \sigma_4 \\ \sigma_5 \\ \sigma_6 \end{bmatrix} \quad \text{and} \quad \begin{bmatrix} \varepsilon_{xx} \\ \varepsilon_{yy} \\ \varepsilon_{zz} \\ 2\varepsilon_{yz} \\ 2\varepsilon_{xz} \\ 2\varepsilon_{xy} \end{bmatrix} = \begin{bmatrix} \varepsilon_1 \\ \varepsilon_2 \\ \varepsilon_3 \\ \varepsilon_4 \\ \varepsilon_5 \\ \varepsilon_6 \end{bmatrix}$$

The relationship between stress and strain is given through Hooke's law as follows using Voigt's notations:

$$\sigma_i = \sum_j C_{ij}\varepsilon_j \tag{3}$$

In a wrtzite structure, due to its symmetry, the fourth ranked elastic tensor can be reduced to:

$$\begin{bmatrix} \sigma_1 \\ \sigma_2 \\ \sigma_3 \\ \sigma_4 \\ \sigma_5 \\ \sigma_6 \end{bmatrix} = \begin{bmatrix} C_{11} & C_{12} & C_{13} & 0 & 0 & 0 \\ C_{12} & C_{22} & C_{13} & 0 & 0 & 0 \\ C_{13} & C_{13} & C_{33} & 0 & 0 & 0 \\ 0 & 0 & 0 & C_{44} & 0 & 0 \\ 0 & 0 & 0 & 0 & C_{44} & 0 \\ 0 & 0 & 0 & 0 & 0 & \frac{1}{2}(C_{11} - C_{12}) \end{bmatrix} \begin{bmatrix} \varepsilon_1 \\ \varepsilon_2 \\ \varepsilon_3 \\ \varepsilon_4 \\ \varepsilon_5 \\ \varepsilon_6 \end{bmatrix} \tag{4}$$

As illustrated in Fig. 7, a top nitride layer for HEMT structure is generally strained on a GaN substrate due to lattice or thermal expansion mismatch. For growth along the c-axis, the stress, induced in epitaxial heterostructures by lattice mismatch and thermal mismatch, is along the basal plane. Lack of any force in the growth direction, and the fact that the crystal can relax freely in this direction, lead to a biaxial stress and also induces strain along the c-axis. As a consequence, we can derive:

$$\sigma_{zz} = \sigma_{yz} = \sigma_{xz} = \sigma_{xy} = 0 \quad \text{and} \quad \sigma_{xx} = \sigma_{yy} \neq 0, \tag{5}$$

$$\Longleftrightarrow \sigma_3 = \sigma_4 = \sigma_5 = \sigma_6 = 0 \quad \text{and} \quad \sigma_1 = \sigma_2 \neq 0. \tag{6}$$

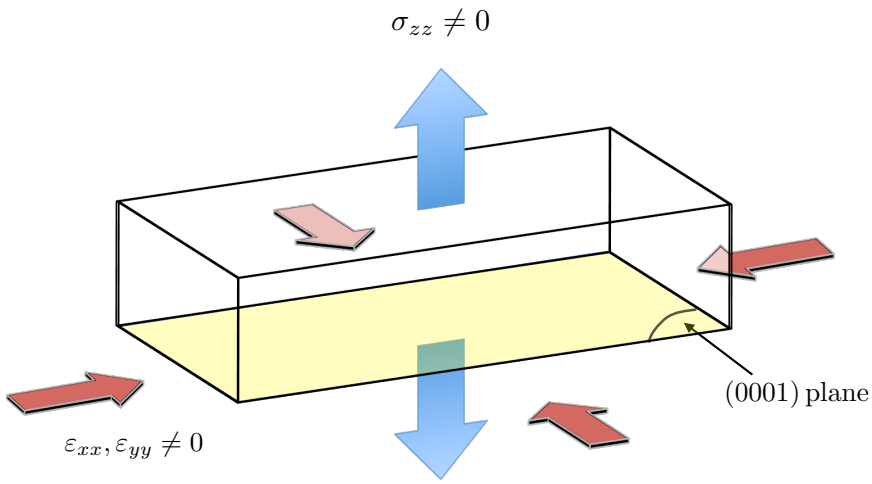

Figure 7: Strain and stress components for a typical configuration of the top layer of a HEMT structure in a wrtzite crystal.

Moreover, Eq. 4 leads to:

$$\begin{cases} \sigma_{xx} &= C_{11}\varepsilon_{xx} + C_{12}\varepsilon_{yy} + C_{13}\varepsilon_{zz}\,, \\ \sigma_{yy} &= C_{12}\varepsilon_{xx} + C_{22}\varepsilon_{yy} + C_{13}\varepsilon_{zz}\,, \\ \sigma_{zz} &= C_{13}\varepsilon_{xx} + C_{13}\varepsilon_{yy} + C_{33}\varepsilon_{zz}\,, \end{cases} \tag{7}$$

Therefore, we can derive using Eq. 4 and Eq. 6:

$$\begin{cases} \sigma_1 &= (C_{11} + C_{12} - \frac{C_{13}^2}{C_{33}})\,\varepsilon_1, \\ \varepsilon_3 &= -2\frac{C_{13}}{C_{33}}\varepsilon_1\,. \end{cases} \tag{8}$$

It should be noted that the term $2\,C_{13}/C_{33}$ corresponds to Poisson's ratio, which is the ratio between the relative variation of the transversal dimension and the relative variation of the length along the direction of the force. Moreover, the relative change of the lattice constant a with respect to the constant of the relaxed crystal a_0 is expressed as follows:

$$\varepsilon_1 = \frac{a - a_0}{a_0}. \tag{9}$$

Finally, according to Eq. 2, and considering only non-vanishing components, the polarization caused by the biaxial strain can be calculated through:

$$P_3^{pz} = \varepsilon_1 e_{31} + \varepsilon_2 e_{32} + \varepsilon_3 e_{33} = 2\,\varepsilon_1 e_{31} + \varepsilon_3 e_{33}, \tag{10}$$

$$\Longrightarrow \quad P_3^{pz} = \frac{a - a_0}{a_0}\left[e_{31} - e_{33}\frac{C_{13}}{C_{33}}\right] \quad \mathrm{cm}^{-2}. \tag{11}$$

2.1.1.2 Optical properties

Nitride materials, with their direct bandgaps, are excellent candidates for optical applications. They cover a large range of bandgaps from 0.7 to 6.2 eV (see Fig. 31 in Section 4.1 for the band diagram) and can therefore emit light in the entire visible spectrum. Bandgaps of GaN, AlN and InN are respectively 3.4 eV [43], 6.2 eV [44] and 0.7 eV [45]. The calculated band structure of GaN is shown in Fig. 8. The maximum of the uppermost valence band is at the center of the Brillouin zone (Γ), aligned with the minimum of the conduction band, hence leading to a direct bandgap. In addition, because of the spin-orbit interaction and the symmetry of the hexagonal structure, the valence band has three bands, i.e. three possible excitons observable according to the strain (bands A, B and C in Fig. 9). Consequently, 3 type of excitons exist in wrtzite GaN, corresponding to 3 hole-electron possible pairs from the valence and conduction bands, respectively.

2.1.2 Growths and Substrates

The growth of nitride semiconductor materials is usually done by molecular beam epitaxy (MBE) or metalorganic chemical vapor deposition (MOCVD). One of the main challenge of the production of nitride-based devices is the lack of suitable substrates for their epitaxial growth. We are limited to commercially available high-quality bulk single crystal substrates. Figure 10 shows a table of lattice parameters and thermal characteristics of a number of the possible substrate materials for nitride growth and their lattice mismatch with GaN from [3]. Today, sapphire (Al_2O_3), silicon carbide

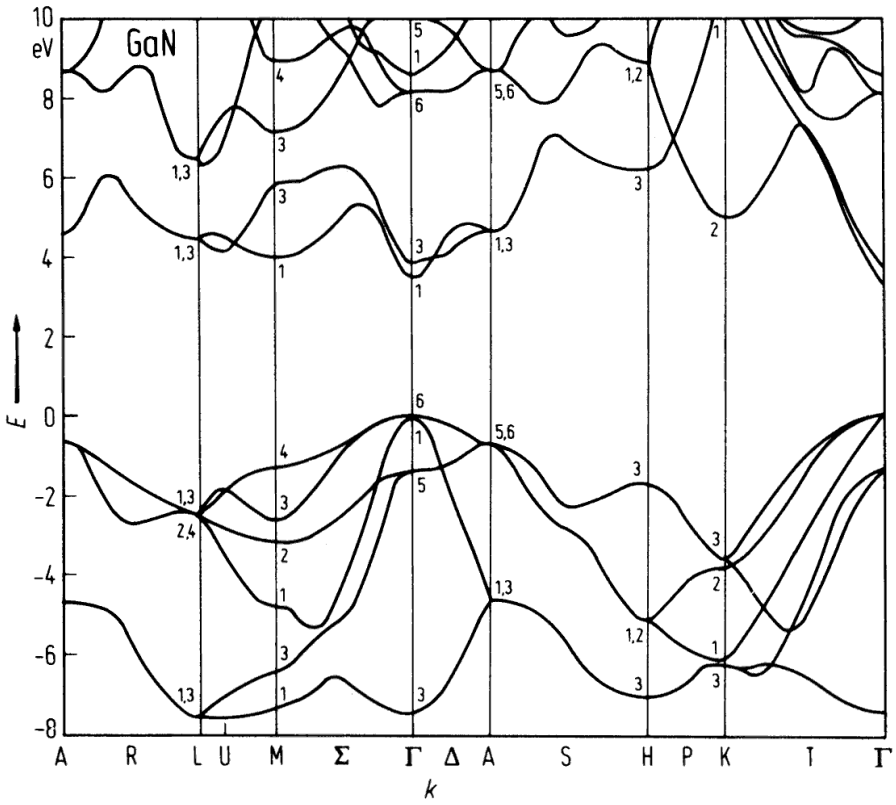

Figure 8: The band diagram of GaN (extracted from [4]).

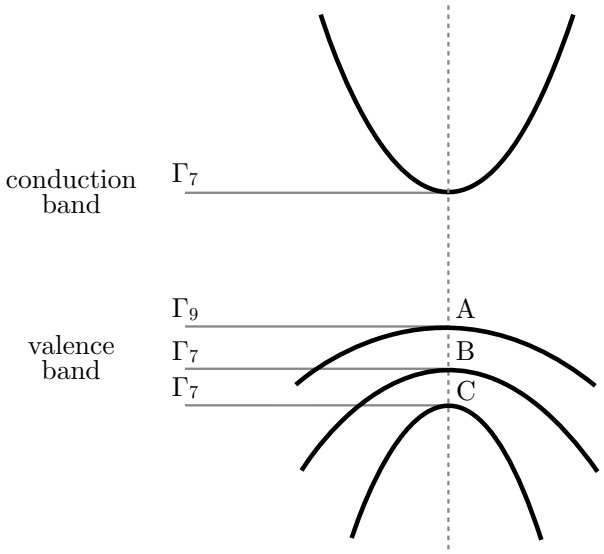

Figure 9: Band-edge structure near k=0 for GaN.

(SiC), and silicon (Si) are commonly adopted to grow single crystal wrtzite GaN. However, free-standing GaN substrates are usually put aside because of their small size and prohibitive cost. Moreover, thermal management is crucial and greatly depends on the substrate used. For that reason, SiC is the most commonly used substrate to reach higher performance despite its higher cost since HEMTs are aimed at working at high energies. Diamond, although expensive, now attracts more attention because of its very high thermal conductivity [46]. Besides, growth of GaN on silicon is becoming standard despite the mismatch; much effort is devoted to improving the structural quality since the potential cost cut is huge and cheap very large silicon wafers are available today.

As GaN does not have perfectly lattice-matched substrates, the hetero-epitaxial layers are subject to stress and strains. When grown on sapphire, the lattice mismatch is $\Delta a/a \sim 16\%$. After a critical thickness of a few nanometers, the elastic energy that has been accumulated will be relaxed through defects such as dislocations in the crystal. Growth of GaN will originate in nano-columns. These micropillars are all independently tilted and twisted (see Fig. 12) relative to the c-axis. Their specific length along the c-axis is large compared to the one in the plane (i.e. their width). During growth, these structures coalesce quickly and inter-grain dislocations are created. Typically, the density of dislocations in GaN is usually of the order of $10^{7-9}\mathrm{cm}^{-2}$. Consequently, GaN comprises many structural and point defects originating to a large extent from lattice and stacking mismatch with substrates. Nevertheless, GaN contradicts the former belief that a high density of dislocations does not allow satisfying device performance.

Crystal	Conventional			Matched a (Å)	Thermal conductivity, κ ($W\,cm^{-1}\,K^{-1}$)	$\Delta a/a$, $\Delta c/c$ ($\times 10^{-6}\,K^{-1}$)	Space group	Mismatch
	a (Å)	b (Å)	c (Å)					
AlN (hexagonal)	3.104	—	4.966	3.104	3.2	4.2, 5.3	$P6_3mc$	−2.7%
GaN (hexagonal)	3.189		5.175	3.19	2.3	5.59, 3.17	$P6_3mc$	0%
Al_2O_3 (sapphire) (rhombohedral)	4.758		12.991	2.747	0.3–0.5	7.5, 8.5	$R\bar{3}c$	49% (∼13%)
4H-SiC (hexagonal)	3.073		10.053					−3.63%
6H SiC (hexagonal)	3.0817		15.1123	3.0817	4.9	4.2, 4.68	$P6_3mc$	−3.36%
ZnO (hexagonal)	3.2496		5.2065	3.2496	0.3–0.4	4.75, 2.9	$P6_3mc$	+1.9%
$ScAlMgO_4$ (hexagonal)	3.246		25.195			6.2, 12.2	$R\bar{3}m$	+1.8%
γ-$LiAlO_2$ (tetragonal)	5.1687		6.2679	3.1340		7.1, 15	$P4_12_12$	−1.7%
$LiGaO_2$ (orthorhombic)	5.402	6.372	5.407	6.372		$a=6$, $b=9$, 7	$Pna2_1$	0.18%
$MgAl_2O_4$ (cubic/spinel)	8.083					7.45	$Fd\bar{3}m$	
Si (cubic)	5.4301				1.5	3.59	$Fd\bar{3}m$	
GaAs (cubic)	5.6533				0.5	6	$F\bar{4}3m$	
β-SiC (cubic)	4.36				4.9		$F\bar{4}3m$	
MgO (cubic/rock salt)	4.216					10.5	$Fm\bar{3}m$	

Figure 10: Lattice parameters and thermal characteristics of a number of the prospective substrate materials for nitride growth and their lattice mismatch with GaN (extracted from [3]).

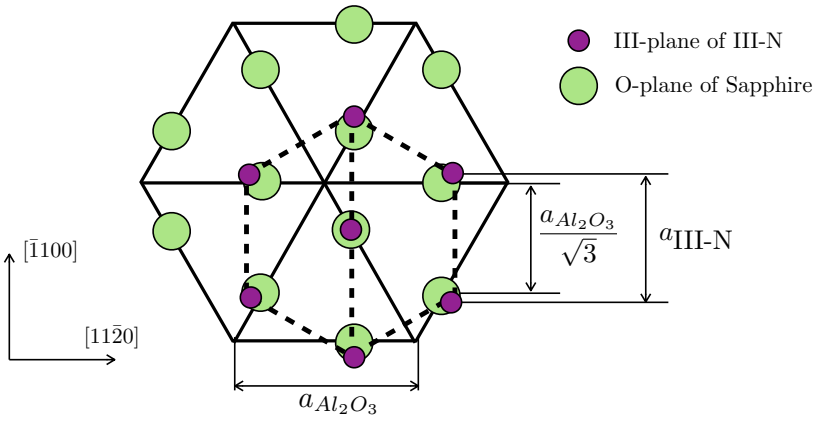

Figure 11: Growth of III-N material on a sapphire substrate (inspired from [5])

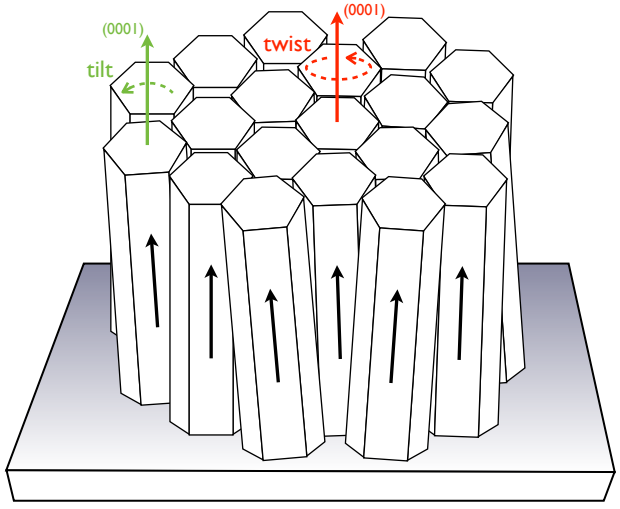

Figure 12: Tilt and twist of grains when grown on lattice mismatched substrate (inspired from [6])

2.1.3 Pseudomorphic growth of nitride compounds

As seen in Section 2.2.1, III-V based devices exhibit interesting properties when employing heteroepitaxy, which is the deposition by epitaxy of crystalline films of different materials. Nevertheless, lattice mismatch can occur, and, if that latter is too large, cracks and defects appear, and drastically impede the device performance. To minimize this effect, we design structures with a particular attention given to the mismatch. In a hetero-junction for HEMT, the *bulk* layer (a few μm) imposes its lattice parameter, and hence, stresses the crystalline structure of the thin layer grown on top for it. Hence, when grown pseudomorphically (i.e. with a mismatch low enough to avoid defects), the lattice is either in a tensile or compressive strain, as illustrated in Fig. 13. For illustration, in the case of an AlGaN/GaN HEMT, an AlGaN layer is pseudomorphically grown on GaN with a percentage of aluminium around 30%. It experiences a tensile strain (i.e. it gets expanded along the growth plane and stretched along the $< c >$ axis) that induces a piezoelectric field as seen in Section 2.1.1.1. This polarization effect is critical for nitride HEMTs as explained in the next Section.

2.2 High electron mobility transistors with III-N alloys

2.2.1 The HEMT and III-V materials

The idea of a *high electron mobility transistor* appeared in 1979[6]. Their development came along with the advent of III-V compounds as it is based on a heterojunction (which did not exist with Si-based structures at that time, SiGe(C) structures appeared later). In regular HEMT structures based on InP or GaAs (for heterojunctions that are InAlAs/InGaAs and AlGaAs/GaAs, respectively), discontinuities in the conduction and valence bands are encountered at the interface because of the difference

[6]The paternity of the idea can be attributed to several groups. It is unclear whether it was first Mimura at Fujitsu Labs, Delagebeaudeuf and Linh in France or even Dingle *et al.* at Bell Labs for the first demonstration.

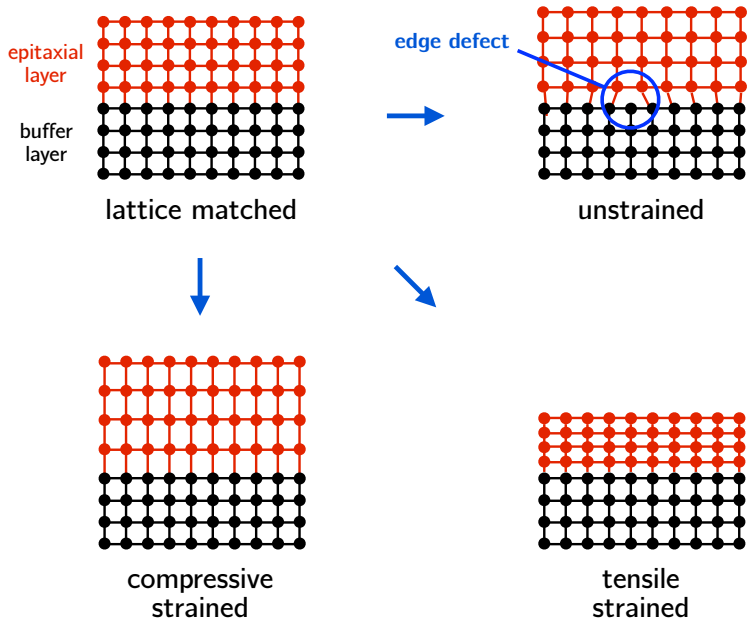

Figure 13: Epitaxial growth of a tensile/compressive strained or unstrained layer.

of bandgap energies between the two parts of the heterostructure. We focus our attention on *type I* heterostructures, i.e. with a straddled alignment, in which discontinuities of the conduction and valence bands lead to confinement of both electrons and holes within the lower bandgap semiconductor material [47]. The discontinuity of the conduction band can lead to charge transfer towards the lower bandgap semiconductor below the Fermi level and, therefore, lead to trapping of the electrons in a quantum well located close to the hetero-interface. Hence, at equilibrium, a fixed 2DEG with a very high density (at least 10^{12-13} carriers per square-centimeters) is naturally enclosed within the structure and confined within a few nanometers. Carriers in the 2DEG can also reach a very high mobilities (up to $10\,000\,\mathrm{cm^2\,V^{-1}s^{-1}}$ at 300K in some InAlAs/GaInAs HEMT structures, $1\,000\,000\,\mathrm{cm^2\,V^{-1}s^{-1}}$ at 2K for some AlGaAs/GaAs HEMT structures and $2000\,\mathrm{cm^2\,V^{-1}s^{-1}}$ at 300K in AlGaN/AlN/GaN HEMT structures) together with high saturation peak velocities (close to 3×10^7cm/s in AlGaN/AlN/GaN HEMT structures), as already seen in Table 1.

Moreover, in conventional HEMT structures, the barrier layer, i.e. the upper layer

of higher bandgap, needs to be n-doped to become the *donor* layer that is supposed to fill the 2DEG with carriers. The delivered electrons are therefore spatially separated from the dopants they originate from, the first ones being trapped in the 2DEG, the others being fixed charges in the *donor* layer (see Fig. 14 where a spacer layer separates the 2DEG from the Si-doping layer). Hence, this added distance helps screen the Coulomb forces of attraction exerted by the ionized positive donors, which inherently slow electrons down [48, 49]. Therefore, the effect of the ionized impurity scattering is reduced, and high mobility and saturation peak velocity can be achieved.

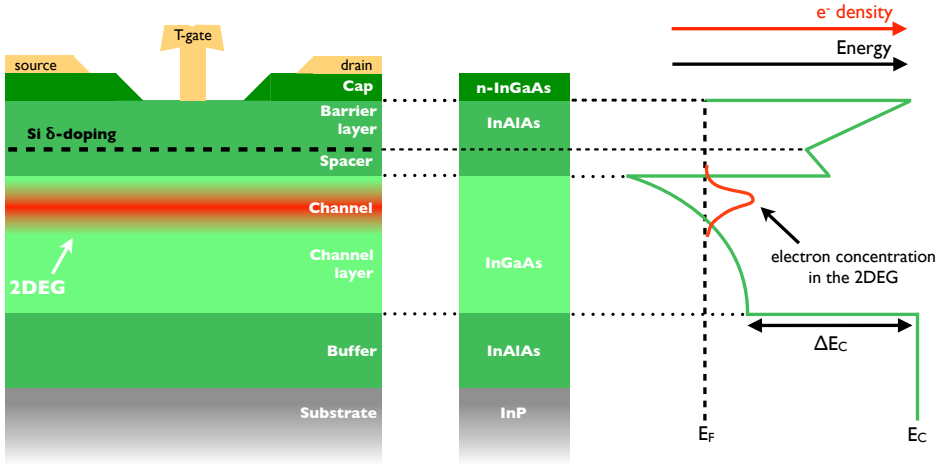

Figure 14: An example of related art technology - InP-based III-V HEMT with the associated conduction band profile (inspired from [7]).

2.2.2 The AlGaN/GaN HEMT

Two decades ago, Khan *et al.* demonstrated the first nitride HEMT based on an AlGaN/GaN heterostructure [50]. As illustrated in Fig. 15, we can see in a typical AlGaN layer grown on top of GaN with the existence of an additional piezoelectric field induced by a lattice mismatch between the two constituents.

The GaN layer is usually very thick, on the order of a few μm, and is therefore called the buffer as it is fully relaxed. The AlGaN layer, which is much thinner than

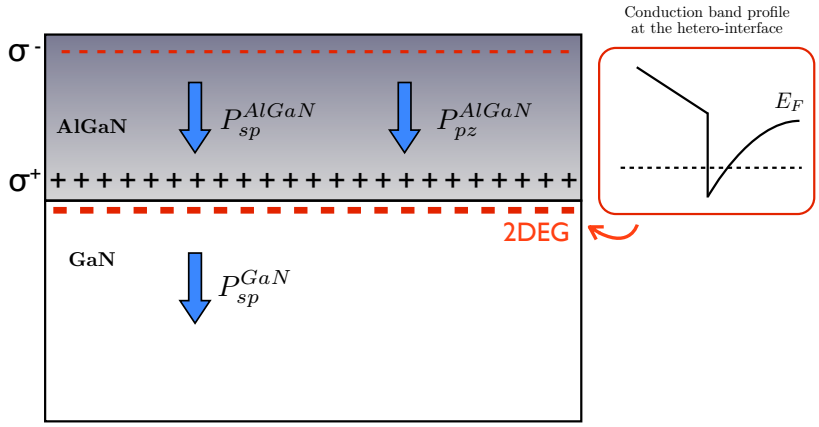

Figure 15: Nitride HEMT - Polarization and the 2DEG.

the bulk GaN on which it is epitaxially grown (typically 20-30 nm on top of a bulk of at least 3.5 μm), will be strained (in the ideal case, there is no relaxation). Thus, its crystalline structure is in tension since the relaxed lattice parameter of the AlGaN, being smaller than that of GaN, is stretched along the a-plane (perpendicular to the growth direction). This induces a piezoelectric polarization field (P_{pz}^{AlGaN}) that is added to the already-existing spontaneous polarization (P_{sp}^{AlGaN}). Therefore, the total polarization in the strained AlGaN layer is much larger than that of the relaxed GaN layer (P_{sp}^{GaN}), and the substraction of these two represents the electric *excitation* field D created at the interface (see Fig. 15). Hence, electrons concentrate at the interface to compensate this discontinuity, and lead to an electronic surface charge density at the interface as follows:

$$\sigma_{AlGaN/GaN} = P_{sp}^{GaN} - (P_{sp}^{AlGaN} + P_{pz}^{AlGaN}) \quad \text{cm}^{-2}. \tag{12}$$

The polarization due to the axial strain, as per Eq. 11, is

$$P_{pz}^{AlGaN} = \frac{a - a_0}{a_0}\left[e_{31} - e_{33}\frac{C_{13}}{C_{33}}\right] \quad \text{cm}^{-2}, \tag{13}$$

where, a and a_0 are the lattice parameters along the a-axis in the AlGaN and GaN layers, respectively; the constants e_{xy} and c_{ij} are the piezoelectric and elastic constants, respectively, of the AlGaN layer. All parameters of the ternary AlGaN are

linearly interpolated between those of the two binaries GaN and AlN. Thus, a 2DEG is formed at the heterointerface where electrons are trapped within a quasi-triangular potential well [51] with densities of carriers around $10^{13}\,\mathrm{cm}^{-2}$, i.e. ten times higher than in GaAs or InP HEMTs.

Additionally, nitrides have very high unintentional background doping (n-type), which was usually between 10^{17} and 10^{18} electrons per cm^3 at room temperature until 2000 [52], and whose origin is still debated among the research community. This doping was thought to be due to nitrogen vacancies, but it is most probably because of impurities such as silicon and oxygen, which inhere in the pollution specific to the growth process [53].

However, since the GaN layers in the actual HEMT structures are semi-insulating, the shallow donors in the GaN are overcompensated by deep-acceptors, either purposely introduced (intentional carbon or iron doping) or resulting from the crystal defects. On the other hand, the negative virtual charges related to the polarization effects and located on top of the AlGaN layer are also compensated, at equilibrium, by positive charges. Several studies provide evidence that surface traps, on top of the barrier layer, are the major contributors [54, 55, 56]. The most efficient way to ensure control and reproducibility of those positive charges whose density can influence the electron density within the channel 2DEG, is to implement surface passivation by adequate insulating material such as Si_3N_4 and the related insulator/AlGaN interface engineering. In optimized structures, lag effects on the density of carriers in the 2DEG can be strongly reduced, while the breakdown voltage in enhanced [57].

2.2.3 Growth direction and Polarity

Most GaN-based HEMT structures reported in the literature are grown along the *c*-direction. As a matter of fact, nitrides' atomic stacking usually differ from those

of substrates on which they are grown. Moreover, as seen previously, GaN is non-centrosymmetric, notably in the [0001] direction, i.e. two different sequences of atomic layering is possible, both inverse from each other, as illustrated in Fig. 16. Subsequently, depending on growth conditions, either Ga-face or N-face layers can be obtained [3]. In fact, their respective properties are allegedly not alike, and, according to our analysis in 2.1.1.1, the polarization is logically upside down in N-face layers [58]. Hence, the polarity of the material depends on the growth direction chosen.

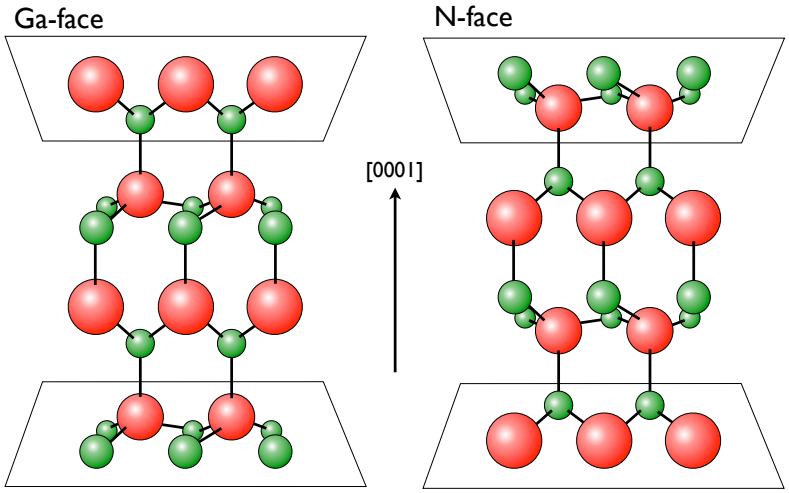

Figure 16: Ga-face and N-face growth of GaN

In this study, all structures, grown by MOVPE, possess a Ga-polarity. However, several studies reports GaN-based HEMT structures using N-face growth (usually employing MBE growth [59]). Spontaneous and piezoelectric polarizations are then switched in the opposite direction of conventional HEMT structures. Subsequently, the growth surface polarity also affects the formation of the 2DEG. In the case of HEMT structures grown on N-face, 2D hole gas could be expected to form spontaneously. Due to the extremely low mobility of holes in GaN (typically $< 10\,\mathrm{cm^2\,V^{-1}s^{-1}}$), the perspective to get p-channel III-N HEMTs has not been considered as very promising so far.

CHAPTER III

GROWTH AND CHARACTERIZATION OF HEMT STRUCTURES

3.1 Growth of semiconductor devices

3.1.1 The MOVPE principle

Growths of III-V compounds has become widespread with GaAs and InP semiconductors. It is the same reactors that were adapted to grow nitrides. The epitaxy through chemical vapor deposition is generally known under the term of metal-organic vapor phase epitaxy (or MOVPE, as MOCVD concerns any crystalline quality). This technique was first presented by Manasevit *et al.* (despite predating patents describing similar process [60]). MOVPE quickly became the leading technique for large-scale manufacturing with the highest purity.

A schematic illustration of the general principle of MOVPE growth is shown in Fig. 17. The process of growth is more complex than for MBE as several chemical reactions occur, and are to be controlled, for the production of basic compounds in the reactor and for epitaxy to happen. The sequence of growth can be broken down into 4 main phases: input of gaseous precursors in the reactor chamber; pyrolysis of the molecules to obtain single atoms or smaller molecules; diffusion/adsorption on the surface of the substrate; surface reaction and epitaxy of atomic layers on the substrate and formation of by-products that are pumped away.

3.1.2 The MOVPE machine

Our growths were performed in the MOVPE reactor which was originally used for InP. Our machine is composed of 3 main parts: the growth chamber, the gas panel

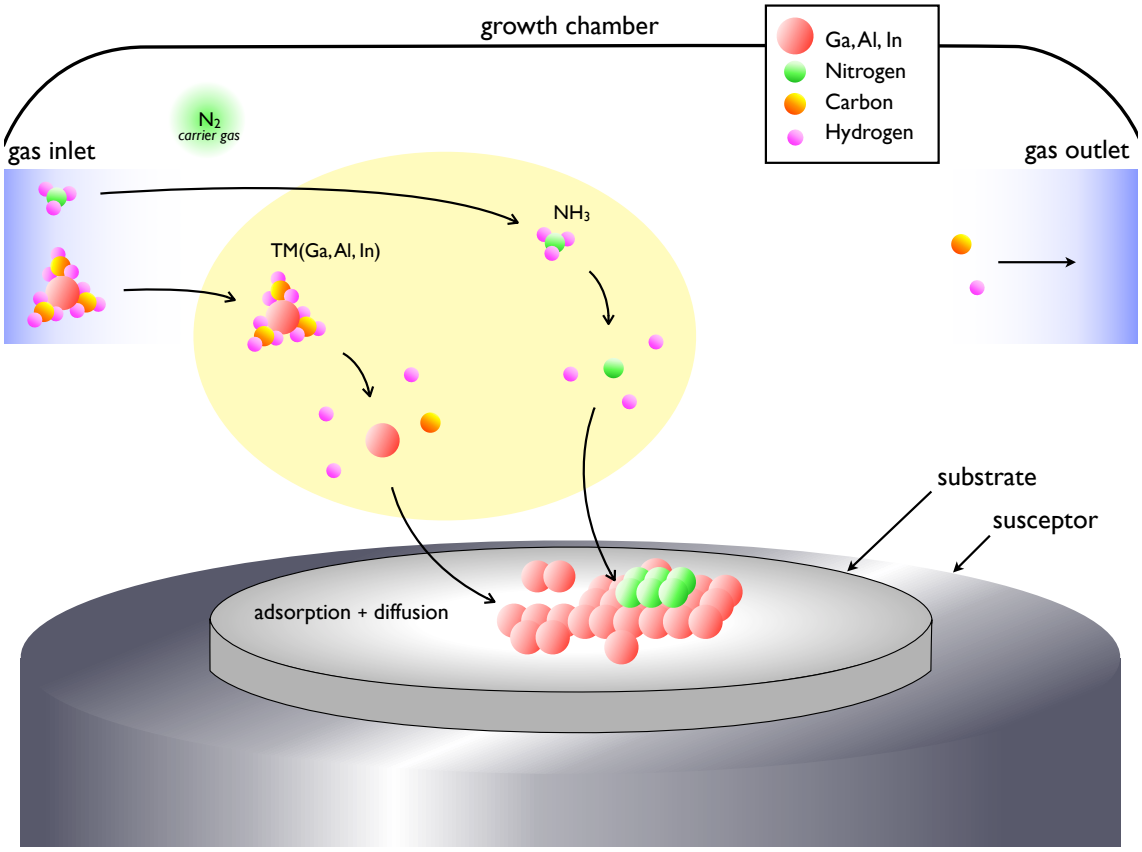

Figure 17: The principle of MOVPE - here illustrated for the epitaxy of GaN layers with N_2 as the carrier gas.

and sources for precursors. A pump is placed at the exit of the growth chamber to allow pressures from atmospheric down to 50 Torr. Nitrogen is employed as a carrier gas. Sources for III-group precursors were trimethylgallium (TMGa), trimethylaluminium (TMAl), triethylboron (TEB), and ammonia for gallium, aluminium, boron, and nitrogen, respectively. The reactor has a T-shaped chamber, with a horizontal rectangular silica tube tapered on both sides in which gas flows, welded to a vertical silica tube where the graphite susceptor is supported by a rotating axis [61]. In the axis of the vertical tube, a *in-situ* reflectometer is installed to perform measurements during growth. Data can be used later to analyze growth rate, thickness, surface roughness, and the right layer sequence.

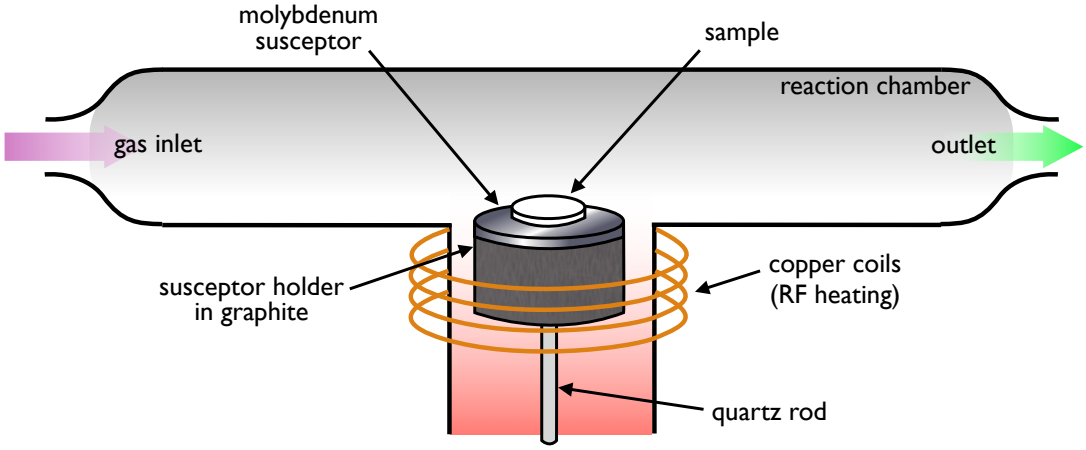

Figure 18: Schematic of the T-shape reactor used in our lab for the growth of nitrides.

3.2 Characterization of semiconductor structures

3.2.1 The AFM

3.2.1.1 Principle

Atomic force microscopy (or AFM) is the primary tool to measure surface roughness and surface defects on our grown structures. A schematic illustration is shown on Fig. 19. It is a non-destructive method consisting of a cantilever (acting as a spring)

comprising a nanometer-scale tip scanning the surface of the sample. Forces between the sample and the tip make that latter move and its deflection is detected by a laser. The force between the sample's surface and the probe can be derived from Hooke's law and its value gives the distance (dominant interactions being Van der Waals interactions).

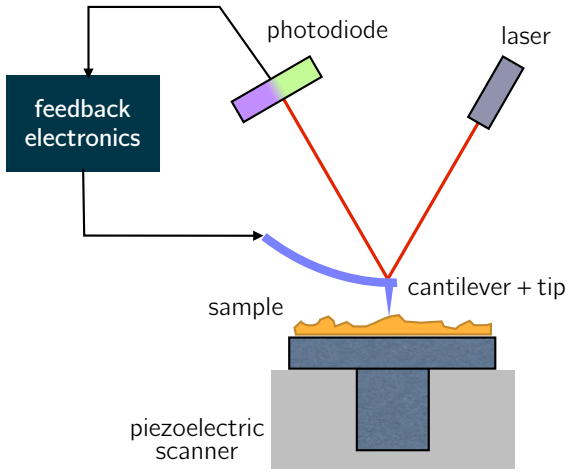

Figure 19: Principle of AFM (inspired from [8])

3.2.1.2 Measurements performed for HEMT samples

Regarding HEMT structure growths presented later, template substrates employed were diced into smaller samples for cost considerations. For all samples, 5μm $\times$ 5μm images were taken. As depicted in Fig. 20, 3 of them are located on edges and one is situated at the center.

Nevertheless, considering structures to be processed for advanced characterization, the structural quality of the surface must be observed on a larger area. As our AFM tool was limited to 512 points per line, we moved to a 20μm $\times$ 20μm image taken at the center. This has been put in place for Series 5 and following ones (see Appendix A).

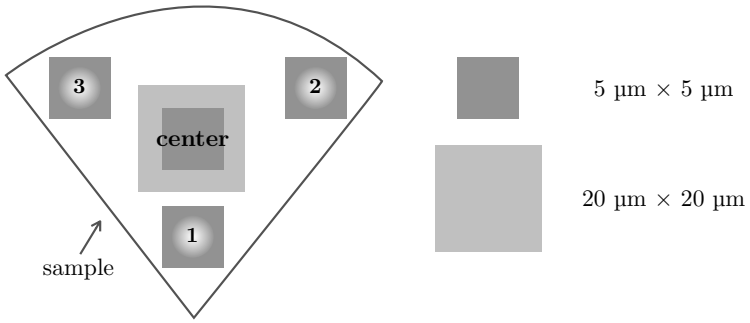

Figure 20: Description of the localization of AFM image measurements on a typical quarter of a disk sample made out from a diced substrate.

As far as the surface roughness value is concerned, we evaluated in practice the root mean square roughness (R_q) from the depth profile using typically a 0.5μm $\times$ 0.5μm box. As several images were taken over the sample, we only extracted the worst value. Even though our AFM images are much larger, we could not perform a calculation over the entire area as the presence of V-defects was detrimental to the value obtained which would not genuinely reflect the structural quality of the growth. V-defects were studied separately and their density, over a 5μm $\times$ 5μm AFM image, was systematically estimated.

3.2.2 The XRD

X-ray diffraction (XRD, also known as X-ray crystallography) measurements exploit interactions between solids and X-rays. It is a non-destructive technique that enables researchers to determine crystal structures and defects. As illustrated in Fig. 21, an impinging monochromatic X-ray beam at wavelength θ with an angle ω scattered by a perfect crystal made of lattice planes spaced by a distance d[1] can lead to a constructive reflection under Bragg's conditions:

$$\lambda = 2d \sin\theta$$

[1] d must be in the same order of magnitude than the wavelength employed.

where θ is Bragg's angle (i.e. angle between the input and output beams wave vector and the reflecting crystal planes).

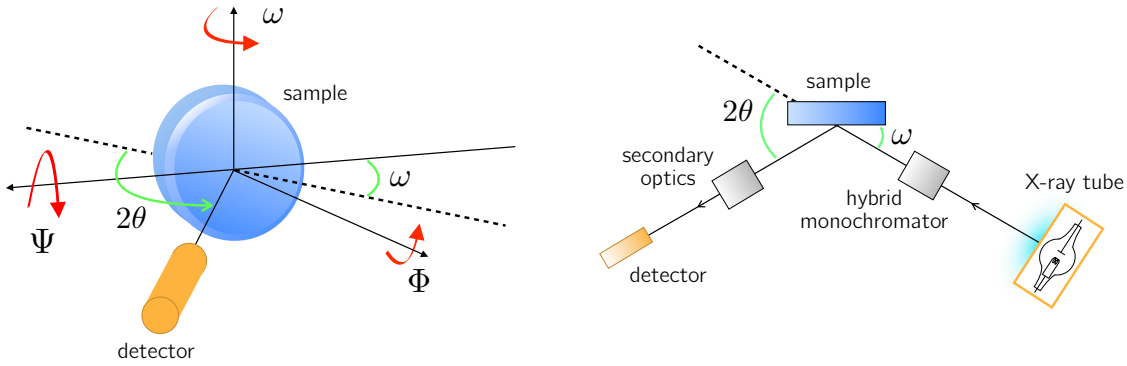

Figure 21: X-ray diffraction measurements principle (inspired from [8])

Our instrument was a PANalytical X'Pert diffractometer for which we use the X'Pert Epitaxy software to simulate structure and compare to experimental data. We usually measure rocking curves: the angle 2θ remains constant while we scan the angle ω through Bragg condition. For non-ideal crystals, the observed broadening in the curves (more specifically the FWHM or Full Width at Half Maximum) is due to the mosaicity (i.e. misorientation of grains), strain variation and finite layer thickness. However, rocking curve measurements cannot discriminate mosaicity from lattice strain. Thus, analysis in reciprocal space maps (RSM) can be performed to circumvent this limitation by combining a symmetric scan with an asymmetric scan.

3.2.3 SIMS analysis

Many tools commonly used in our field are meant to detect trace-level contaminants. Amongst them, analytical techniques based on mass spectroscopy necessitate removal of material and are therefore considered as destructive. It is precisely the case for Secondary Ion Mass Spectroscopy (SIMS) which is an extremely sensitive technique employed to perform a thorough analysis of components of a sample.

Basically, a primary beam of ions is focused onto the surface of a material to

sputter elements in the form of neutral and ionized atoms and molecules, as illustrated in Fig. 22. Charged elements are then accelerated in a mass spectrometer and detected according to their mass-to-charge ratio [9].

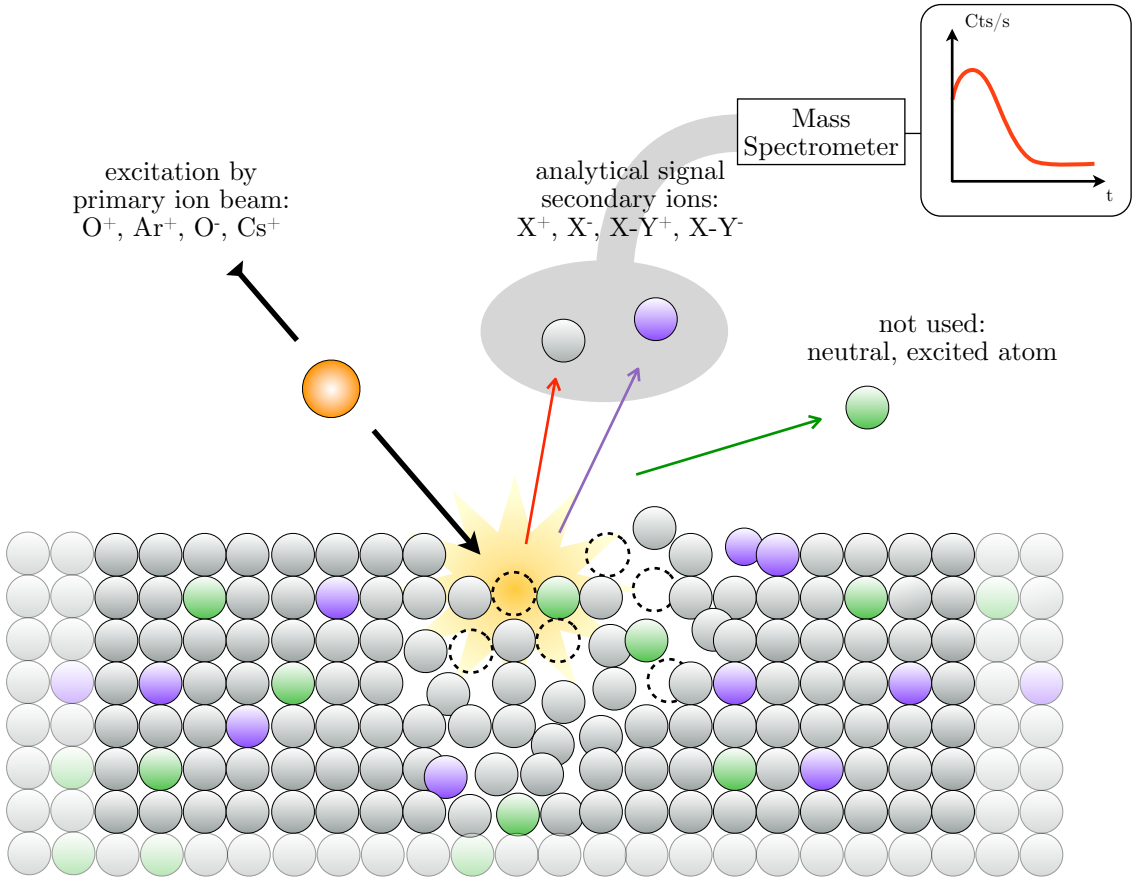

Figure 22: The principle of Secondary Ion Mass Spectroscopy.

Using SIMS, one gets a depth profiling of elements in the layer. Its level of detection, i.e. parts-per-million to parts-per-trillion range, makes it an indisputable way to reveal the presence of any dopant or impurities.

3.2.4 The PL setup

To characterize nitride semiconductor structure grown at our lab, a lab focusing on photoluminescence characterization has been established. Specifically, nitrides such as InN, GaN, and AlN have bandgap energies of 0.7 eV, 3.4 eV, and 6.2 eV, respectively,

which require wavelengths below 1550nm, 364nm, and 200 nm respectively in order to produce luminescence. Thus a light source in the UV range was necessary. I have been in charge, during my Ph.D., to setup a photoluminescence bench. The goals was to create a UV photoluminescence setup capable of performing measurements at room and low temperatures, perform some characterization experiments on nitride-based semiconductors, including structures of BGaN grown on GaN and AlN, and establish methods and programs that can quickly and accurately process the data. At the early stage, design of the setup was done by Pr. Sirenko with help of Ph.D. student Peter Bonanno. I had been involved when the lab itself had to be prepared to welcome the bench. For the testing and measurements on the bench, I have been helped by Chris Bishop (now Ph.D. student).

3.2.4.1 The laser

The source laser is a continuous-wave argon-ion laser *Innova 90C FreD* from Coherent. The photon source is a plasma Argon tube that creates light at the characteristic lines of Argon and reflects inside the laser housing between the back mirror and the output mirror. Emitted fundamental wavelengths are in the range of 457.9-528.7nm (visible range) and the maximum output power could be up to 5W.

A prism in the back is meant to select a single wavelength (e.g. 488 nm), and the output mirror assembly contains a intra-cavity BBO frequency doubling crystal, which will double the frequency and produce a continuous wave light source at one of seven possible frequencies in the range of 229-264.3nm (deep UV range). Also included in the output mirror assembly is a light pick-off, which filters the satellites by deflecting most of their intensity out of the laser line. What exits the beam is up to around 100 mW of the main 244 nm color plus a highly diminished set of satellites.

In order to prevent overheating, the laser was cooled by water through a chiller located in a separate room. In addition, the BBO crystal is continuously heated at

50°C and is under a flux of nitrogen gas to prevent humidity to deteriorate the crystal.

3.2.4.2 The setup

A schematic of the setup is shown on Fig. 23. The laser beam is firstly filtered through a monochromator to remove wavelengths other than 244 nm. The UV beam obtained is then focused by a lens onto the sample that is held by a sample holder for room temperature measurements. Thus, the luminescence originating from the sample is analyzed by a Horiba Jobin Yvons iHR 550 spectrometer equipped with a Synapse CCD detector and photomultiplier tube.

Data is eventually treated with *Labspec* software using a computer which also controls the spectrometer. Different diffraction gratings are available within the spectrometer for different wavelength ranges depending on desired results. Moreover, a standard He-Ne laser is employed to perform a *back-alignment*. Its beam is indeed used to follow the inverse path of the *luminesced* light and obtain a beam spot on the sample. Hence, the UV beam must be precisely targeted on the very same spot to maximize the quantity of photons reaching the CCD detector and get the best contrast.

3.2.4.3 The cryostat

To perform low temperature measurements, a *Janis Research* VNF-100 cryostat is used at the place of the sample holder. A Varian TPS-compact turbo pump creates a vacuum in the cryostat jacket down to 10^{-5} mbar. The supported cryogenic fluid is liquid nitrogen (or LN_2) which allows to reach temperatures down to 66K. A schematic of the cryostat is shown in Fig. 24. The needle valve is thus used to control the introduction of LN_2 inside the chamber. Two temperature sensors, one situated at the bottom of the chamber, in contact with the liquid, and another, in contact with the sample holder, are connected to a temperature controller (*LakeShore* model 331).

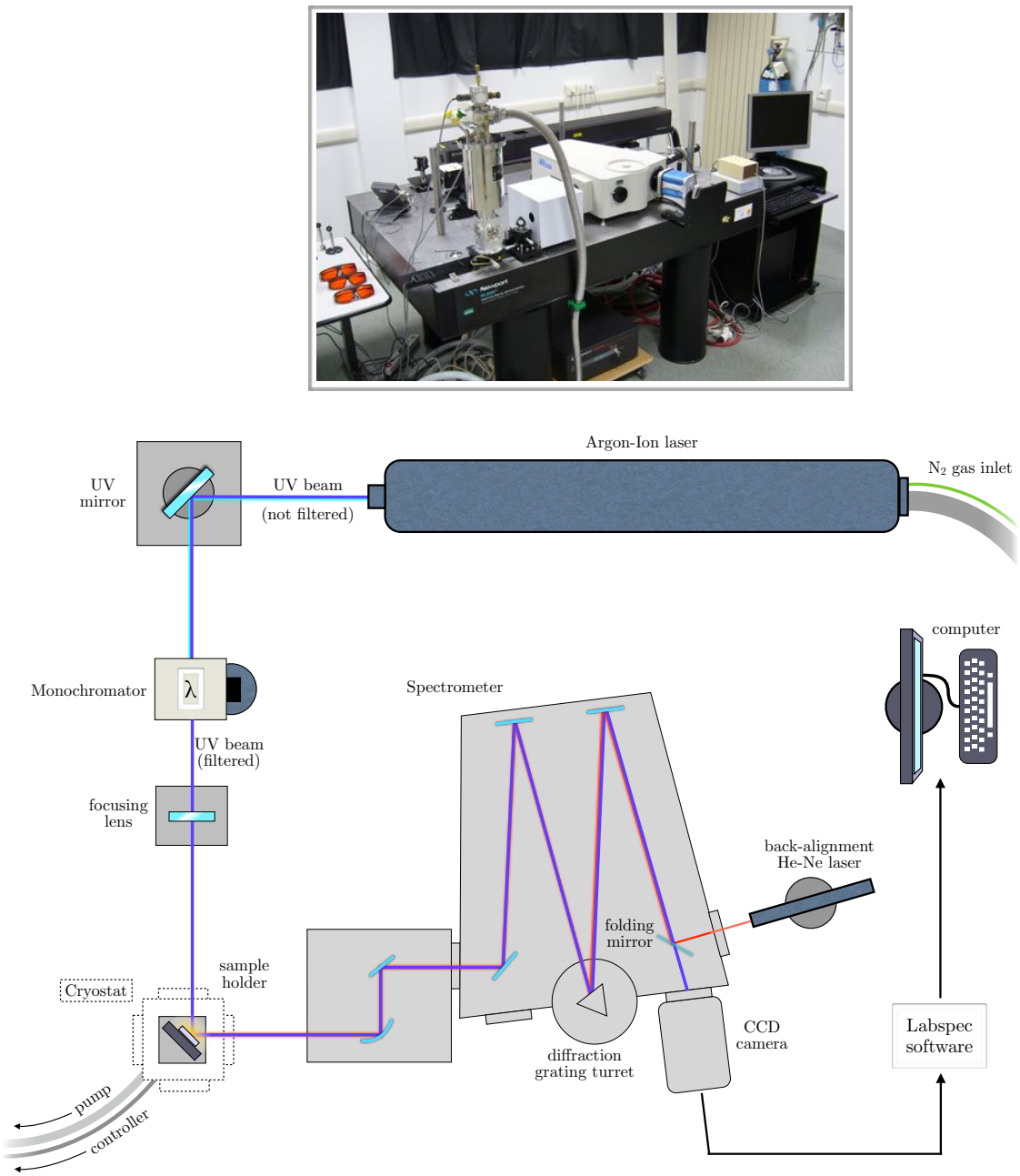

Figure 23: Schematic of the photoluminescence setup used in our lab.

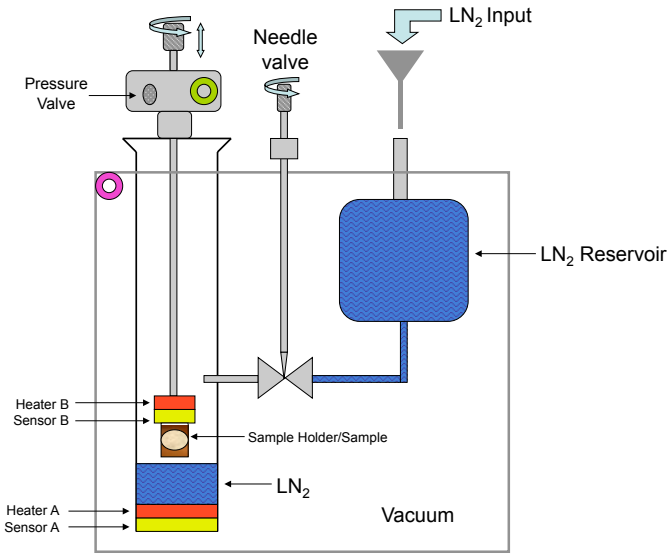

Figure 24: Operating mechanism schematic of the LN_2 Janis Research VNF-100 cryostat (credit to Chris Bishop)

3.2.5 PL measurements on standard substrates

Measurements were performed on a standard GaN substrate usually used for our HEMT growths (see Table 3 in Section 6.2.1). The laser was operated at 488 nm and, after the *doubling*, the output power at 244 nm was up to 100 mW. The angle of incidence of the beam is 45° off the surface normal. Considering a minimum diameter of the spot of 0.6 mm, the power density is up to 35 W/cm^2.

The room temperature measurement showed a distinctive yellow glow when observed with naked eye. Fig. 25(a) shows the distinctive peak of GaN at 361.5 nm (also known as the UV transition). We normally considered GaN's bandgap to be at 3.39 eV, which corresponds to 365.7 nm, to be compared to the theoretical value at 361 nm (or 3.437 eV at 300K [62]). The rest of the photoluminescence, spanning from 400 to 700 nm, is due to yellow luminescence as reported in the literature [63]. Usually centered around 2.2 eV, it corresponds to defect-assisted transitions, originating from defects and impurities, and which are observed with growths performed

with both MOVPE and MBE. Moreover, the other intense peaks, especially the one observed at 488 nm, correspond to the laser beam which is not perfectly filtered by the monochromator.

For low temperature measurements, the sample was mounted on the sample holder of the cryostat using silver paste to ensure proper thermal conduction at the interface. After reaching a cryogenic temperature within the chamber, the sample was firstly immersed into LN_2 which was then slowly evaporated to obtain a stable temperature of 77K. Fig. 25(b) exhibits indeed the photoluminescence spectra obtained. The 3 peaks (labelled A, B and C) are probably related to impurities or donor- or shallow-acceptor bound excitons. The major peak, related to the GaN, is situated at 355.5 nm. In fact, the temperature dependance of GaN, based on Varshni's empirical formula, is given by the following equation [62]:

$$E_g(T) = 3.503 - \frac{5.08\,.\,10^4 \times T^2}{996 - T} \quad \text{in eV}, \tag{14}$$

with T the temperature in Kelvin. Hence, the theoretical value expected for the major UV transition is at 354 nm for 77K (corresponding to 3.502 eV), which is very close to the experimental value above. Beyond excitons, for energies below, the yellow luminescence is observed again, but a additional set of wavelengths around 410 nm appears. This blue luminescence originates as well to defect-related emissions, usually due to donor impurities [64, 65].

Lastly, for both spectra, a modulation of the curve, with multiple maxima and minima, can be noticed. As our CCD detector is Front-Illuminated, we do not suspect interference issues that could occur with a back- illuminated CCD. This phenomenon, that has already been observed on AlGaAs structures [66], is due to Fabry-Perot interferences that add up to the structure of the luminescence. The large difference of refractive index between the GaN epi-layer and the substrate (e.g. GaN on Sapphire) on one hand, and with the air on the other hand, leads to multiple reflections of light, it is the Fabry-Perot effect that acts as a filter on frequencies. We suppose that the

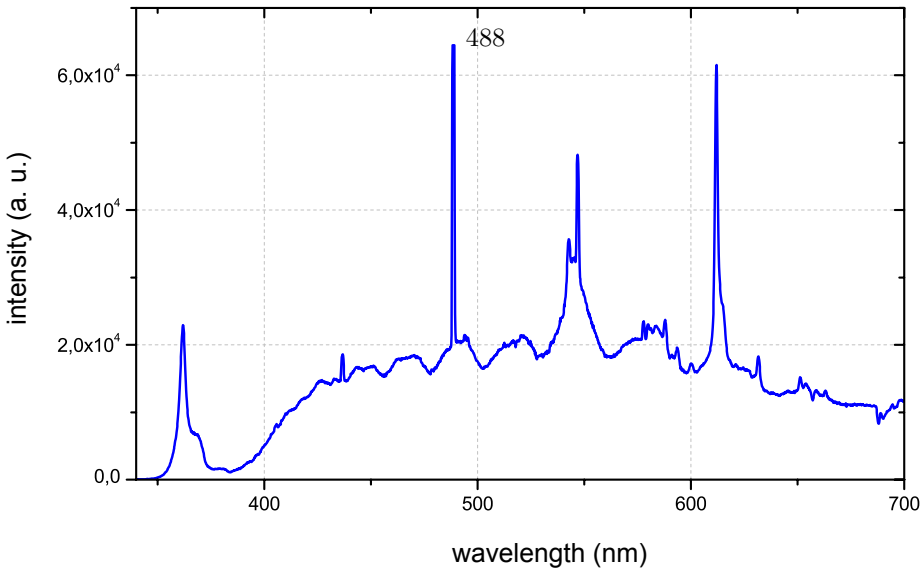

(a) Room temperature ($\sim$ 295K)

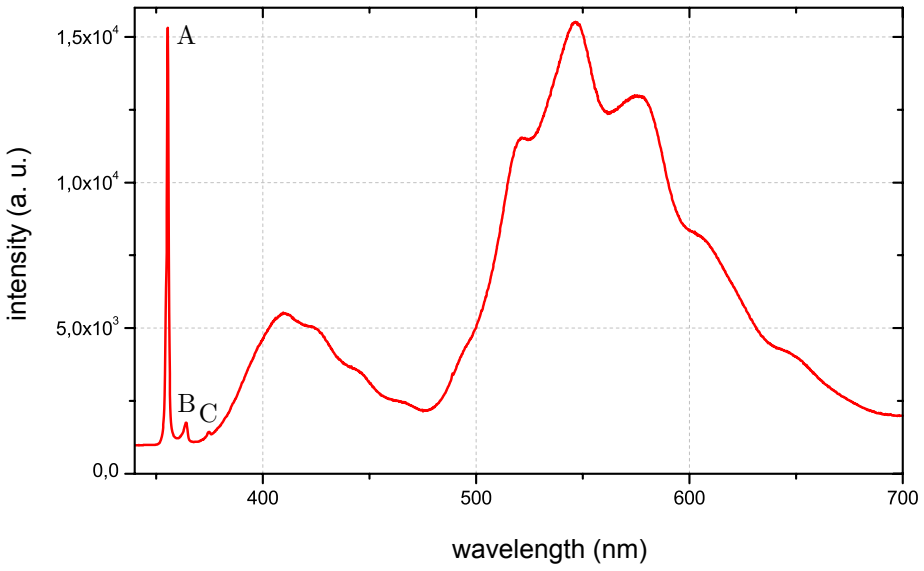

(b) Low temperature (77K)

Figure 25: PL measurements, using a 244 nm laser beam, on a standard semi-insulating GaN Fe-doped substrate on sapphire (STINS GaN09542) at both room and low (77K) temperatures, from 300 to 700 nm. The GaN peak is observed in both figures along with the yellow luminescence characteristic of nitrides. At low temperature, there are 3 clearly visible peaks (labelled A, B and C). The major peak is related to the GaN and peaks B and C are probably related to impurities or donor- or shallow-acceptor bound excitons.

incoherent travel of the light in the Sapphire and the GaN template of about 3.5 μm is the prevailing medium for this interferometric effect. An interference function can therefore be computed as reported in the literature [67]. According to the basic theory of the well-known Fabry-Perot interferometer, the transmission is made up of equally spaced peaks in frequency, the spacing given by the following formula [68]:

$$\Delta\lambda = \frac{\lambda_0^2}{2\,n\,l\cos\theta}, \tag{15}$$

with λ_0, the exciting wavelength, n, the refractive index, l, the thickness of the medium, and θ, the angle of incidence. The exciting wavelength for our case was 244 nm and the angle of incidence was estimated at 60°. Moreover, according to Fig. 25, the separation between two maxima (or minima) due to the Fabry-Perot effect is approximately 20 nm. As far as the refractive index is concerned, it can be derived using a Sellmeier law describing only the real part as a function of the wavelength [67]:

$$n = \sqrt{a + \frac{b\lambda^2}{\lambda^2 - c^2}}\,, \tag{16}$$

with $a = 5.003$, $b = 0.423$ and $c = 327$ nm. For a wavelength of 244 nm, the refractive index is 2.11. Hence, we can compute from Eq. 15 an estimated thickness l of 2.82 μm. Thus, we are indeed on the order of magnitude of the template's thickness, i.e. the bulk GaN, which is responsible for the added interference function observed in our measurements.

3.2.6 The Transmission Electron Microscopy

Several tools covered earlier are essential to study the structural quality of our samples. However, Transmission Electron Microscopy (TEM) enables to analyze more precisely the crystal matrix down to the atomic scale thanks to high-resolution microscopic images. Such imaging can be essential to assess correct definition of interfaces

between materials, find orientations or chemical compositions, study the different elastic and plastic relaxation modes and all of these at a sub-nanometer scale. There are several techniques that can be employed using this tool: standard imaging, high-resolution imaging, X-ray microanalysis and quantitative contract analysis.

Measurements were performed at our partner lab at the *Laboratoire de Photonique et de Nanostructures* (CNRS/LPN). Fig. 26 presents the schematic principle of the instrument used for analyzing our samples. Basically, a source emits a primary beam of electrons that acquire a high energy (acceleration up to 300kV of voltage) to be focused on a sample. Electrons are then transmitted through the thin sample and scattered. The probability of an electron to pass through depends on the nature of the material or atoms (in the case of high resolution TEM). A subsequent assembly of magnetic and projection lenses, as well as apertures, allows to obtain a magnified image using a phosphorescent plate (see image in Fig. 26).

Compared to Scanning Electron Microscopy (SEM) that is meant for surface imaging, TEM is mostly used to observe cross-views of the samples. Thus, to examine semiconductor structure grown at our lab, a specific preparation must be realized. To reach a sufficiently thin section below 100 nm, we employ a Focused ion beam (FIB) method performed by our partner lab at the IEMN.

In addition, Scanning Transmission Electron Microscopy (STEM) measurements were also performed at LPN. STEM differs from regular TEM by focusing the primary electron beam into a narrow spot, which is in turn swept over the surface of the sample. This technique enables us to use both high angle annular dark-field (HAADF) and energy dispersive X-ray (EDX) spectroscopy.

3.2.7 The Scanning Electron Microscopy

As indicated by its name, Scanning Electron Microscopy allows to scan over the surface of a sample with an electron beam to eventually obtain an image. Compared

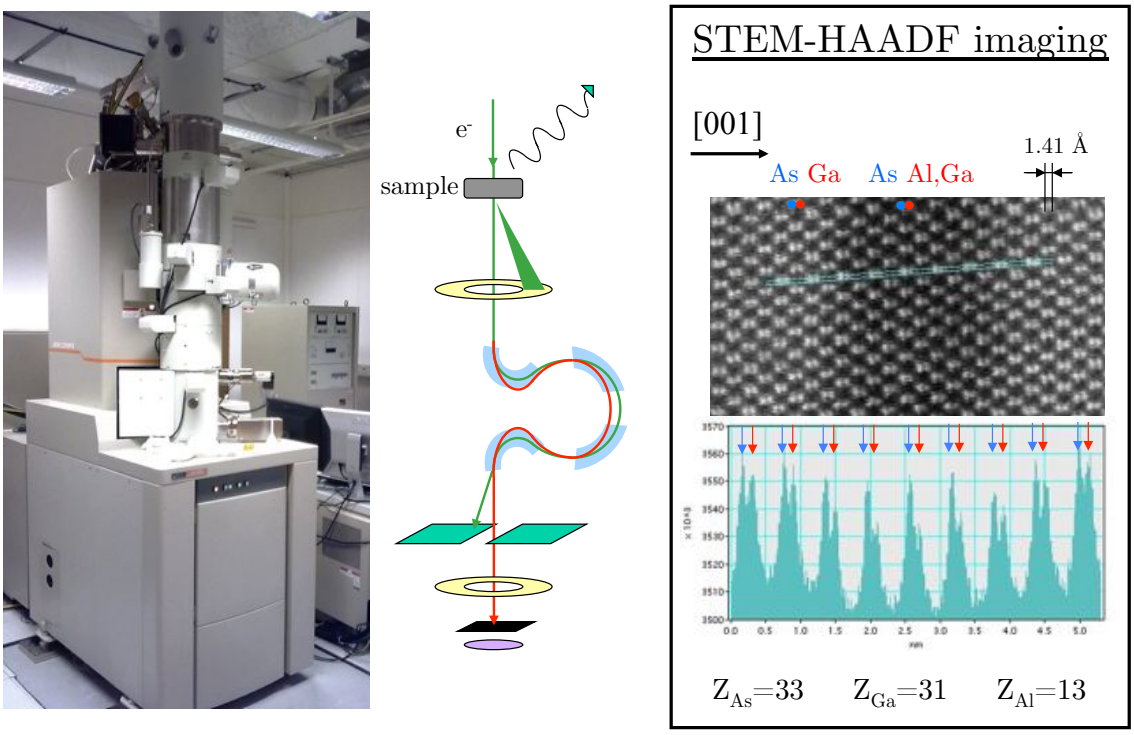

Figure 26: TEM instrument *Jeol 2200FS* at LPN (left), schematic views of its microscopy principle (center) and illustration with a HAADF imaging (right) (courtesy of LPN).

to TEM, SEM is meant at surface imaging but can render 3 dimensional images. In addition, the magnification can only reach levels up to 200.000 times compared to 500.000 times for TEM.

Fig. 27 shows the schematic of the instrument's principle where main constituting electron optics are represented. The source image generates electrons inside a vacuum that are focused through electron optics on the sample. The fine beam is then rastered over the specimen and, if we disregard the fine analysis of all interactions happening, electrons scattered from the surface are sensed by a detector.

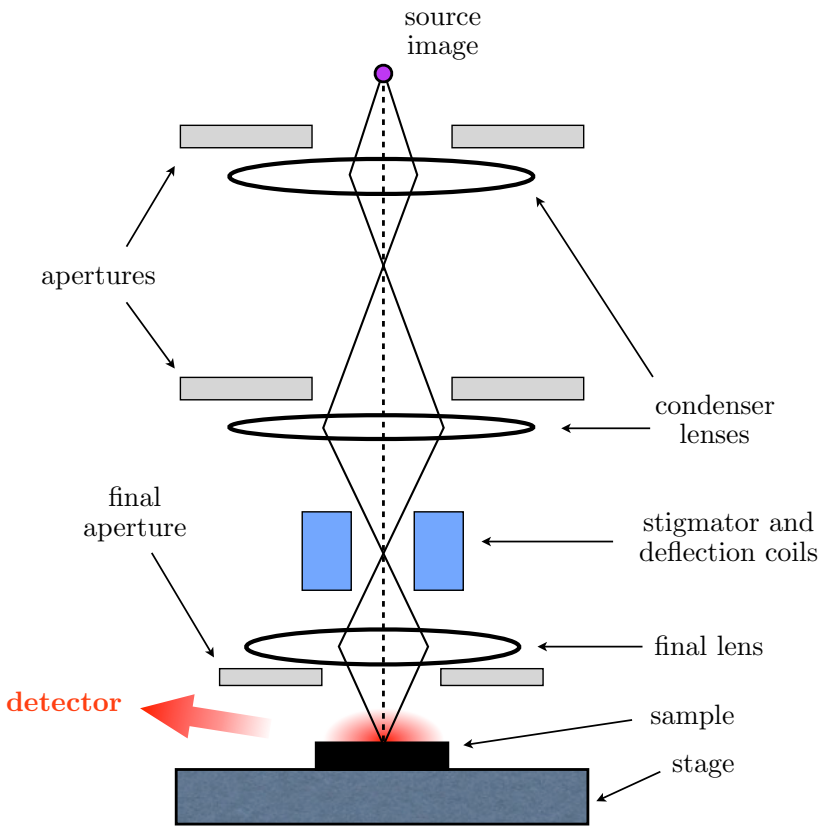

Figure 27: Schematic of SEM principle with constituting electron optics (inspired from [9]).

3.3 Electrical characterization of HEMTs

3.3.1 Hall effect

When an electric current flows through a conductor or a semiconductor, it corresponds to electrical charges q in movement with a velocity v. However, if these very same charged particles are in presence of a perpendicular magnetic field, as depicted in Fig. 28 for the case of electrons, they experience a magnetic force, part of the Lorentz force, as follows:

$$\overrightarrow{F_L} = q\overrightarrow{v} \wedge \overrightarrow{B},$$

which deviates laterally their path towards side faces of the conductor. Hence, at equilibrium the difference of accumulated charges on both opposite faces leads to an electric field as follows:

$$\overrightarrow{E_H} = -\overrightarrow{v} \wedge \overrightarrow{B} \quad \text{with} \quad E_H = \frac{V_H}{w},$$

which intends to balance the influence of the magnetic field $\overrightarrow{B}$.

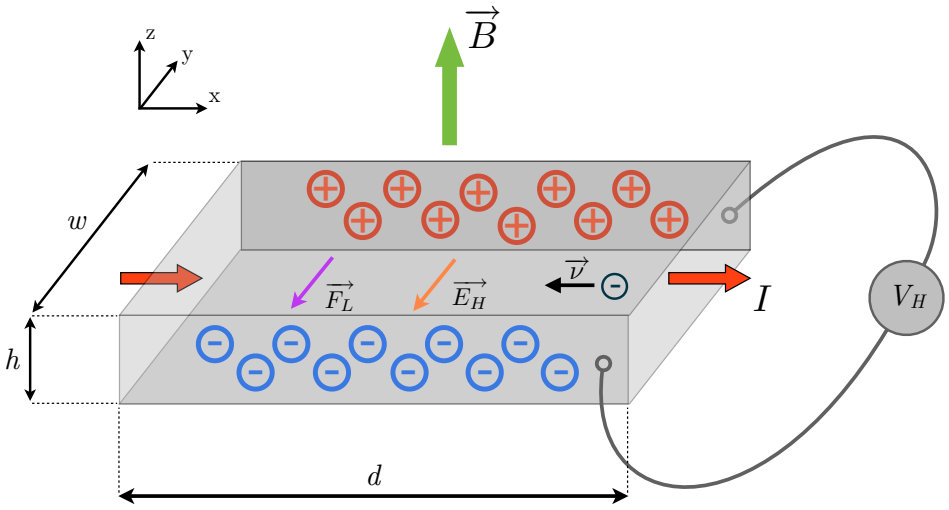

Figure 28: Schematic of the Hall effect occurring in semiconductor samples under a magnetic field (B) (Lorentz force components are represented for the case of electrons).

As $\overrightarrow{E_H}$ and $\overrightarrow{F_L}$ cancel each other, we infer the following equation:

$$V_H = R_H.\frac{I.B}{h} \quad \text{(in V)} \quad \text{with} \quad R_H = \frac{1}{n.e} \quad \text{(in m}^3\,\text{C}^{-1}\text{)}, \tag{17}$$

with n, the number of carriers per m^3, v, the velocity of electrons and e, the charge of an electron (i.e. negative). As a consequence, the bulk carrier density can be easily computed by performing a Hall measurement. When dealing with the sheet density, that value would be:

$$n_s = \frac{IB}{eV_H} \quad (\text{in m}^{-2}). \tag{18}$$

Furthermore, we can infer the mobility of carriers by mean of the Hall effect occurring in semiconductors. Using Eq. 17 for the bulk carrier density and the definition of mobility for electrons, we find:

$$\mu_n = -\sigma_n \, R_H = \frac{\sigma_n}{e \, n} = -\frac{\sigma_n V_H \, h}{IB} \quad (\text{in m}^2.\text{V}^{-1}.\text{s}^{-1}), \tag{19}$$

where σ_n is the electron conductivity that can be obtained by a resistivity measurement. Thus, we can compute the sheet density using Eq. 18.

3.3.2 The Van der Pauw technique

To know the sheet resistivity on uniform thin films as semiconductors, which is a critical property for electrons' movement, a widely employed technique was established by Van der Pauw [69]. Conversely to Hall measurements, there are no specific geometry required but simply four ohmic contacts on an arbitrarily shape sample.

As illustrated in Fig. 29, these contacts are preferably situated in corners of the samples. The figure gives schematic of the Van der Pauw method for a rectangular configuration. Hence, resistances indicated as R_A and R_B can be determined by performing voltage and current measurements between considered contacts (refer to equations displayed in the figure). Knowing these characteristics resistances, one can calculate the sheet resistivity R_S by solving the following equation:

$$\exp(-\frac{\pi R_A}{R_S}) + \exp(-\frac{\pi R_B}{R_S}) = 1. \tag{20}$$

We can then derive the bulk resistivity ρ and the conductivity σ_n as follows:

$$\rho = \frac{1}{\sigma_n} = R_S \, h \quad (\text{in } \Omega.m^{-1}), \tag{21}$$

with h being the thickness of the sample as depicted in 28. Now, if we go back to Hall measurements, using this result, we can eventually compute the mobility from Eq. 19.

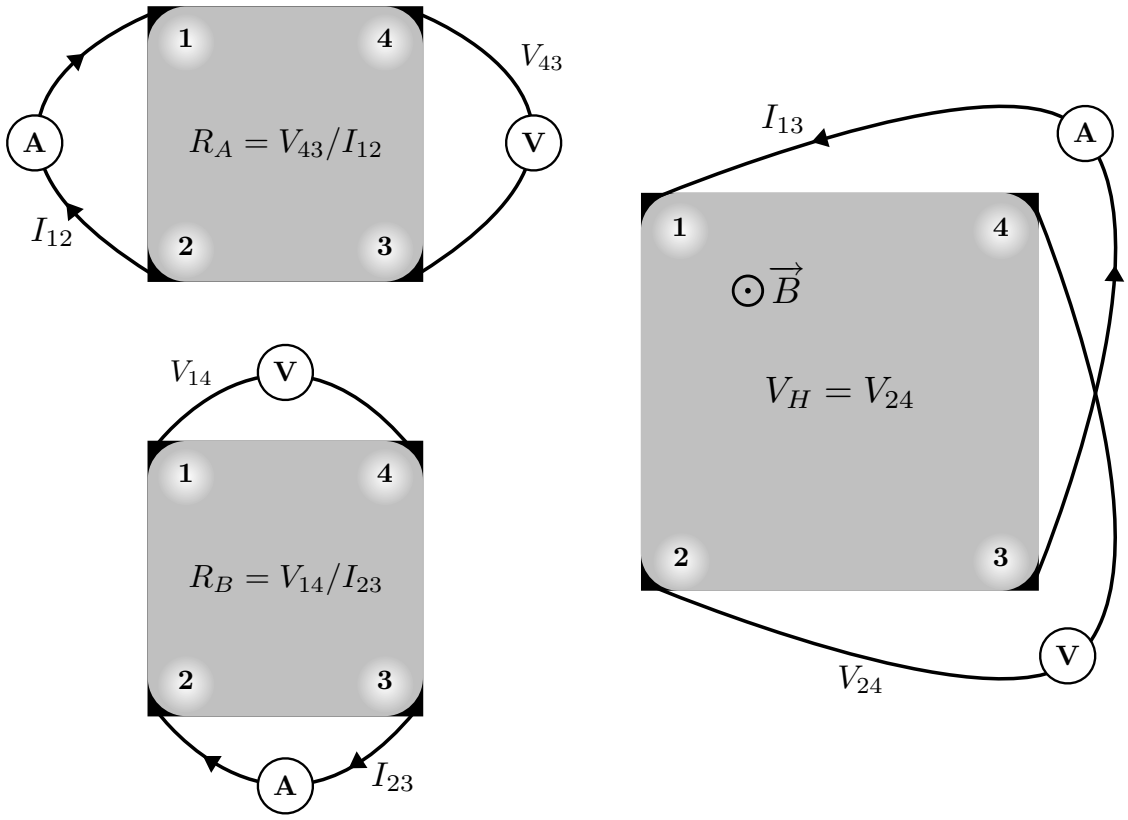

Figure 29: Van der Pauw method.

Another way to relate Hall measurements to Van der Pauw method is to perform a measurement as depicted in the third schematic of Fig. 29. While applying a constant perpendicular magnetic field, this configuration allows to find the Hall voltage V_H (or V_{24}) by imposing a current between two opposite terminals and reading the voltage between the two others. Thus, one can derive the sheet carrier density using Eq. 18.

3.3.3 Capacitance-voltage measurements

Capacitance-voltage testing is a very common measurement giving a straightforward characterization of the 2DEG. It allows to monitor the capacitance while the structure

is driven by a gate bias. There are three modes of operation: accumulation, depletion, and inversion (see Fig. 30).

The accumulation mode occurs when the gate bias is positive ($V_G > 0$). Majority carriers, or electrons, are therefore attracted to the gate and accumulate in the 2DEG. Consequently, the measured capacitance is high as the GaN has a conductor behavior compared to AlGaN. The maximum capacitance corresponds to the AlGaN behaving as a dielectric.

Conversely, when the gate bias is negative ($V_G < 0$), a depletion region appears with electrons pushed away and the capacitance starts to decrease. If the bias is further decreased ($V_G << 0$), the inversion mode occurs with the accumulation of minority carriers, or holes. The minimum capacitance corresponds to the doping concentration of GaN.

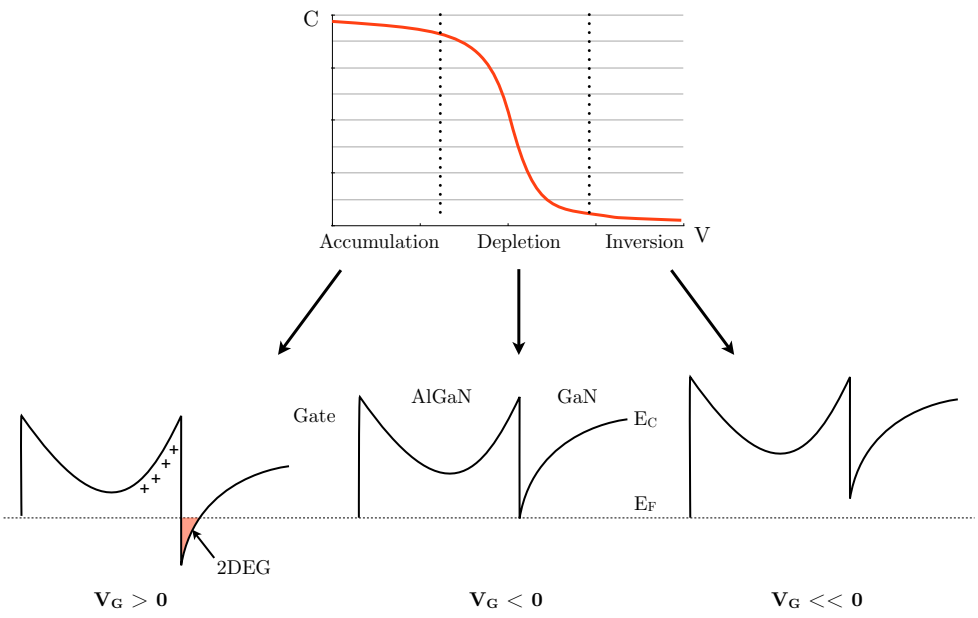

Figure 30: Principle of capacitance-voltage measurements.

Hence, the sheet carrier density of the 2DEG can be derived using values obtained with the accumulation mode. Moreover, the voltage, at which occurs the transition between the maximum and minimum capacities, corresponds to the pinch-off voltage

of the structure. In addition, during depletion modes, any trap, defect or donor impurity inside the depleted area will be revealed by the capacitor. Values obtained are typically in the range of the nano- to picofarads. In fact, low frequency measurements (a few tens of kHz) are a reliable way to reveal traps, due to their slow charging, and usually existing in the buffer of HEMT structures.

3.3.4 Mercury probe measurements

Normally, to perform capacitance profiling of a device, contacts must be fabricated onto the structure which requires specific process, at high temperature and time-consuming. To circumvent this, we use mercury probes that consist in droplets of mercury deposited on the surface, hence ensuring current flow [70, 71, 72]. It is a non-destructive and fast technique working at room-temperature, given that mercury is easily removable with allegedly no damage or residue [73].

Thus, a small ball of mercury is held at the end of a glass capillary tube. The typical size of the droplet is in the order of the μm (e.g. 7 μm). In order to better control the area of contact (related to mercury's viscosity), special precautions should be considered regarding temperature, Hg purity, etc. [74].

These contacts can be employed to perform Capacitance-Voltage measurements that are decisive, for instance, to detect a 2DEG in a HEMT structure.

CHAPTER IV

BORON-BASED NITRIDE ALLOYS

Exploring new materials and their properties is of paramount importance to broaden the range of applications. In most cases, this translates into reaching new bandgaps or lattice parameters that dictate the mechanical, electrical or optical behavior of a device. It allows to perform band engineering and obtain new wavelength or new electrical properties. Among nitride wide-bandgap semiconductors, a new class of materials has arisen based on boron alloying.

4.1 Introduction to boron-based nitrides

When only several percents of boron are incorporated, boron-containing nitride materials, BGaN for instance, possess all the distinctive characteristics of nitride materials [75]. These new materials have only been studied by a few groups but several applications are foreseen. First, alloying could be adapted so that BGaN or BAlN layers are lattice-matched to SiC (with 17% and 5% of boron, respectively) or AlN templates (with 8% of boron for BGaN), hence drastically diminishing the density of dislocations in the buffer. Second, BAlN is a potential candidate for future UV-range laser devices and Bragg mirrors with fewer periods for vertical-cavity surface-emitting laser (VCSEL) because of a noteworthy large refractive index [76]. The possibility to have a larger refractive index contrast by only introducing a few percent of boron alternatively in multiple Bragg pairs would lead to a higher reflectivity and bandwidth.

The growth of boron-based nitrides is however still challenging and needs more technological maturity to increase the boron content. Due to a large miscibility gap, the theory predicts a maximum value of 5% alloying of boron in BGaN [77]. Research in our laboratory has allowed us to get up to 3.6% composition using MOCVD growth

[11], and 4.6% using MBE growth [78]. Nevertheless, it has been shown that very interesting properties are observable with only a few percents.

It was recently demonstrated that, for a small boron alloying, a strong decrease of the BGaN bandgap is observed (about 150 meV from 0 to 1.8% of boron observed with the optical bandgap) [10]. More specifically, BGaN exhibits a bowing compared to a linear interpolation between GaN and BN bandgap values. In fact, knowing this value is critical for simulation as we performed band-engineering to enhance performances of devices (see Chapter 5). As depicted in Fig. 31, BN alloys with conventional nitrides are wide-bandgap semiconductors. Most usual nitrides are shown with their respective bandgaps and lattice parameters. The branch corresponding to BGaN (linking GaN to BN) was deliberately represented with a bowing, and not straight as per Vegard's law, which corresponds to the results obtained by our group. However, this bowing is verified only for little boron alloying, the rest of the branch is extrapolated and is represented only for illustration. The two others branches related to BAlN and BInN are showed for the same purpose as well and are not based on concrete results. We can observe that BGaN can be lattice matched to SiC for approximately 17 % of boron and BAlN as well but only for about 5 % of boron. Besides, this suggests that the quaternary BAlGaN could be either lattice-matched on SiC of AlN while allowing band-engineering with high bandgap energies.

Moreover, BGaN materials also show very interesting electrical properties [14]. Studies have reported a strong correlation between the electrical resistivity and the boron composition between 0 and 1.75%. A strong raise of the resistivity was observed in connection with the decrease of the n-type carrier concentration associated with the increase of boron composition. Furthermore, this resistivity enhancement occurred with an increase of the mobility of the carriers, which indicated a good crystalline quality of the BGaN layers studied[1].

[1] As confirmed by polarized Raman spectroscopy.

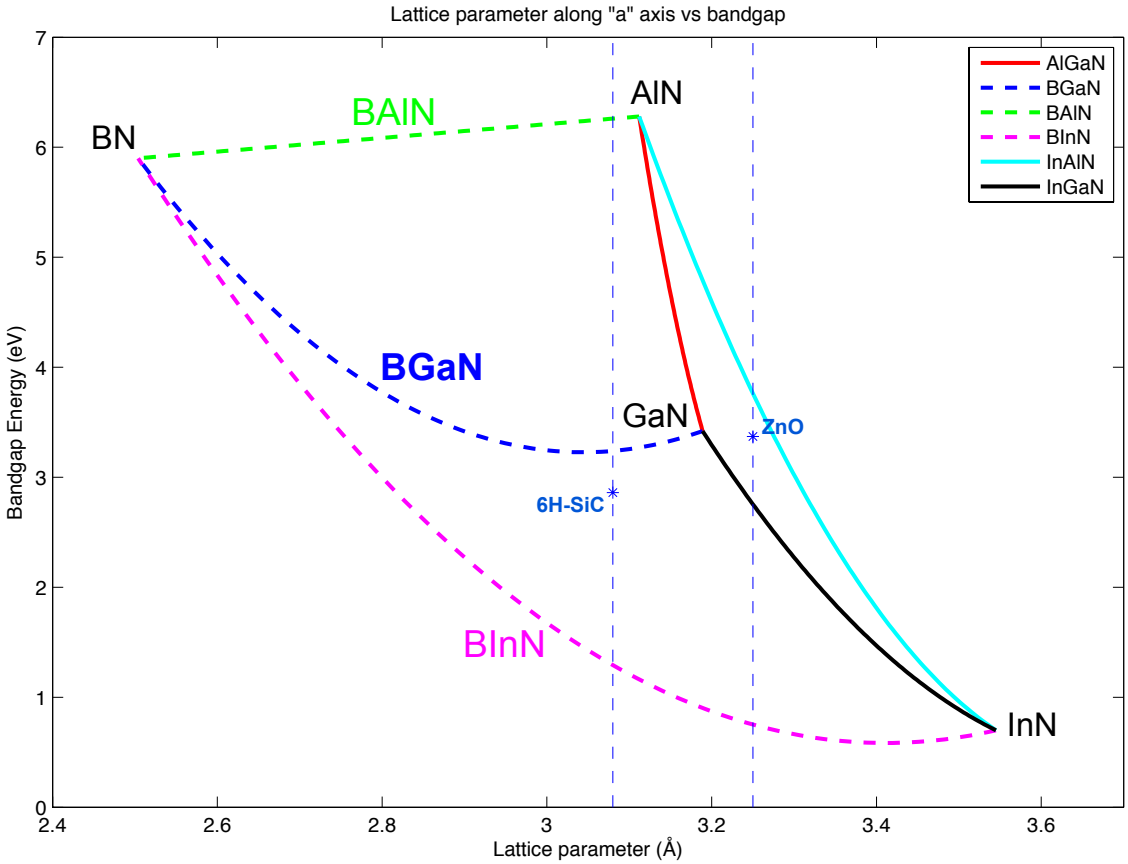

Figure 31: Bandgap versus lattice parameter with representation of usual nitrides compounds (straight lines) and boron nitride materials (dashed lines). Boron alloys-related branches are represented only for illustration and are not based on concrete results. The bowing of BGaN translates results obtained in [10].

4.2 Growth of BGaN

Regarding experience gained at our lab, the incorporation of boron in epitaxial nitrides has been extensively studied by our group [12], notably with $B_xGa_{1-x}N$. Layers are grown on GaN templates by low pressure MOVPE at high temperature, similarly to GaN or AlGaN. Typically, parameters are set to have the temperature in the 1000-1050° C range while the pressure is kept between 100 and 450 Torr.

As far as morphology is concerned, there is an optimal thickness beyond which a sudden degradation of the surface morphology is observed [11]. Visually, this phenomenon manifests itself with shinny surface aspect quickly switching to a whitish aspect. Experiments were carried out on a series of BGaN layers grown at a pressure of 450 Torr. The signal from a *in-situ* reflectometer, implemented inside our growth chamber, was monitored. Clearly, the signal degrades beyond the optimum thickness and only exhibits the background noise as illustrated on Fig 32. In Fig. 32 (a), we can remark that, as the TEB/III ratio increases, the sudden drop of the *in-situ* reflectance signal happens earlier, translating a deterioration of the growth at a lower thickness. SEM imaging showed that the degradation is embodied by the appearance of crystallites on the surface once the optimal thickness is reached, hence enhancing the surface roughness. Furthermore, optimal thicknesses derived from growths campaigns at both 100 and 450 Torr are plotted in Fig. 32 (b). Thus, growths of BGaN layers are executed with a thickness below the optimal thickness.

After thickness, the second parameter to be investigated is the boron incorporation. To this end, its insertion within the GaN crystalline matrix is controlled by varying the molar ratio of TEB in the vapor phase, TEB/III. As depicted in Fig. 33, results show firstly that the reproducibility is good at 100 Torr. Data of boron mole fraction in the BGaN layer were derived from high resolution X-ray diffraction using (0002) reflection. In addition, values obtained at 450 Torr demonstrate that increasing the pressure of the reactor allows to introduce more boron in GaN layers.

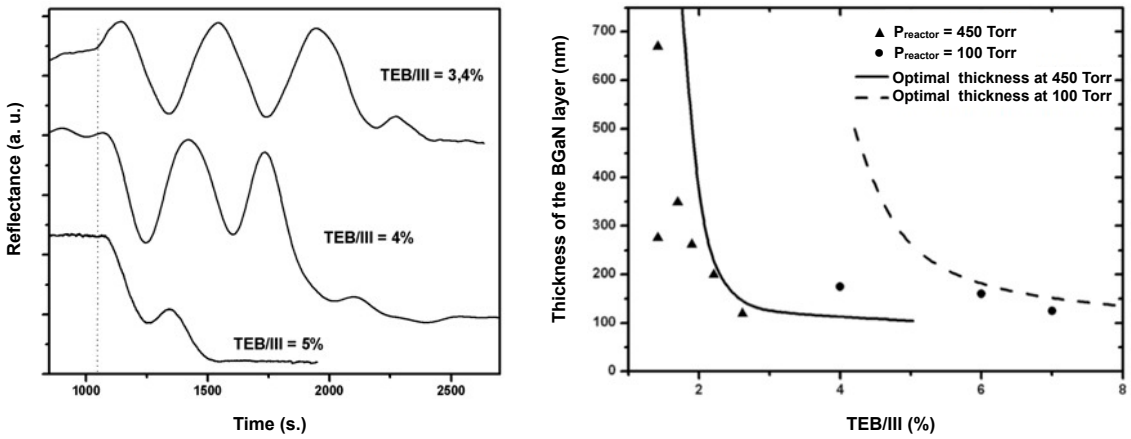

(a) *In-situ* reflectance data

(b) Optimal thickness

Figure 32: (a) Sudden degradation of the surface morphology observed with *in-situ* reflectance for a total pressure of 450 Torr in the reactor at different values of the TEB/III ratio. (b) Optimal thickness evolution as function of the TEB/III ratio for a total pressure of 100 or 450 Torr in the reactor [11].

As a consequence, a maximum value of 3.6 % has been obtained at a pressure 450 Torr.

Analogous experiments were conducted on AlN templates. It was observed that boron incorporation was quite similar and, hence, unrelated to the type of substrate employed. In addition, several SIMS measurements, high resolution X-ray diffraction measurements, along with Raman scattering and infrared spectroscopy measurements corroborate determined values and helped refining growth parameters [11, 79].

4.3 Structural analysis of BGaN layers

As BN's lattice parameter is rather different from usual nitrides, it implies that its introduction within the GaN matrix is quite arduous. Combining this with the fact that its stable crystalline phase is not necessarily wrtzite, unlike other nitride it is alloyed with, it explains why studies showed a limitation in terms of boron content below 5% [77]. It is therefore interesting to perform a fine structural analysis of grown BGaN layers.

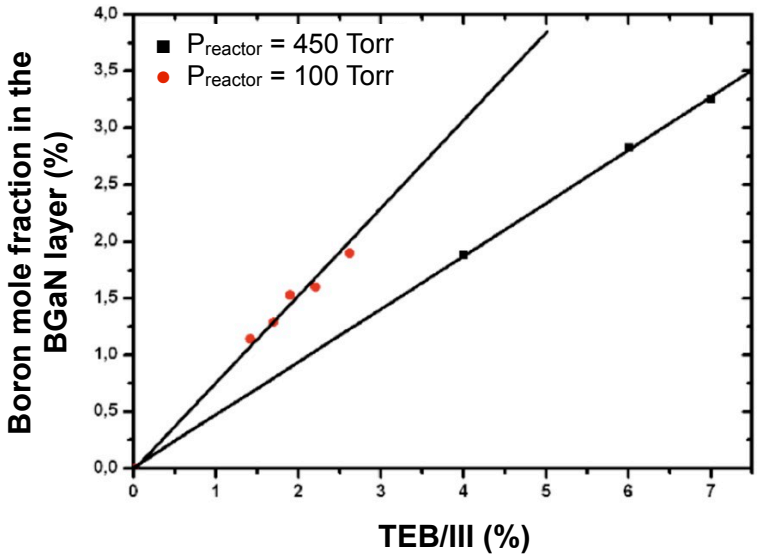

Figure 33: BGaN boron composition (%) versus TEB/III ratio (%) for two different pressures in the reactor [12].

Several BGaN layers of 400 nm thickness were grown on 3.5 μm thick c-plane-GaN/ sapphire templates by MOVPE in our custom-made growth chamber (see Section 3.1.2) with N_2 as carrier gas. The temperature of growth was 1000°C with a V/III ratio of 830 while the reactor pressure was at 133 hPa (100 Torr). To monitor the boron incorporation, we play on the molar ratio of TEB in the vapor phase (i.e. TEB/(TMG+TEB)). We employed HR-XRD $2\theta/\theta$ scans to determine more precisely boron contents of the BGaN samples.

Two samples of different compositions were picked for STEM measurements using HAADF, which has the advantage to be sensitive to the atomic number. Fig. 34 shows results for the sample containing 0.7% of boron. By observing the arrangement of atoms in Fig. 34 (a), a columnar structure clearly emerges with a rough width of 100 nm (coherent with AFM measurements) and a orientation parallel to the growth direction. Thus, the growth is considered 3-dimensional but a relatively uniform contrast leads us to think that there are no compositional discrepancies, i.e. high-boron clusters. Nonetheless, we can reveal the crystal structure patterns using a direct

Fourier transform of the picture, as illustrated in Fig. 34 (b), which is composed of phase patterns of both wrtzite and zinc-blende structures. Thus, the transform distinctly shows that both phases are within the crystal matrix, knowing that zinc-blende aggregates can be enclosed in a wrtzite structure in terms of crystal binding consistency. By filtering the Fourier transform on contributions of zinc-blende phase and applying an inverse Fourier transform, we get Fig. 34 (c) that illustrates zinc-blende insertions in the structure. It can be noticed that it corresponds to a few monolayers.

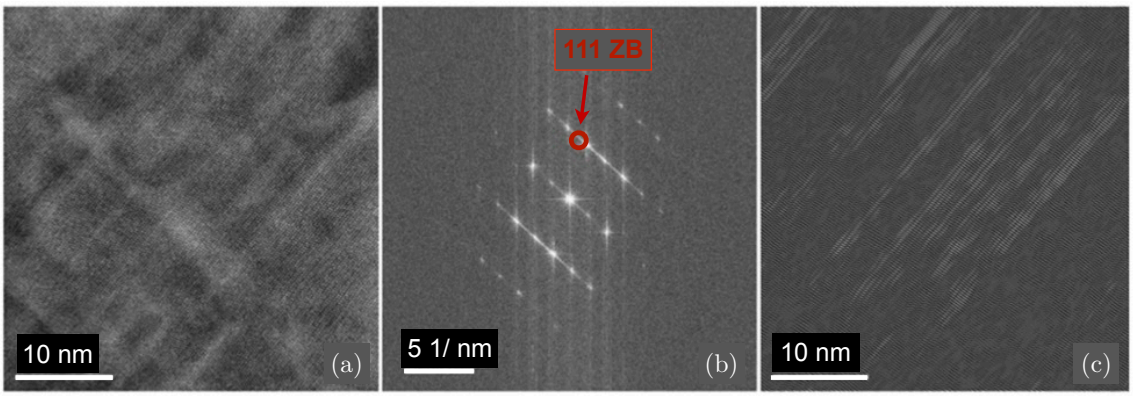

Figure 34: (a): HAADF-STEM picture of a 400 nm thick BGaN layer containing 0.7% of boron. (zone axis is $< 1120 >$) and (b) 2D Fourier transform pattern of the HAADF-STEM image in (a). The wrtzite reflections as well as the zinc-blende one are present. The specific 111 ZB is circled in red. (c) The BGaN layer image reconstructed by mean of inverse Fourier transform evidences zinc-blende insertions in the BGaN material [13].

Figure 35 is an image obtained with HAADF-STEM technique on the sample containing 1.7% of boron. The arrangement exhibits the distinctive columnar pattern that also appears in the previous sample. These columns are 100 nm wide and stretching along the growth axis. A *chevron* shape is observed in layers stacking: it is due to small disorientations between the columnar grains observed in this boron rich layer. Furthermore, the structure is teeming with nano-scale clusters as pointed by arrows in the figure. Analyses show that their spread is quite uniform, with a mean

size of 3 nm in diameter. An average density of $10^4\,\mu m^{-3}$ was determined, which corresponds to 5% of the total crystal volume.

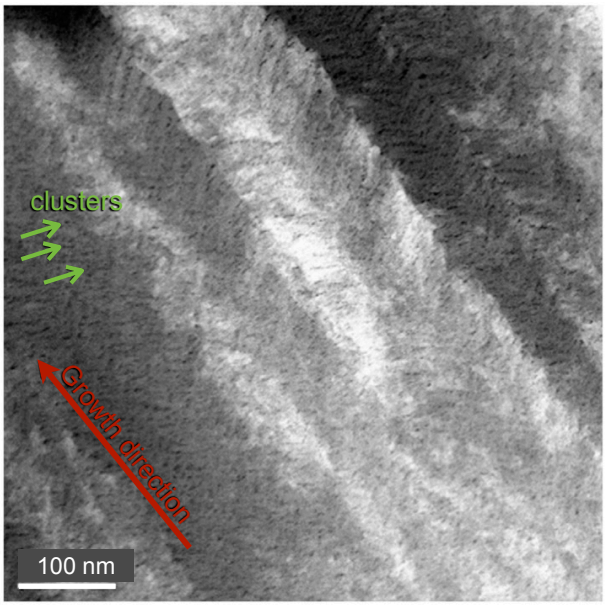

Figure 35: HAADF-STEM picture of a 1 mm thick BGaN layer containing 1.7% of boron [13].

Figure 36 (a) is example of image acquired by HAADF-STEM on one of the clusters witnessed in Fig. 35. A direct Fourier transform of image leads to Fig. 36 (b). Once more, both wrtzite and zinc-blende phase patterns are distinguishable, with spots located by blue and red circles, respectively. As seen previously, if inverse Fourier transforms are computed on each group of spots, we obtain Figs. 36 (c) and (d) representing zinc-blende and wrtzite phase, respectively. It is interesting to note that both areas are complimentary to each other, which supports a hypothesis of zinc-blende clusters inserted in a surrounding wrtzite structure.

A question remains as to why a darker area appears in Fig. 36 (a) whereas it does not fit with phases spreadings observed earlier. If we refer to TEM principle, it should coincide with an element of lower atomic number. A possible answer is that it is an evidence of presence of boron-rich compounds, with contents believably up to

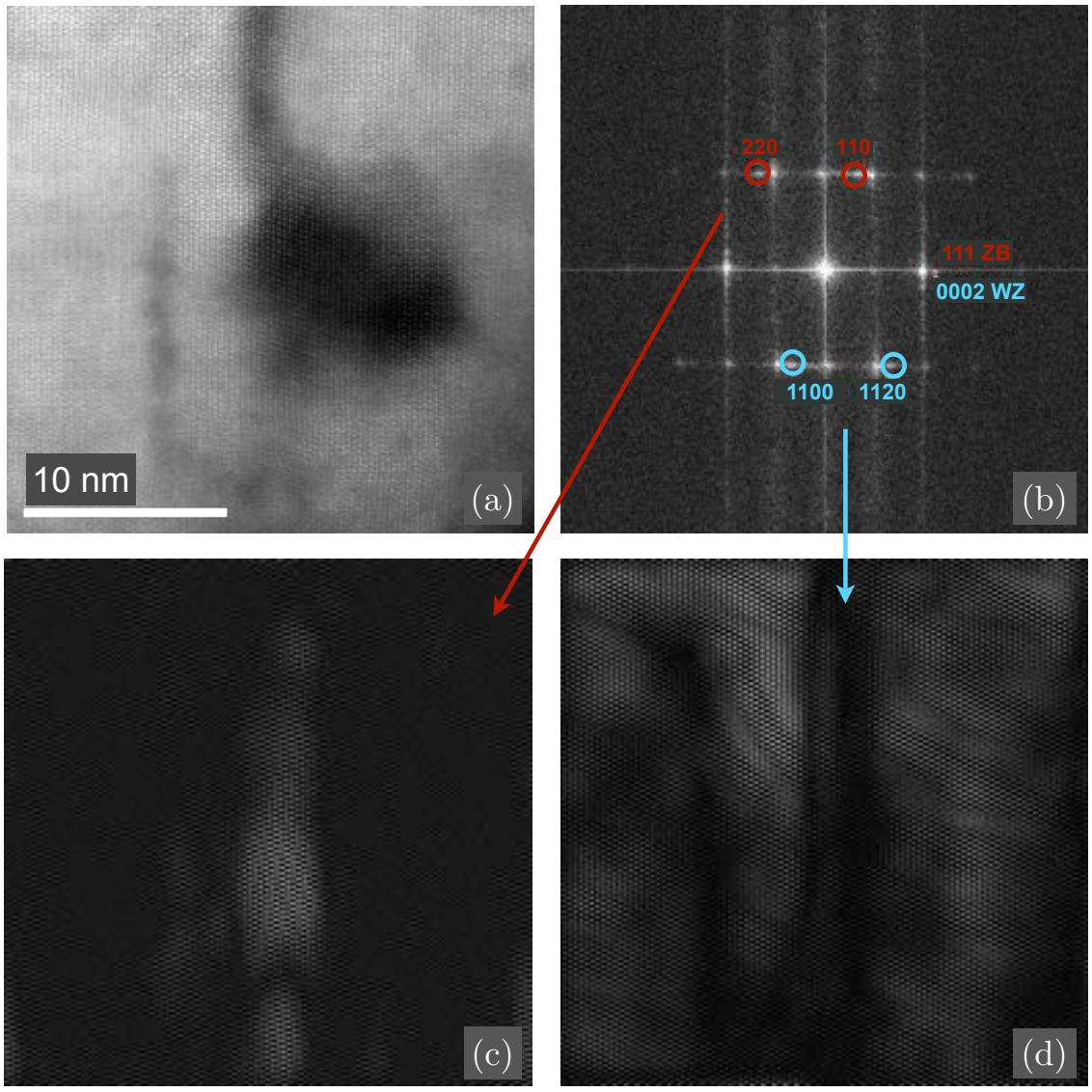

Figure 36: (a) HAADF-STEM picture of a single cluster in a 1000 nm thick BGaN layer containing 1.7% of boron (the thin foil was prepared along the $< 1120 >$ zone axis), (b) diffraction pattern of the image. Wrtzite pattern as well as zinc-blende are present, (c) inverse Fourier transform image realized with the specific wrtzite spots 1100 and 1120 and (d) inverse Fourier transform picture obtained with the cubic 111 and 220 spots [13].

20%.

4.4 Electrical characterization of BGaN

Electrical properties of BGaN layers have been investigated by our group. Growths were performed on AlN templates, under exact same conditions and for a constant thickness of 600 nm. As AlN has a very high bandgap and is undoped, leakage is less prone to happen and it does not interfere with measurements on BGaN layer above. Four-probes Van der Pauw and Hall measurements were performed at room temperature on layers of different boron composition from 0 to 1.75%.

Resistivity measured as function of boron incorporation is displayed in Fig. 37 where a very substantial increase is observed from $2.7 \times 10^{-2}\,\Omega$.cm to $7.4 \times 10^{4}\,\Omega$.cm. This statement is supported by a drastic decrease of the carrier density in the volume of the layer with boron incorporation, as shown in the inset. In addition, we can derive the mobility from Hall measurements (see inset), which exhibits an enhancement. It therefore proves that the resistivity is not due to a degradation of the structural quality that would hinder carriers movement within the crystal.

Possible explanations for this phenomenon is a compensation, or more probably a passivation, of dopants. Oxygen and Silicon are well known shallow donors and Carbon, a shallow acceptor in GaN [53, 80, 81, 82]. Hence, boron is believed to hinder trapping of these donors during growth or to compensate them. In conclusion, it was established that BGaN layers can be very resistive only with a few percents of boron, which could be very interesting for devices such as HEMTs.

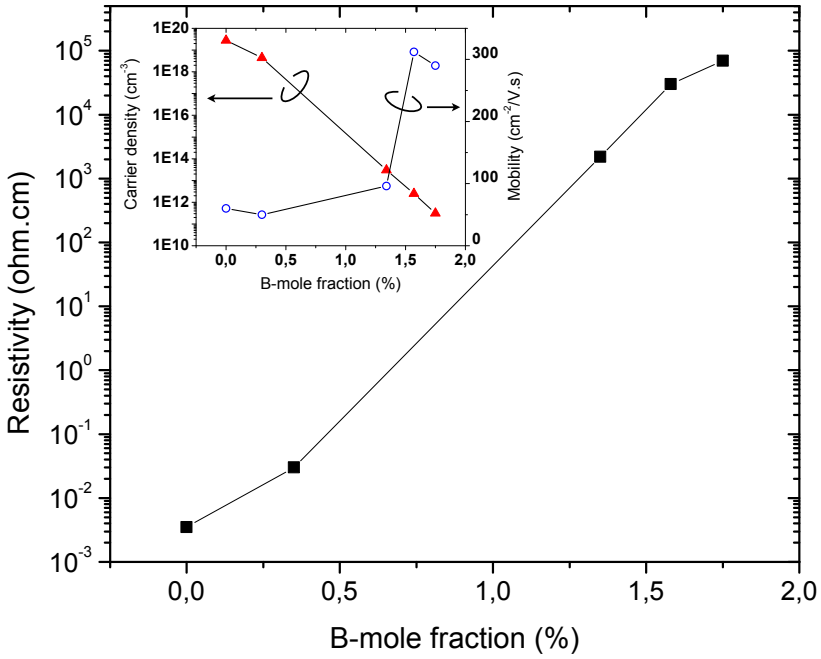

Figure 37: Electrical characterization of 600 nm thick BGaN layers on AlN template: resistivity as function of the boron composition. The inset shows the measured density of carriers and the mobility as function of the boron composition [14].

CHAPTER V

SIMULATION OF HEMT DEVICES AND DUAL-PURPOSE BGAN HEMT

If we look at the cost of the fabrication of a device, we have to take into account the price of the substrate, the maintenance of the growth machine and characterization tools with the man-hours associated, as well as all the process in clean rooms for the contacting and measurements. It is therefore judicious to perform a theoretical study beforehand to identify the most favorable structure to grow. Apart from providing a deeper understanding of physical phenomenon involved, It allows to predict performance and hence accelerates the design process.

Thus, a reasonable criterion for comparing the relative performance of HEMT structures is the study of the band diagram. Some specific figures of merit indeed allow one to find the optimal structure in terms of electronic performance. For HEMT, the main parameters to assess the capabilities of the device are the 2DEG density and the mobility of electrons. However, there are many others that are very valuable depending on the type of applications targeted: pinch-off voltage, sheet resistance, power density, cut-off frequency, power-added efficiency (P.A.E.), etc. Most of them are measurable after the actual fabrication and process of the device.

5.1 The Schrödinger-Poisson equation and ab initio calculations

In the case of semiconductor structures, where the physics involved is intimately related to quantum theory, designing starts with band engineering. Original structures based on carefully chosen alloys and thicknesses can improve performance as described later (for instance, see Section 5.3). In the scope of this research, we therefore need

a powerful tool allowing rapid prototyping of structures.

In HEMTs, the core element is the 2DEG that is caused by a bending of the conduction band at the interface of two materials of different bandgap. This phenomenon is jointly described by classical electromagnetism and quantum theory. Regarding electrostatic principles, Poisson's equation explains effects such as band bendings or potential wells attracting electrons. However, when the order of magnitude is of a few nanometers, all peculiarities specific to subatomic scales are part of the quantum theory, best described by Schrödinger's equation. That latter is crucial to describe the discretization of energy levels that occurs at the interface where the quantum well lies (the density of carriers can be dramatically changed compared to simply applying Fermi-Dirac distribution on a continuum of energies). As a consequence, estimating a complex heterostructure means solving numerically a multi-physics problem in a semi-classical approach through the Schrödinger-Poisson equations. This set of equations allows to calculate the band diagram, hence providing information on the carriers in the 2DEG, their density as well as their relative confinement.

In addition, as our structure are basically a stack of layers, it can be considered as a 1-dimensional system. We therefore focus our simulations only in one dimension, i.e. the growth axis.

5.1.1 Solving Schrödinger's equation

In one dimension, with an electrostatic potential, the Schrödinger equation is

$$-\frac{\hbar^2}{2}\frac{d}{dx}\left(\frac{1}{m^*(x)}\frac{d}{dx}\right)\psi + V(x)\psi = E\psi, \tag{22}$$

with

ψ the wavefunction of an electron (part that does not depend on time),

E the energy of the electron,

V the potential energy encountered by the electron,

h Planck's constant (with $\hbar = \frac{h}{2\pi}$),

m^* the effective mass of the electron, and

x the spatial linear coordinate.

Knowing the structure to be simulated, we first approximate the initial potential V by setting its value equal to the bandgap of the corresponding material in each section. Then, as $V(x)$ and $m^*(x)$[1] are initially known *empirically* for initialization, we solve the system to find E and ψ. Using the finite difference method (or FDM) [83] on an one-dimensional equally spaced grid with α being the mesh size, we define

$$A_{ij} = \begin{cases} \frac{-\hbar^2}{2}\left(\frac{2}{m^*_{i+1/2}}\frac{1}{\alpha_i(\alpha_i+\alpha_{i+1})}\right) & \text{if} \quad j = i+1, \\ \frac{-\hbar^2}{2}\left(\frac{2}{m^*_{i-1/2}}\frac{1}{\alpha_{i-1}(\alpha_i+\alpha_{i-1})}\right) & \text{if} \quad j = i-1, \\ -A_{ii+1} - A_{ii-1} + V_i & \text{if} \quad i = j, \\ 0 & \text{elsewhere.} \end{cases} \tag{23}$$

The major hypothesis here is to consider that physical parameters are constant over a carefully chosen finite length. This allows Eq. (22) to be rewritten in terms of matrices as

$$A\psi = E\psi. \tag{24}$$

Here, A corresponds the Hamiltonian operator related to the energy of the system which encloses both kinetic and potential energies and is known as:

$$-\frac{\hbar^2}{2\,m^*(x)}\frac{\partial^2}{\partial x^2} + V(x) \tag{25}$$

Since the mesh size is uniform, Eq. (24) is equivalent to an eigenvalue problem, and the matrix associated with the Hamiltonian (A) is a tridiagonal matrix. In the case

[1]The effective mass, m^*, being determined by the potential

of a quantum well, we get discrete values of the allowed energies. Among all the energies found, only those below the maximum energy level of the quantum well (i.e. the Fermi level E_F) are kept. They correspond to *bound states* and there are a total of s energy levels. Those correspond to the bounded states (called E_ℓ). In addition, considering the reciprocal space of allowed wavevectors, or *k-space*, for the case of a 2-dimensional system, the density of states is found as follows:

$$g_{2D}(E) = \frac{m^*}{\pi\hbar^2}. \tag{26}$$

We can therefore infer the electron charge concentration for each state by applying Fermi-Dirac statistics as follows:

$$n_\ell = \frac{m^*}{\pi\hbar^2} \int_{E_\ell}^{\infty} \frac{1}{1 + e^{(E-E_F)/kT}}\, dE, \tag{27}$$

where k is Boltzmann's constant and T is the absolute temperature. It then gives

$$n_\ell = \frac{m^* kT}{\pi\hbar^2} \ln\left(1 + e^{(E_F-E_\ell)/kT}\right). \tag{28}$$

Finally, the electron density is the sum of the concentrations of all the states weighted with the corresponding probability density as follows:

$$n(x) = \sum_{\ell=1}^{s} \psi_\ell^*\, \psi_\ell\, n_\ell = \sum_{\ell=1}^{s} |\psi_\ell|^2 \frac{m^* kT}{\pi\hbar^2} \ln(1 + e^{(E_F-E_\ell)/kT}). \tag{29}$$

Assuming that the electron density and the doping concentration N_D are known, we can solve the Poisson's equation in one dimension as

$$\frac{d}{dx}\left(\varepsilon_s(x)\frac{d}{dx}\right)\phi(x) = \frac{-q[N_D(x) - n(x)]}{\varepsilon_0}. \tag{30}$$

It gives the electrostatic potential ϕ, which is related to the potential energy V through

$$V(x) = -q\phi(x) + \Delta E_c(x), \tag{31}$$

where q is the elementary charge. We now reinject V into Eq. (22), and make the result converge toward a solution potential until a chosen precision is reached (for instance, a difference of 10^{-5} eV between two iterations).

5.1.2 Solving Poisson's equation

After solving Schrödinger's equation, we obtain the electron density $n(x)$ that is supposed to also satisfy Poisson's equation. However, Poisson's equation becomes nonlinear and solving it requires optimization technique. Newton-Raphson's method is a well-know iterative method to solve the nonlinear Poisson equation. It is used to get the error to be added to the initial potential so as to get closer to the exact solution. The goal is to determine the potential that influences the electron density. Considering the electron density as a functional of the potential $n[\phi]$, one can rewrite Poisson's equation as follows:

$$\frac{d}{dx}\left(\varepsilon_s(x)\frac{d\phi}{dx}\right) = \frac{-q[N_D - n[\phi]]}{\varepsilon_0}. \tag{32}$$

Using notations from [83], let us call $\phi^{(0)}$ the exact solution of Poisson's equation and $\delta\phi$ the error associated with the initial potential ϕ as

$$\phi^{(0)}(x) = \phi(x) + \delta\phi(x). \tag{33}$$

If we inject this expression into Eq. (32), we have

$$\frac{d}{dx}\left(\varepsilon_s(x)\frac{d\phi}{dx}\right) = \frac{-q(N_D - n[\phi + \delta\phi])}{\varepsilon_0} - \frac{d}{dx}\left(\varepsilon_s(x)\frac{d\delta\phi}{dx}\right). \tag{34}$$

Considering a first order approximation of the functionnal $n[\phi + \delta\phi] = n[\phi] + \delta n[\phi]$, one gets

$$-\left[\frac{d}{dx}\left(\varepsilon_s(x)\frac{d\phi}{dx}\right) + \frac{-q(N_D - n[\phi])}{\varepsilon_0}\right] = \frac{d}{dx}\left(\varepsilon_s(x)\frac{d\delta\phi}{dx}\right) - \frac{q}{\varepsilon_0}\delta n[\phi]. \tag{35}$$

Most of the difficulty now lies in finding an expression for $\delta n[\phi]$. Empirically, we have

$$\delta n[\phi] = \sum_{\ell=1}^{s} \left[\delta(\psi_\ell^*\,\psi_\ell)\, n_\ell + \psi_\ell^*\,\psi_\ell\,\delta n_\ell\right], \tag{36}$$

with

$$\delta(\psi_\ell^*\,\psi_\ell) = \psi_\ell^*[\phi + \delta\phi]\psi_\ell[\phi + \delta\phi] - \psi_\ell^*[\phi]\,\psi_\ell[\phi]. \tag{37}$$

According to the experimental work reported in [83], the first term of Eq. 36, in the sum of $\delta n[\phi]$, is lower by a few orders magnitude in comparison with the second term. It can be therefore neglected, which gives

$$\delta n[\phi] \simeq \sum_{\ell=1}^{s} \psi_\ell^* \, \psi_\ell \, \delta n_\ell. \tag{38}$$

We can derive an expression for δn_ℓ as follows:

$$\delta n_\ell = \frac{dn_\ell}{dE_\ell} \delta E_\ell = \frac{dn_\ell}{dE_\ell} (E_\ell(\phi + \delta\phi) - E_\ell(\phi)), \tag{39}$$

where E_ℓ's are the eigenvalues of the Hamiltonian in Schrödinger's equation. Their dependence with ϕ is therefore linked to the evolution of the Hamiltonian. Consequently, solving such a problem requires the use of perturbation theory. If we note H_0 the initial Hamiltonian, for which energy levels and eigenstates are already known, the perturbed Hamiltonian becomes $H = H_0 - q\delta\phi$, and, according to perturbation theory [84], we write

$$E_\ell(\phi + \delta\phi) = E_\ell(\phi) + \langle \psi_\ell | - q\delta\phi | \psi_\ell \rangle, \tag{40}$$

where we used the *bra-ket* notation. Moreover, using the expression of n_ℓ with Eq. (28), we have

$$\frac{dn_\ell}{dE_\ell} = \frac{d}{dE_\ell} \left(\frac{m^* kT}{\pi\hbar^2} \ln(1 + e^{(E_F - E_\ell)/kT}) \right) = -\frac{m^*}{\pi\hbar^2} \frac{1}{1 + e^{(E_\ell - E_F)/kT}}. \tag{41}$$

So, if we inject this formula in Eq. (39), we obtain

$$\delta n_\ell = \frac{m^*}{\pi\hbar^2} \frac{1}{1 + e^{(E_\ell - E_F)/kT}} \times \langle \psi_\ell | - q\delta\phi | \psi_\ell \rangle, \tag{42}$$

and, eventually, Eq. (38) becomes

$$\delta n[\phi] \simeq \sum_{\ell=1}^{s} \psi_\ell^* \, \psi_\ell \, \delta n_\ell = \sum_{\ell=1}^{s} \psi_\ell^* \, \psi_\ell \times \frac{m^*}{\pi\hbar^2} \frac{1}{1 + e^{(E_\ell - E_F)/kT}} \times \langle \psi_\ell | - q\delta\phi | \psi_\ell \rangle. \tag{43}$$

Finally, Eq. (35) is rewritten as follows:

$$\begin{aligned} &- \left[\frac{d}{dx} \left(\varepsilon_s(x) \frac{d\phi}{dx} \right) + \frac{-q(N_D - n[\phi])}{\varepsilon_0} \right] = \\ &\quad \frac{d}{dx} \left(\varepsilon_s(x) \frac{d\phi}{dx} \right) - \frac{qm^*}{\varepsilon_0 \pi\hbar^2} \sum_{\ell=1}^{s} \psi_\ell^* \psi_\ell \times \frac{m^*}{\pi\hbar^2} \frac{1}{1 + e^{(E_\ell - E_F)/kT}} \times \langle \psi_\ell | - q\delta\phi | \psi_\ell \rangle. \end{aligned} \tag{44}$$

This differential equation gives the incremental error $\delta\phi$ to be added to the potential at each iteration to converge to the exact solution. Let us also approximate the value of $\langle\psi_\ell|q\delta\phi|\psi_\ell\rangle$, which represents an integral in this case, by $q\delta\phi$ as a first order approximation [85]. Using again the FDM with a mesh size β, we introduce the matrices C and $\hat{C}$ defined by

$$C_{ij} = \begin{cases} \frac{2\varepsilon_{i+1/2}}{\beta_i(\beta_i+\beta_{i-1})} & \text{if} \quad j = i+1, \\ \frac{2\varepsilon_{i-1/2}}{\beta_{i-1}(\beta_i+\beta_{i-1})} & \text{if} \quad j = i-1, \\ -C_{ii+1} - C_{ii-1} & \text{if} \quad i = j, \\ 0 & \text{elsewhere,} \end{cases} \tag{45}$$

$$\hat{C}_{ij} = \begin{cases} \frac{2\varepsilon_{i+1/2}}{\beta_i(\beta_i+\beta_{i-1})} & \text{if} \quad j = i+1, \\ \frac{2\varepsilon_{i-1/2}}{\beta_{i-1}(\beta_i+\beta_{i-1})} & \text{if} \quad j = i-1, \\ -\hat{C}_{ii+1} - \hat{C}_{ii-1} + U_i & \text{if} \quad i = j, \\ 0 & \text{elsewhere,} \end{cases} \tag{46}$$

with

$$U_i = \frac{q^2 m^*}{\varepsilon_0 \pi \hbar^2} \sum_{\ell=1}^{s} \psi_\ell^{(i)*} \psi_\ell^{(i)} \times \frac{1}{1 + e^{(E_F - E_\ell^{(i)})/kT}}. \tag{47}$$

It should be noted that $\psi_\ell^{(i)}$ corresponds to the ℓ^{th} wavefunction associated with the energy E_ℓ taken at the discrete position i. Let us also define the vectors $\{b\}_i = q(N_D^{(i)} - n^{(i)})/\varepsilon_0$ as well as the electrostatic potential, $\{\phi\}_i$, and the error vector, $\delta\phi_i$, both along the x-axis (the index i being the position). Eventually, the differential equation described in Eq. (44) is expressed as

$$-([C]\{\phi\} + \{b\}) = \hat{C}\{\delta\phi\} \quad \Rightarrow \quad \{\delta\phi\} = -[\hat{C}]^{-1}([C]\{\phi\} + \{b\}). \tag{48}$$

Thus, considering the initial potential ϕ found with Eq. (24), we compute the error $\delta\phi$ and approximate the exact solution $\phi^{(0)}$ using Eq. (33). Therefore, solving self-consistently Schrödinger's and Poisson's equation consists in injecting the obtained electrostatic potential $\phi^{(0)}$ back into Eq. (22), and iterate the process until it converges (as explained below).

5.1.3 The Schrödinger-Poisson *solver*

As detailed earlier, the Schrödinger-Poisson system is formed of two coupled equations that have to be solved simultaneously. We therefore solve them self-consistently until convergence. The diagram in Fig. 38 shows the iterative algorithm used to self-consistently solve the system. This allows us to obtain the band diagram and information on the carrier concentration as well as their spatial distribution.

The initial potential (V) is known *a priori*, i.e. using an estimation of its shape based on bandgaps, as it is the most basic approximation accessible in the first place. Consequently, this initial potential exhibits several abrupt discontinuities that are to be smoothed down with calculations. It is then injected into Schrödinger's equation so as to get the eigenvalues. Only the *bounded* states, associated to energies supposed to be below the Fermi level, are considered since energies beyond correspond to *virtually bonded* states. Additionally, normalization is performed on each bounded eigenvector while carefully respecting the boundary conditions to compute the electron concentration. Eventually, the solution is used into Poisson's equation, which gives a new potential. Then, if the error ε, that is the difference between the obtained potential and the previous one, is higher than a threshold value (typically 10^{-5}), the iterative process continues until the error convergence.

5.1.4 Adding polarization to Poisson's equation

For nitride semiconductors, polarization is critical to describe key phenomenon occurring in devices as nitride HEMTs, such as the spontaneous creation of a band bending enclosing a 2DEG (see Section 2.2.2). Thus, it is of paramount importance to introduce the polarization in our simulated structure. We can therefore introduce simply the polarization within Poisson's equation as follows:

$$\frac{d}{dx}\left(\varepsilon_s(x)\frac{d}{dx}\phi(x) - \frac{P(x)}{\varepsilon_0}\right) = \frac{-q[N_D(x) - n(x)]}{\varepsilon_0}\ . \tag{49}$$

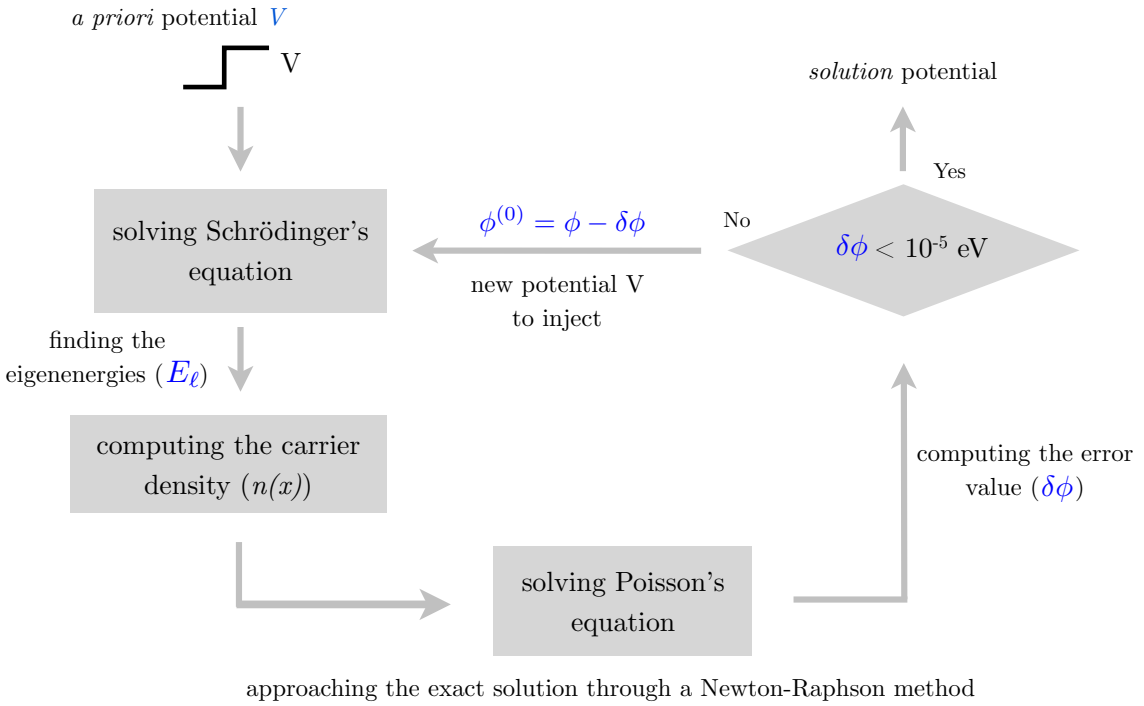

Figure 38: Iteration process for the Schrödinger-Poisson *solver*.

Following a reasoning similar to that of Section 5.1.3, the final matrix equation to be solved becomes

$$-([C]\{\phi\} + \{b\} - \{p\}) = \hat{C}\{\delta\phi\}, \tag{50}$$

where the vector p is the first derivative of the polarization vector $P(x)$. By means of the finite difference technique, the vector p can be defined as

$$p_i = 2\,\frac{p_{i+1/2} - p_{i-1/2}}{h_i + h_i + 1}. \tag{51}$$

Nevertheless, modifying directly the equation as explained above leads to computational problems. As our first approximation for the initial polarization profile is to take constant values in each different material, it leads to discontinuities at interfaces complexifying the computation. Alternatively, it is physically equivalent to add surface carrier concentrations at interfaces where polarization-induced sheet charges exist (i.e. where the polarization vector encounters discontinuities). Hence, the simulator uses physical parameters from the literature, computes the polarization for a given

Table 2: Physical constants of nitrides used for the calculation of the polarization. Parameters e_{31} and e_{33} are the piezoelectric coefficients, C_{13} and C_{33} are the elastic constants and P_{sp} is the spontaneous polarization.

	GaN	AlN	InN	BN
a (in Å)	3.210	3.112	3.533	2.534
e_{31} (in C/m^2)	-0.49	-0.60	-0.52	0.31
e_{33} (in C/m^2)	0.73	1.46	0.95	-0.94
C_{13} (in GPa)	103	108	98	61
C_{33} (in GPa)	405	373	245	1061
P_{sp} (in C/m^2)	-0.029	-0.081	-0.032	-0.032

structure using Eq. (12) and simply treats polarization charges as fixed interface charges.

5.2 Polarization study in nitrides

Polarization plays a major role in the creation of a 2DEG in a nitride-based HEMT structure. For our study of new materials, we therefore focus first on the calculation of the polarization field. To input the influence of polarization in our HEMT structures, we use the standard technique that consists in adding electrons at carefully chosen interfaces with densities given by Eqs. (12) and (13). The physical constants employed are usually given by *ab initio* calculations (cf. the method used in [42]) for binary compounds. Vegard's law, which is a linear interpolation, is then applied to obtain the ternary compounds values. In Table 2, the parameters relevant for the polarization calculation are shown for the three binaries GaN, AlN and BN.

Graphs in Fig. 39 and Fig. 40 show notably the piezoelectric polarization and the sheet charge density calculated respectively for AlGaN and InGaN strained on GaN at their respective interfaces. In the case of AlGaN, the absolute value of the sheet charge density increases steadily with the Al content. It is in accordance with the piezoelectric polarization increase as the AlGaN barrier is more strained (stretched)

on GaN (refer to Section 2.1.3). Thus, a HEMT structure with a higher Al content in the barrier should have more carriers in the 2EDG. In practice, the density reaches a threshold close to 0.5 Al-mole fraction.

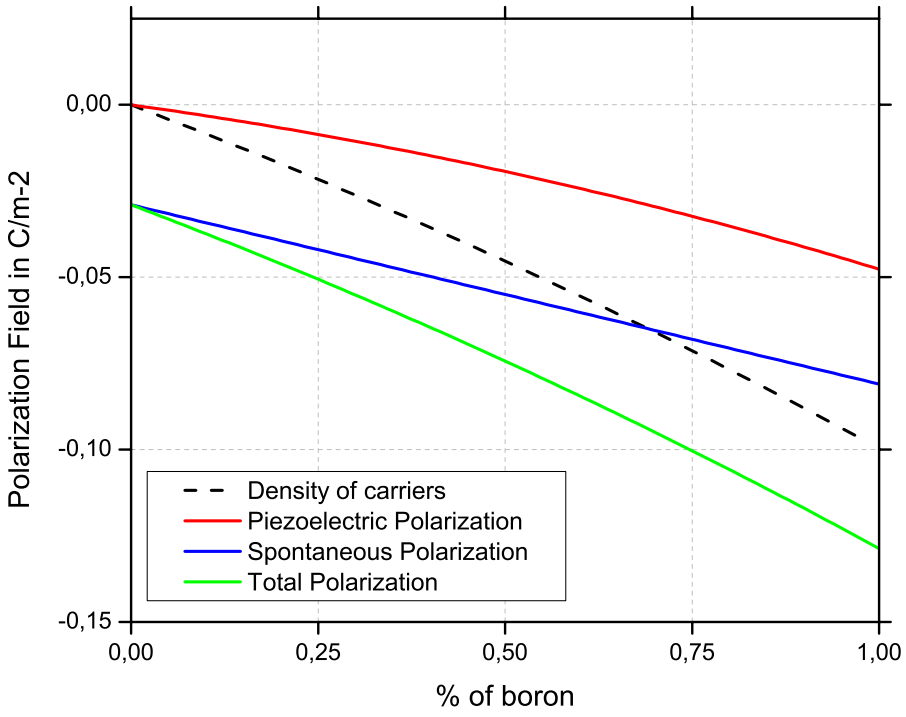

Figure 39: Polarization evolution in an AlGaN/GaN heterostructure.

For the case of InGaN, the absolute value of the sheet charge density increases as well with the In-mole fraction as the InGaN layer is more strained (compressive) on GaN. Nevertheless, the charges are positive, which implies that electrons are repelled from the interface and not trapped as in an AlGaN/GaN interface.

Ab initio results are known to provide tendencies and orders of magnitude rather than accurate values. Yet, it is known that theoretical 2DEG densities calculated with these parameters happen to be very close to experimental results [38]. Consequently, to interpolate for instance BGaN's parameters, we have to look for similar *ab initio* parameters for the binary BN.

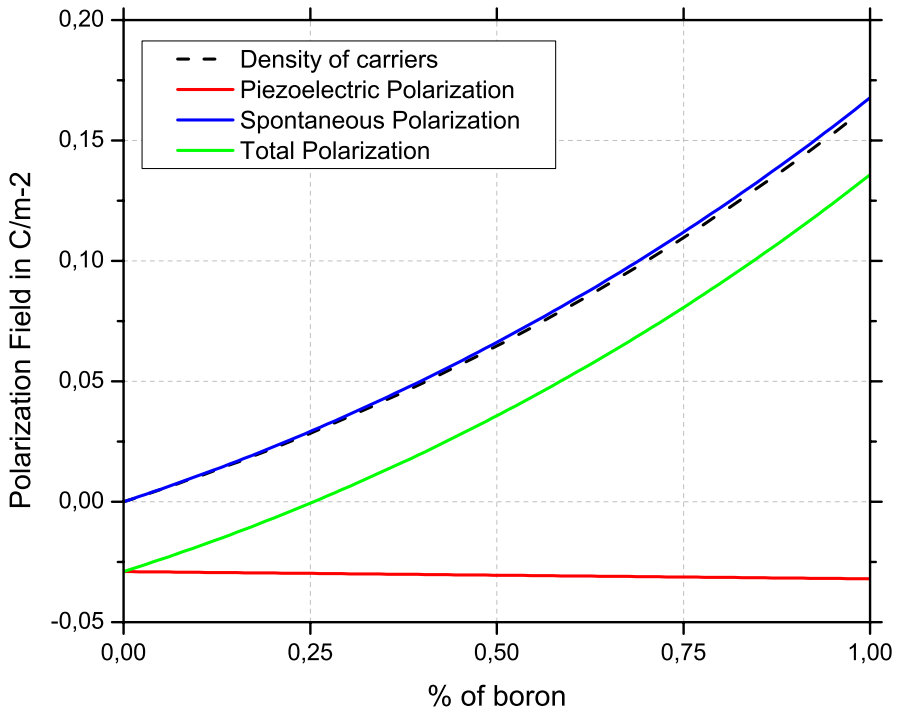

Figure 40: Polarization evolution in an InGaN/GaN heterostructure.

5.3 Simulation of AlGaN/GaN HEMT

First simulations were performed on standard AlGaN/GaN HEMTs. We used equation from the literature to make a software that computes the 2DEG density of a standard AlGaN/GaN HEMT knowing the thickness and the composition of the barrier as well as the applied gate voltage. We quickly moved to simulations performed with Snider's software as it was a stand-alone, easy-to-use, program that could be adapted to our needs.

We performed simulation of standard AlGaN/GaN HEMTs to evaluate accuracy of the solver. In Fig. 41, we display results of simulation of an AlGaN barrier with a composition of 0.25 for Al. Different thicknesses of the barrier and doping level were employed and data are compared to values reported in an article from Ambacher *et. al.* [38]. Simulation were performed considering a Nickel layer for the gate metal but no applied voltage ($V_{gs} = 0$). First observations show that the carrier density in the

2DEG increases with the Al composition in the barrier. It is in accordance with the sheet charge density increase (in absolute value) observed with the polarization effect (refer to Fig. 39). Moreover, results are in good accordance with experimental results from literature.

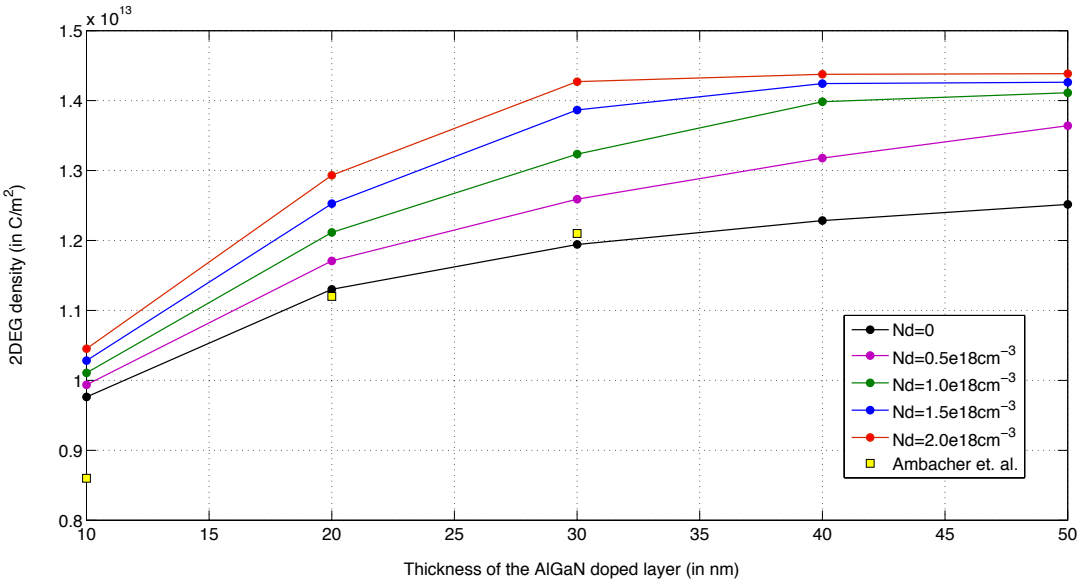

Figure 41: Simulation of an $Al_{0.25}GaN_{0.75}$/GaN structure, with 0.25 of Al in barrier, for different thicknesses doping level of the barrier.

To further evaluate the accuracy of the simulator, we performed simulations on AlGaN/GaN HEMT structure comprising an InGaN back-barrier with the Schrödinger-Poisson *solver*. The InGaN back-barrier improves the confinement of the 2DEG by raising the conduction band and preventing leakage in the buffer (we will discuss it in more details in the following Section 5.4.1). Simulated structures consist of a 15 nm $Al_xGa_{1-x}N$ barrier layer with $x = 0.22$, a 1.5 nm thin AlN interlayer, a 5 nm GaN channel layer, followed by an InGaN back-barrier on top of the GaN buffer. Figure 42 shows density profiles obtained for different thicknesses (either 10 or 20 Å) and In-mole fraction (5 to 15%) of the InGaN back-barrier. The density profile of the same structure, but with no back-barrier, is plotted (in black). For all structures, a sharp drop of the carrier density is observed beyond the InGaN layer with densities two

orders of magnitude lesser than in a standard structure. Carriers are indeed repelled by the electrostatic barrier created by the InGaN/GaN interface. Therefore, few carriers happen to be far from interface channel/barrier and the leakage phenomenon is less likely to occur. This results are in good accordance with ones reported in the literature [86, 87].

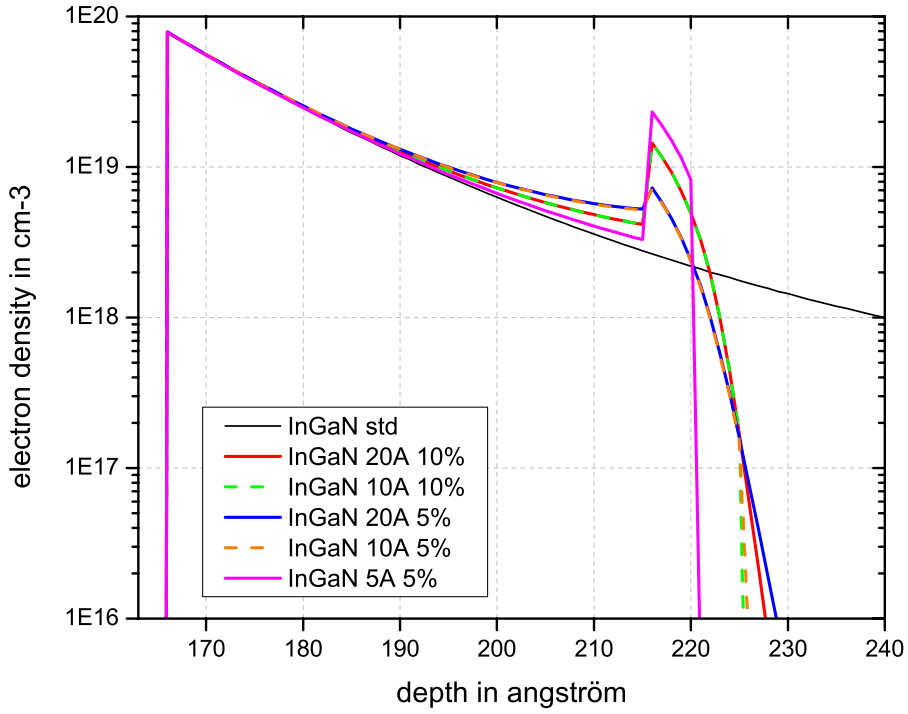

Figure 42: Simulation of the confinement of an AlGaN/AlN/GaN/InGaN/GaN HEMT structures with different InGaN back-barriers - the maximum of the density profiles corresponds to the AlN/GaN interface (based on [15]).

To know better the impact of back-barriers on the spread of carriers, we performed further simulations on additional structures displayed in Figs. 43. The HEMT structure remains the same, but composition and thickness are modified. Again, even though the peak concentration at the interface barrier/channel remains unchanged, the spread of the carriers changes dramatically with the introduction of back-barriers as seen in Fig. 42. Furthermore, it can be observed that the In-mole fraction has little influence on the shape on the profile.

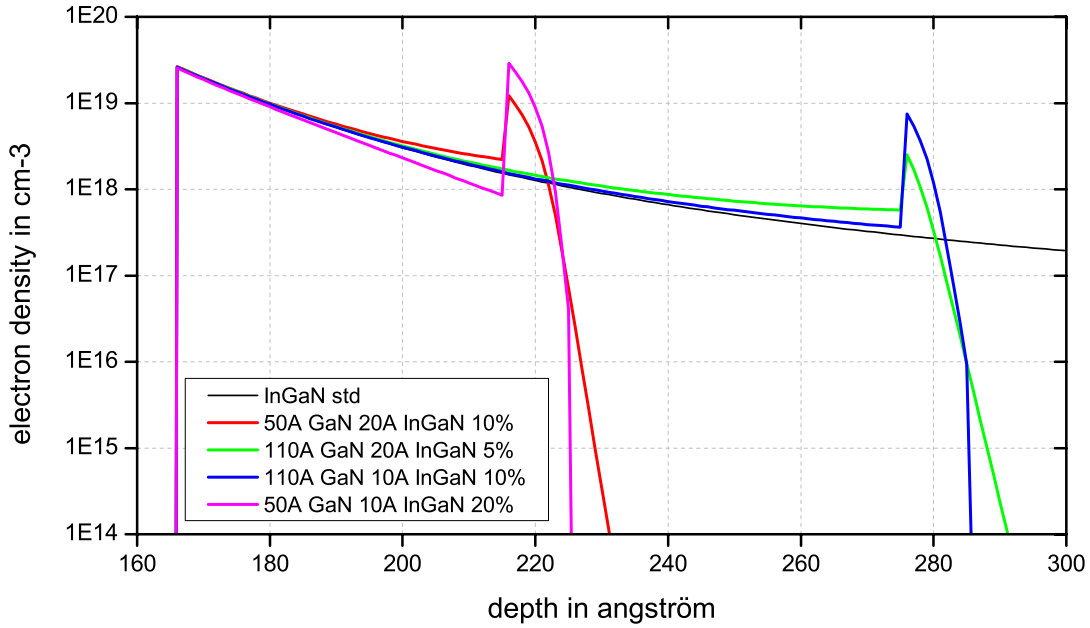

Figure 43: Simulation of the confinement of an AlGaN/AlN/GaN/InGaN/GaN HEMT structures with different InGaN back-barriers - the maximum of the density profiles corresponds to the AlN/GaN interface (based on [15]).

To assess the confinement, the limit depths, before which 90% or 99% of the electrons are plotted in Fig. 44. For comparison purpose, horizontal lines representing values for a standard structure with no InGaN are added. The distance between the two limits is always below 50 Å with the introduction of a back-barrier and 99% of the electrons remain below 300 Å whereas this limit is around 500 Å for a standard structure. It can be noticed that the confinement is logically better when the barrier is closer to the interface channel/barrier as electrons 'bounce back' to the 2DEG earlier. Besides, the thickness of the barrier does not seem to impact results between 10 or 20 Å. Similarly, no significant improvement is observed by increasing the composition of the InGaN back-barrier. It can therefore be kept low, down to 10 %, to obtain satisfying confinement results.

Subsequently, we can imagine using an analogous design but with a different material. We will show that BGaN can be employed for the same purpose while

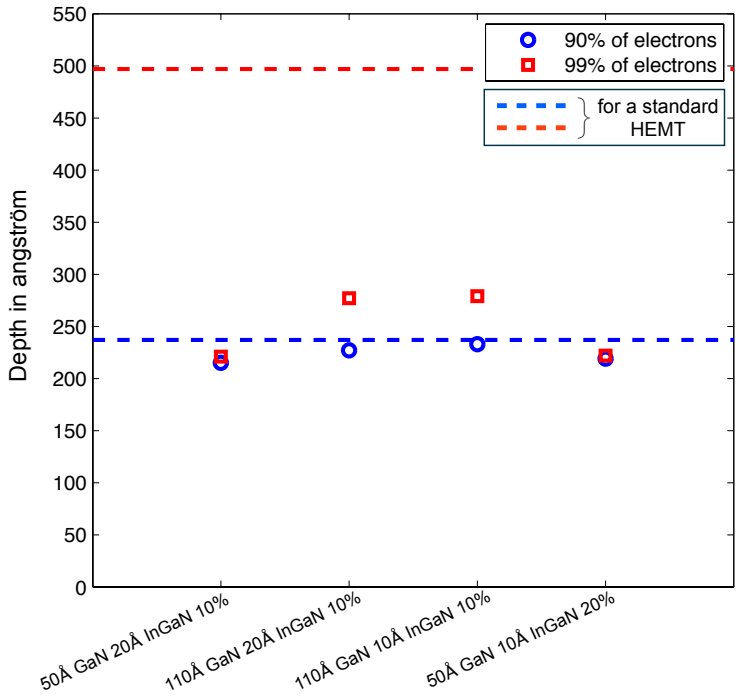

Figure 44: Simulation of the confinement of AlGaN/GaN HEMT structures with different InGaN back-barriers - depth limits for 90% or 99% of the electrons.

keeping limited thicknesses and low boron incorporation.

5.4 AlGaN/GaN HEMT with BGaN thin layers

5.4.1 Limiting leakage in the buffer

Several limitations are caused by the insufficient confinement of the electrons in the 2DEG, which is crucial for the overall efficiency of the HEMT. Measurements on devices have proven that a poor confinement leads to ill-defined pinch-offs and a reduced modulation efficiency because of the presence of numerous traps.

In conventional AlGaN/GaN HEMTs, GaN is not only the buffer, but also includes the electron carrier channel located close to the interface. The intrinsic drawback is that, even though electrons cannot spillover in the barrier, they do not encounter any potential barrier at the backside of the 2DEG, hence resulting in buffer leakage. Additionally, the unintentional background doping in GaN is high as seen earlier,

and participates in the leakage phenomenon [53]. To overcome this, researchers first have tried to compensate it with impurities such as iron (Fe) or carbon (C). These dopants are incorporated during the epitaxy to get semi-insulating buffers [88, 89]. Nonetheless, these techniques introduce deep-levels defects in the GaN layer resulting in memory effect and current collapse with high drain voltage.

Another idea is to employ a buffer of greater bandgap such as an AlN buffer. However, the lattice mismatch between the AlN and the buffer of GaN is tremendous. Certain studies used a graded AlGaN layer on top of the AlN buffer to attenuate this mismatch, but it leads to mixed results [90]. Despite an enhanced breakdown voltage, the mobility is significantly impaired as it strongly depends on the crystalline quality of the GaN channel [91]. AlGaN can also be employed in the buffer as an electrostatic barrier (or back-barrier, see example of InGaN below), we then talk about a double-heterostructure HEMT (DH-HEMT) AlGaN/GaN/AlGaN [92, 93, 94, 95]. Yet, it originates in too many threading dislocations impeding the structural quality of the GaN channel and the capacities of the 2DEG.

We can also find AlGaN/InGaN/GaN structures where a thin layer of InGaN is used as the channel [29, 96]. It is interesting to use InGaN as it dips the band conduction down, and hence increases the confinement and the density of carriers. The main issues are a low breakdown voltage and a higher alloy scattering impeding the mobility, which are mainly due to the interface roughness [97].

Recently, it has been demonstrated that using an InGaN electrostatic barrier to electrons in the GaN buffer better confines these carriers in the quantum-well formed at the interface, hence preventing leakage in the bulk [98, 99, 100, 101]. State-of-the art record frequencies were achieved with a f_{max} up to 230 GHz. To obtain such a result, an InGaN thin layer (10% of In, 10 nm thick) is used as a back-barrier in a conventional AlGaN/GaN HEMT structure. Even though InGaN has a lower bandgap than GaN, it raises the conduction band because of stronger polarization

effects occurring in nitride materials (see Fig. 45).

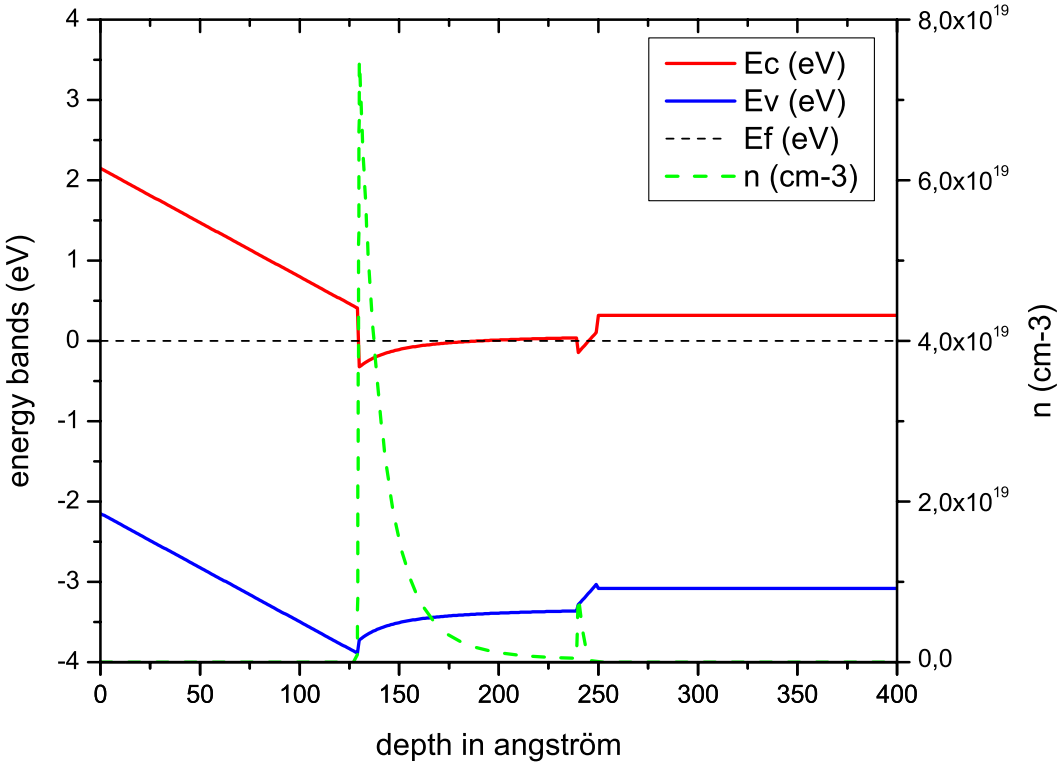

Figure 45: Simulation of an AlGaN/GaN HEMT with an InGaN back-barrier.

Indeed, indium has the peculiarity to have a lattice parameter larger than GaN. Therefore, InGaN alloys experience a compressive strain when they adopt the GaN lattice parameter (see Section 2.1.3). As illustrated by Eq. (13), describing the axial-strain induced polarization, the strain experienced in the bilayer system is reversed. It is caused by the lattice parameter of InGaN, which is smaller than that of GaN. The polarization vector then points in the opposite direction. If we refer to Fig. 40, with the calculation of InGaN polarization strained on GaN, the distinctive difference compared to AlGaN is the density of charges that is positive. Compared to the use of an AlN spacer layer, the InGaN thin layer creates a discontinuity of the conduction band downwards, which attracts electrons and is compensated on the other side by a lift of the conduction band.

As mentioned above, our aim now is to prove that thin BGaN layers could help at limiting effectively the leakage in the buffer. To assess this by simulation, we need to make use of the right data and equations allowing the introduction of BGaN in our designs.

5.4.2 Implementing BGaN

The binary BN exists in different polytypes, and its growth remains challenging as researchers address several obstacles (see Section 4.1). The boron nitride compounds considered in this study, in which boron incorporation is low (not more than a few percents, see 4.1), are grown in a wurtzite structure (the atom of boron using the Ga-site for the case of BGaN). Consequently, most properties of BGaN are quite similar to the pure binary GaN except for the resistivity and bandgap bowing, both showing interesting characteristics even with very little boron incorporated in the alloy [10, 14].

In our simulations, we have to implement each binary material (i.e. GaN, AlN, InN, etc.) with all relevant parameters needed for both Schrödinger's and Poisson's equations. When a ternary material is employed, its parameters are linearly interpolated from the two binaries it originates from. Thus, we need to implement BN in our database to simulate layers with boron (e.g. BGaN, BAlN, etc.). For most parameters, as very little boron is incorporated, we reuse those of GaN for BGaN. However, it will not be the case with the bandgap, a crucial parameter, which is notably influenced by boron incorporation. The quadratic equation of the bandgap for a BGaN layer, including the bowing found by our group [10], is as follows:

$$E_g = 3.39 - 7.09\,x + 9.2\,x^2 \quad \text{eV}, \tag{52}$$

with $x \in [0, 1]$, the rate of boron diluted. However, we consider this equation to be valid for no more than 5% of boron in BGaN. Now that the bandgap is defined, the next step is to implement the polarization, which is the other key feature to simulate

devices with boron-based materials.

5.4.3 Polarization in BGaN

For the computation of the polarization in a BGaN layer strained on a GaN bulk layer, we need the lattice parameter, the elastic constants, and the piezoelectric constants of BN (see Table 2). Usually, as calculations using *ab initio* parameters give tendencies rather than quantitative results, it is better to select a set of values from the same study, or article per say. Numerical values for the physical properties of GaN, AlN and InN are found in the literature [42, 102], and simulations made with these *ab initio* parameters have been proven to be close to experimental results [38]. Nonlinear behaviors, due to strain effects, have been demonstrated for the piezoelectric constants and for the spontaneous polarization value as a function of the composition [17, 103], but taking into account these bowings has little effect on the end results. However, the spontaneous polarization of BN is not calculated in the study by Shimada *et al.*, it can be found though in [104].

The graph obtained after computation of the polarization of BGaN strained on GaN is shown Fig. 46. The quadratic equation of the total polarization for a BGaN layer is as follows:

$$P_{pz} + P_{sp} = 3 \times 10^{-6} + 1.502 \times 10^{-5}\, x + 3.491 \times 10^{-5}\, x^2 \quad \mathrm{C/m^2}, \tag{53}$$

with $x \in [0, 1]$, the rate of boron diluted. It is interesting to see first that the polarization undergoes a change in the direction of its vector (see Fig. 46). This is due to the piezoelectric parameters of BN (see Table 2) that have inversed signs compared to the other nitrides.

Furthermore, as BN's *ab initio* parameters were primarily extracted from one single study, we decided to launch calculations with our partner from the LEM3 lab (or *Laboratoire d'étude des microstructures et de mécanique des matériaux*) at Metz, France. In Appendix B are displayed *ab initio* calculations performed on GaN,

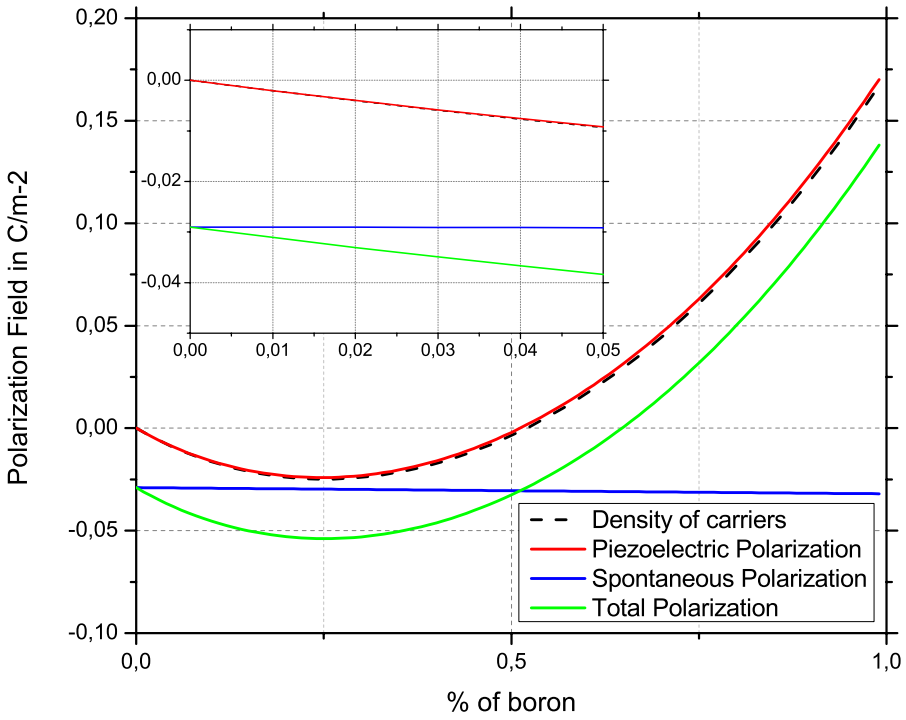

Figure 46: Polarization evolution in a BGaN/GaN heterostructure.

AlN and BN binary compounds. First, it was observed that results for the first two well-known materials agreed with data from the literature. Moreover, as parameters derived for BN fully match with results reported by Shimada *et al.*, it supports their employ for our simulations.

5.4.4 Dual-purpose BGaN layers for AlGaN HEMTs

The introduction of an InGaN notch as a barrier to electrons in AlGaN/GaN HEMTs produced state-of-the-art results, but a significant drawback lies in their growth by MOCVD; InGaN is grown at a different temperature than GaN or AlGaN (e.g. 700-800°C [105] compared to 1000°C [106], respectively). Two options are possible: either growing everything at the same temperature, but reducing the growth temperature of GaN diminishes its structural quality [107], or using different temperatures for each material, knowing that multiple temperature changes impede the interfacial quality between layers [108].

BGaN materials, similarly to InGaN, have a smaller bandgap for small boron incorporation according to a recent study exhibiting a bowing [10]. They also possess the distinctive strong polarization of nitride materials. Additionally, incorporating boron allows the temperature to be kept constant during the growth by MOCVD of AlGaN and GaN. Therefore, adopting the same band-engineering concept as in [99], it is more convenient to grow an AlGaN/GaN HEMT with a BGaN barrier layer (or back-barrier, or BB) to obtain a greater structural quality as illustrated in Fig. 47.

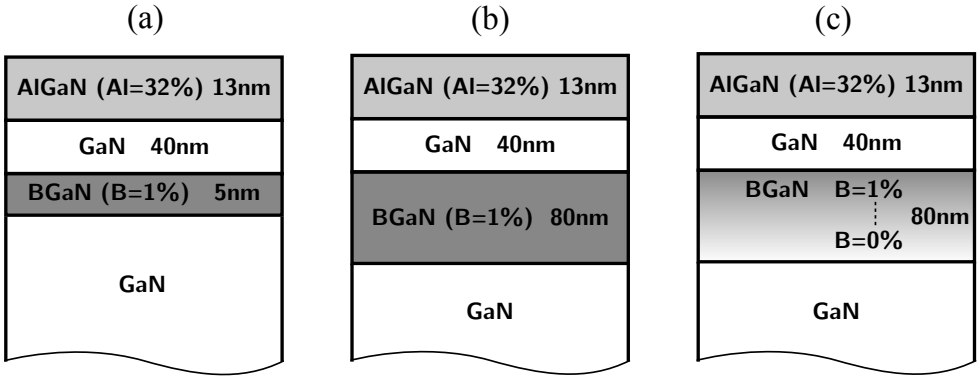

Figure 47: Examples of AlGaN/GaN HEMT with and without a BGaN BB employed for simulations: (a) thin BGaN BB, (b) thick BGaN BB and (c) graded BGaN BB.

According to Fig. 46, as the lattice of BGaN tends to be smaller with boron incorporation compared to GaN, the density of charges created is negative unlike the case of InGaN barriers. Consequently, as seen in Fig. 48, the barrier raises the conduction band locally similarly to AlGaN barriers in DH-HEMTs, but this effect is not spread over the buffer as for InGaN (see Section 5.4.1 and Fig. 45). It is possible to obtain a larger *wall* to block the electrons by either using a thicker graded or a mono-composition BGaN layer, as illustrated in Fig. 49.

Moreover, studies from our group have shown that, with boron incorporation, BGaN's resistivity and mobility are significantly enhanced, which proves that it does not originate from structural disorder [14]. Thus, a thick layer of BGaN, for an incorporation from 1 to 5%, creates an electrostatic and resistive barrier to electrons

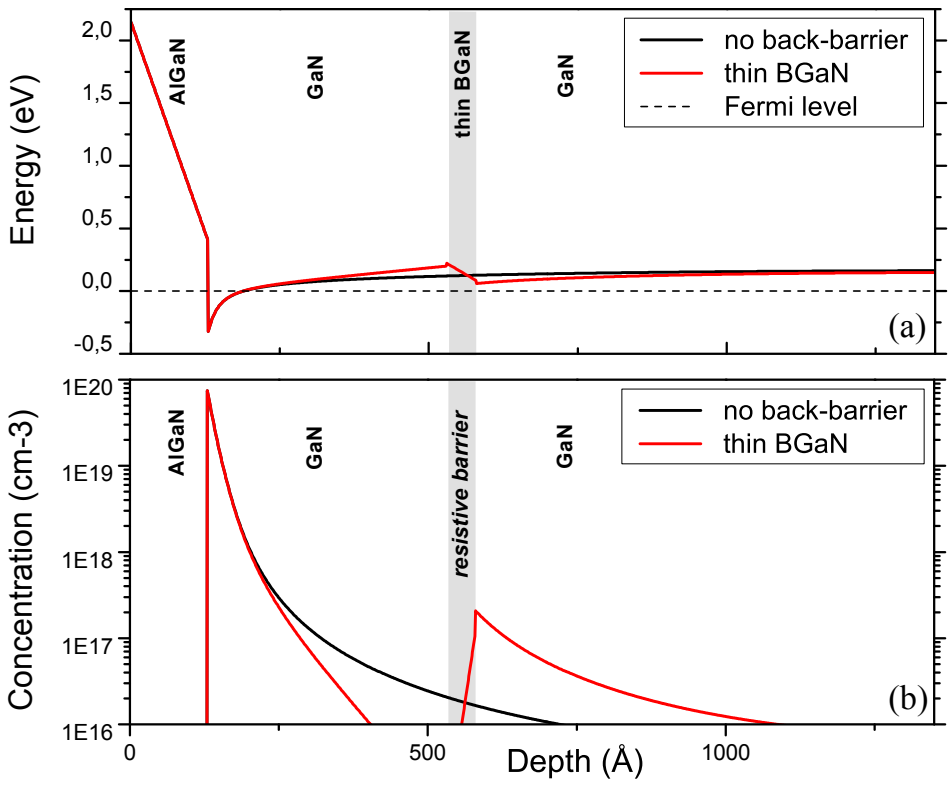

Figure 48: Conduction band profile and carriers density for AlGaN/GaN HEMTs with and without a thin BGaN BB from the top surface to the buffer. In (b), the raise of the conduction band with the BGaN BB offers an electrostatic barrier to electrons that reduces the spreading of the electrons in the 2DEG as illustrated in (a). The grey-colored area corresponds to the thin BGaN layer which also represent a resistive barrier to electrons, hence preventing leakage in the buffer.

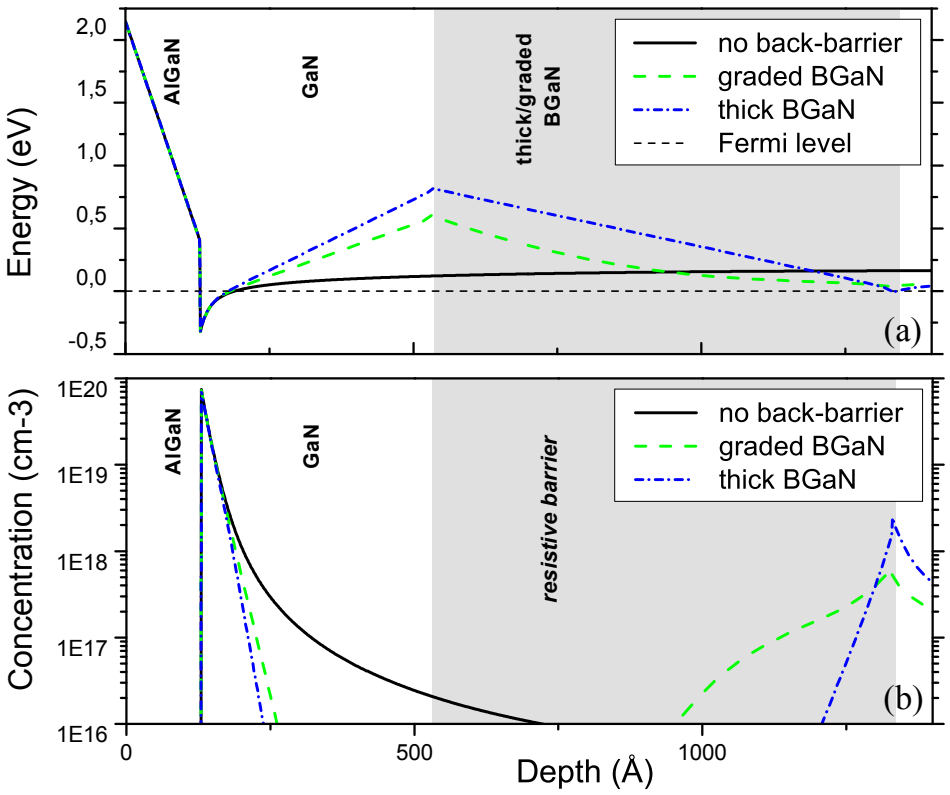

Figure 49: Conduction band profile and carriers density for AlGaN/GaN HEMTs with and without a thick or graded BGaN BB from the top surface to the buffer. In (b), raises of the conduction band with BGaN BB offer an electrostatic barrier to electrons that reduces the spreading of the electrons in the 2DEG as illustrated in (a). The grey-colored area corresponds to the thick/graded BGaN layer which also represent a resistive barrier to electrons, hence preventing leakage in the buffer.

between the channel enclosing the 2DEG and the buffer of GaN below. This dual purpose of BGaN, being more suitable for the MOCVD growth, shows that these innovative structures are very promising for high-power and high-frequency applications since an improved confinement of carriers can be expected.

CHAPTER VI

EXPERIMENTAL WORK: OPTIMIZATION OF HEMT GROWTH

Components, such as HEMTs, require growth of material with very low levels of residual impurities. Thus, for our first HEMT structure growths in our machine (refer to Section 3.1.2), our attention was firstly focused on growth quality itself. Optimization was performed on the growth chamber and on the manifold, throttle valves of that last were replaced with new ones. The T-shaped growth chamber was configured to minimize first parasitic reactions that occur in vapor phase and, secondly, deposition on inner walls. To prevent any cross contamination with boron, our growth planning was organized in campaigns, each one dedicated to a specific structure to ensure that the chamber sees the same compounds and growth conditions. To further counter any pollution, advanced outgassing is routinely performed between each campaign, consisting in a high temperature thermal annealing at low pressure. Moreover, we acquired a new molybdenum sample holder which was cleaned systematically between campaigns by sand-blasting.

By adopting these precautions, we obtain reproducible incorporations of aluminium as well as stable growth rates of AlGaN and GaN. Consequently, the reproducibility, structural quality and purity of our structures are guaranteed.

6.1 Growth of thick AlGaN layers

A major technological brick to acquire before making HEMT is to know how to grow the AlGaN barrier layer. The ternary compound AlGaN has been extensively studied by the scientific community for a wide variety of devices. It is a cardinal component

that is decisive for properties such as carrier density or confinement and light generation as demand shifted to higher power-handling capabilities and shorter wavelength sources [3]. As seen in Section 2.1.2, apart from MBE, MOVPE is the second major techniques to achieve AlGaN layers. Nonetheless, its growth by MOVPE requires a specific optimization proper to a given machine. Precise control of the thickness and composition is not straightforward particularly because of the high reactivity of the III-group element precursor trimethylaluminium (TMAl) with V-group element nitrogen (ammonia, NH_3, being the precursor) producing by-products. It has been shown that these parasitic interactions were more critical for Al. The two compounds TMAl and NH_3 react as soon as they are put together in the chamber through a bimolecular process leading to a polymer. As a consequence, the growth rate of AlGaN can diminish significantly along with the aluminium incorporation efficiency if proper growth conditions are not chosen [109]. The aluminium incorporation efficiency ν is given as follows:

$$\nu = \frac{x}{TMAl/(TMAl + TMGa)},$$

where x is the mole fraction in solid phase ($Al_xGa_{1-x}N$) and TMAl/(TMAl + TMGa) representing the Al precursor proportion within the total III-group elements' precursors which is TMAl + TMGa in the gaseous phase. The *V/III ratio* corresponds to the ratio of the concentration of the nitrogen source to the total concentration of the III-elements (Ga, Al, In...) sources supplied to the growth chamber. It is precisely the parameter that is varied to limit parasitic reaction during growth.

Figure 50(a) exhibits efficiency results of Al incorporation in the compound AlGaN for different V/III ratios in the growth chamber. The incorporation efficiency of aluminium drops abruptly, from 0,9 to under 0,2, when the V/III ratio exceeds 900. Parasitic reactions must occur beyond this value that impede a nominal AlGaN growth.

Hence, for the growth of structures within the frame of this project, we performed

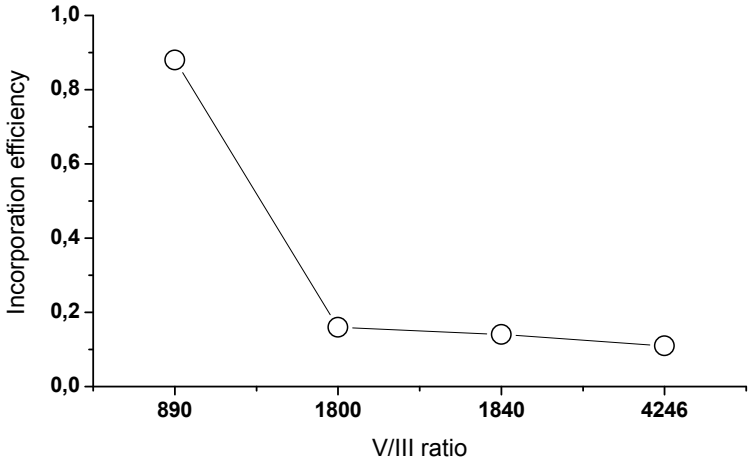

(a) Al incorporation efficiency as a function of V/III ratio

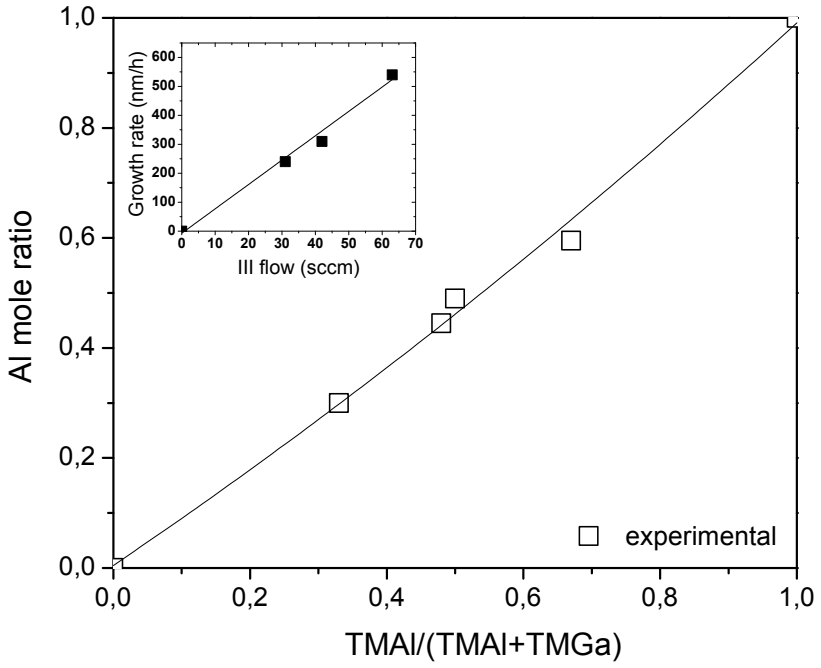

(b) Al-mole ratio as a function of TMAl/III ratio

Figure 50: (a) Incorporation efficiency of aluminium in the solid phase as function of V/III ration for constant TMAl/III ratio equal to 25%. (b) Al-mole ratio in the solid phase (x) as function of TMAl/III ratio for a V/III ratio of 900.

Table 3: Specifications for a Fe-doped semi-insulating GaN standard templates on sapphire substrate (source: *Lumilog*).

Item Reference	STINS
Size	Ø 2''
Exlusion zone	5 mm from outer diameter
Thickness	typical 4 µm
Thickness uniformity	± 5 %
Threading Dislocations density	typical 8 x 10^8 cm^{-2}
Sheet resistance $R_\square$ (300K)	typical 10 MΩ

experiments with a constant V/III ratio of 900. To obtain AlGaN with an accurate control of the composition, we performed several growth while varying the TMAl/III ratio. In Fig. 50(b), the aluminium composition in the solid phase is displayed as function of the TMAl/III ratio for a constant V/III ratio of 900. Under these conditions, it allows us to obtain a linear incorporation in the solid phase according to the proportioning of precursors in the gaseous phase.

6.2 Standard AlGaN/GaN HEMT growth (first HEMT campaigns)

6.2.1 Growths performed

Our first goal is to get the 2DEG in a conventional AlGaN/GaN HEMT device, i.e. a reference structure for future comparisons. We use commercial Fe-doped semi-insulating GaN standard templates on sapphire substrate (STINS) from *Lumilog*. Specifications for these substrates are given in Table 3.

The sheet resistance $R_\square$ is around $10^7\,\Omega$, which shows a good insulating behavior to prevent leakage in the bulk GaN. Additionally, the threading dislocations density, below $10^9\,cm^{-2}$, is relatively good. Higher quality substrates are available, but Lumilog's products are a good compromise between quality and cost for our first trials.

We perform regrowths on GaN pseudo-substrates, such as GaN templates grown on sapphire. Our first structures' designs, corresponding to Series 1, are shown in Fig. 51 and 52. The barrier layer is 30 nm thick, and the Al concentration between 17 and 20% on top of a 150 to 300 nm thick GaN buffer layer for T334 and T335. The Al concentration is low for the first trials as no calibration existed yet on our machine for HEMT structures. Even though, our main concern, in the first place, is the optimization of the interfaces AlGaN/GaN (barrier) and GaN/buffer (channel).

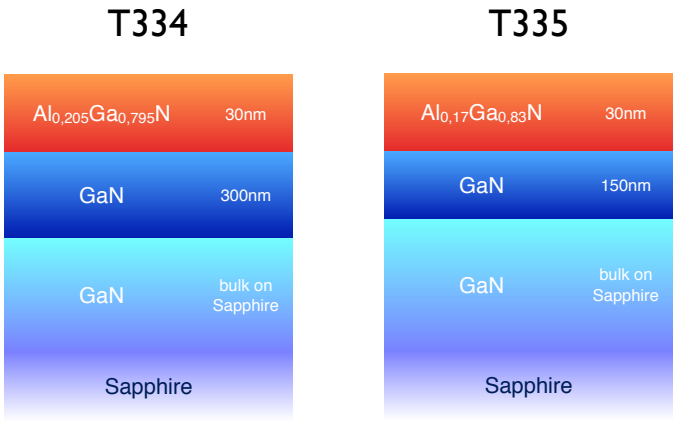

Figure 51: Series 1: standard AlGaN/GaN HEMT structures ; T334 (left) and T335 (right).

For structures T336, T337 and T344, we experimented for the first time HEMT structures comprising BGaN layers. The BGaN layer employed in these three structure has a boron incorporation of either 0.6% or 1.18% with a thickness of 90 nm.

6.2.2 Structural and morphological results

6.2.2.1 T334 & T335:

Structural properties of the different materials and their composition were analyzed using high-resolution X-ray diffraction. There is a good agreement between the simulated curve with the measured curve on the sample, which implies that the structural quality and interfaces between layers are very good.

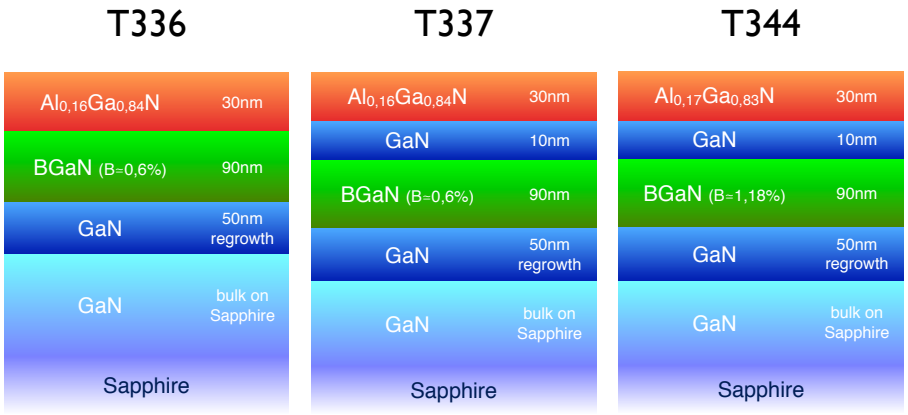

Figure 52: Series 1: HEMT structures comprising BGaN layers ; T336 (left), T337 (center) and T344 (right).

The morphology of the samples has been examined using AFM and SEM imaging. Figure 53 (a) exhibits images obtained for the structure T335. The surface of all our samples present the same morphology than substrates on which they were grown. In Fig. 53 (a), atomic steps and terraces are clearly recognizable which is a sign of a good morphological quality. On the other hand, crystallographic defects, or dislocations, that occur in the bulk, originate in *V-defects* on the surface (see Fig. 53 (b)). V-defects are holes, in the shape of an inverted hexagonal pyramid which emerge from threading dislocations (TDs) [110] and that are characteristic of an epitaxial regrowth. More precisely, on the SEM image, larger defects correspond to screw dislocations while smaller ones to mixed dislocations. However, the roughness was evaluated around 0.35 nm within an area devoid of any V-defect, which agrees with the good morphology observed. The density of V-defects was estimated at $10^8\,\mathrm{cm}^{-2}$ by quantifying them on a $5\mu m \times 5\mu m$ window.

In fact, V-defects appear with growth of GaN on SiC or Sapphire substrates, i.e. lattice-mismatched substrates. Such heteroepitaxial depositions are believed to be responsible for the formation of these defects, keeping in mind that the discrepancy

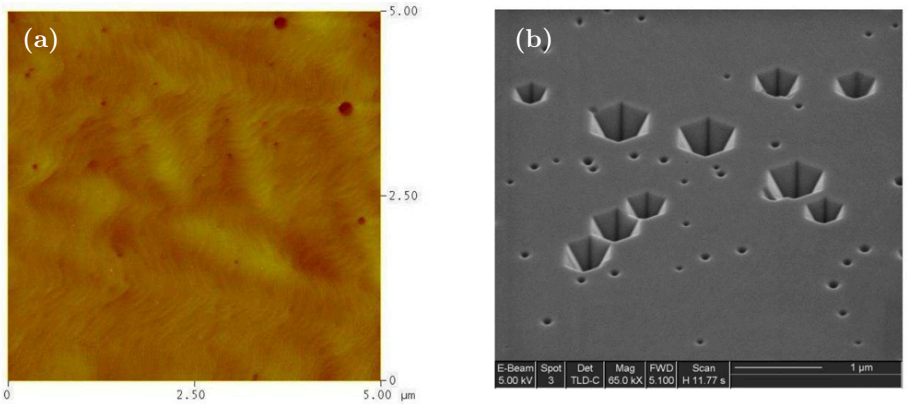

Figure 53: Morphology of the structure T335. (a) AFM image on a $5\mu m \times 5\mu m$ window showing the good morphological quality and (b) SEM image of the surface where distinctive holes, known as V-defects, can be observed (SEM performed at the IEMN).

between thermal expansion coefficients of GaN and the foreign substrate further aggravates the phenomenon. Defects formed have a typical cross sectional shape of a "V". Figure 54 describes the formation of these hexagonally shaped defects [16]. As a result, we can see that as the thickness of the growth layer increases, the area of V-defects becomes larger. Dimensions of the V-defects determined from AFM images on our structures do fit, proportionally to their total thickness, the theoretical formula indicated in Fig. 54. Subsequently, the size of V-defects is logically larger for structure T409 as its thickness is greater. Correspondingly, reflectance of layers, that is monitored *in-situ* during growth, diminished drastically as layers grew since apertures of V-defects expanded.

Considering that V-defects are most probably due to TDs already existing on templates employed for our growths, and knowing that the TD density is up to $8 \times 10^8\,\mathrm{cm}^{-2}$ (see Fig. 3), we can consider that it provides a *prima facie* evidence of the good quality of our structures as the V-defect density remains in the same order of magnitude. Allegedly, low-temperature growth, as it occurs for InGaN growth, is a cause of V-defect formation. For comparison, Johnson *et al.* showed that growth

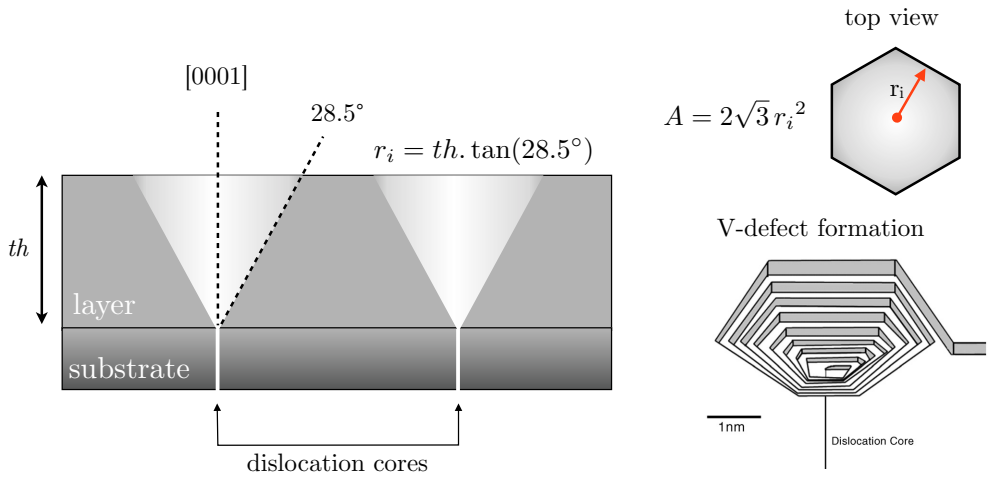

Figure 54: Schematic of V-defects originating from a dislocation core [16].

of InGaN multiple quantum well structures on low defect density templates ($\sim 2 \times 10^8\,\mathrm{cm}^{-2}$) led to V-defect densities around $10^{10}\,\mathrm{cm}^{-2}$ [111].

6.2.2.2 T336 & T336 & T344:

Concerning our first devices comprising BGaN layers, we systematically observed a morphology corresponding to a 3D growth with not well-defined interfaces between the different material. As seen in Fig. 55(a), the AFM imaging exhibited surfaces composed of 10-100 nm large grains, which must evidently constitute the bulk material as well. As a consequence, in the X-ray diffraction measurements, this loss of coherence results in the absence of thickness-related interference fringes around the diffraction peak for AlGaN (see scan $\omega - 2\theta$ in Fig. 55(b)). Moreover, no peak associated to BGaN was identified most probably because the layer was not thick enough (less than 100 nm).

These preliminary results suggest that the employ of thick BGaN layers is detrimental for the growth of layers on top of it.

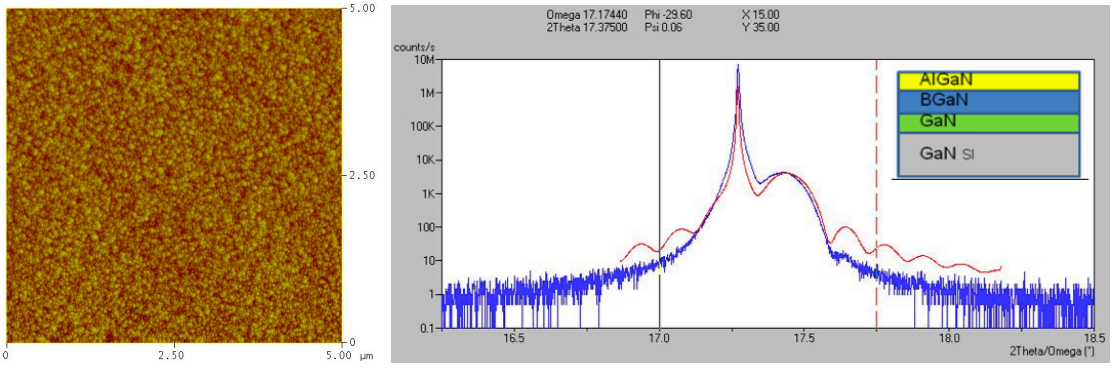

(a) (b)

Figure 55: Morphology of structure T336 containing BGaN: (a) the AFM image on a $5\mu m \times 5\mu m$ window shows a degraded surface composed of 10-100 nm large grains ; (b) scan $\omega - 2\theta$ XRD measurement exhibiting the absence of thickness-related interference fringes around the diffraction peak for AlGaN.

6.2.3 Device results

We manufactured the first devices from our structures at the IEMN. To that end, contacts must be inserted, with proper isolations. A prior acid cleaning with no recess is done before metallization. Ohmic contacts were made with Ti/Al/Ni/Au alloys followed by a thermal annealing and isolation with He^+ implantation. The mask used, called *Spirou*, is shown in Fig. 56(a), and a picture obtained by SEM of an actual contact is shown in Fig. 56(b).

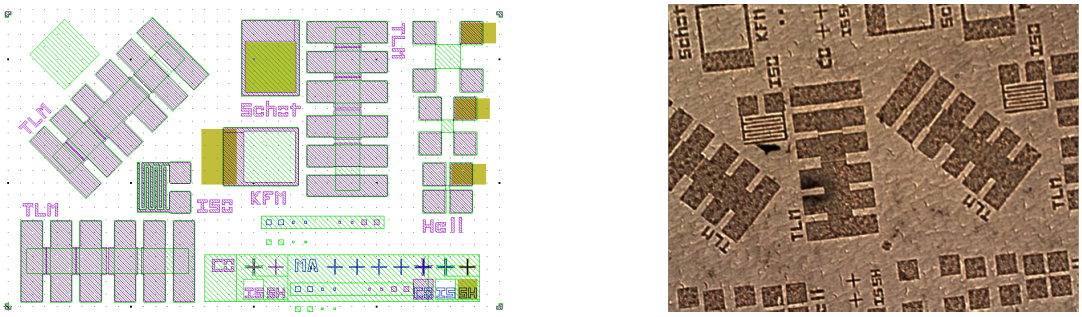

(a) *Spirou* mask schematic (b) *Spirou* mask deposited

Figure 56: *Spirou* mask used for electrical characterizations with its schematic (left) and a SEM picture obtained of the mask deposited on a HEMT (right).

Capacitance-voltage (CV) and Hall measurements were performed to evaluate the

Table 4: Data derived from Hall measurements on Series 1 samples. No structure exhibits distinctive marks of a HEMT behavior with a well-confined gas.

Series 1	**T334**	**T335**	**T336**	**T337**	**T344**
R ($\Omega/\square$)	603	239	438	484	542
n_s (cm^{-2})	1.16×10^{16}	1.83×10^{15}	7.70×10^{14}	3.88×10^{15}	2.05×10^{14}
μ_n ($cm^2/V.s$)	2.8	14.3	20.2	16.2	28.9
Hall coefficient (C/m^2)	1.21	1.17	1.10	1.04	1.52

2DEG transport properties in our HEMT devices. The Hall coefficient was determined to derive the mobility and the sheet resistance. A high mobility and a low sheet resistance are notably distinctive marks of a good structural quality at the AlGaN/GaN interface where the gas lies. Similarly, a large 2DEG density from CV measurements denotes a better power-handling capability. All processed structures exhibited a similar behavior with Hall measurements (see Table 4):

- a sheet resistance varying between 250 and 700 $\Omega/\square$,
- a carrier density varying between 1.5×10^{15} and 2×10^{16} cm^{-2},
- a mobility varying between 0.4 and 37 $cm^2/V.s$.

Only the structure T344 demonstrates different results, namely:

- a sheet resistance varying between 950 and 2200 $\Omega/\square$,
- a carrier density varying between 5×10^{13} and 5×10^{14} cm^{-2},
- a mobility varying between 13 and 39 $cm^2/V.s$.

Undoubtedly, no structure is exhibiting characteristic figures of the existence of a 2DEG, even standard AlGaN/GaN structures which have a good structural quality.

This phenomenon has already been reported when employing regrowth on templates [112]. It appears that impurities are accumulated at the regrowth interface and drastically impede electrical properties. This is explained by the appearance of a parallel parasitic conduction channel. It can easily happen during surface preparation or when samples are in contact with foreign atmospheres other the growth chamber. In fact, carrier densities derived are typical of a conduction in the bulk and not confined within a 2DEG.

6.2.4 Regrowth interface

To verify our theory, we further investigated this contamination by performing SIMS analysis on our samples. Figure 57 shows results obtained for structure T334. Principal dopants relevant for nitrides, and already known to appear in our growth chamber, were monitored: Oxygen, Carbon, and Silicon through its two isotopes ^{28}Si and ^{30}Si.

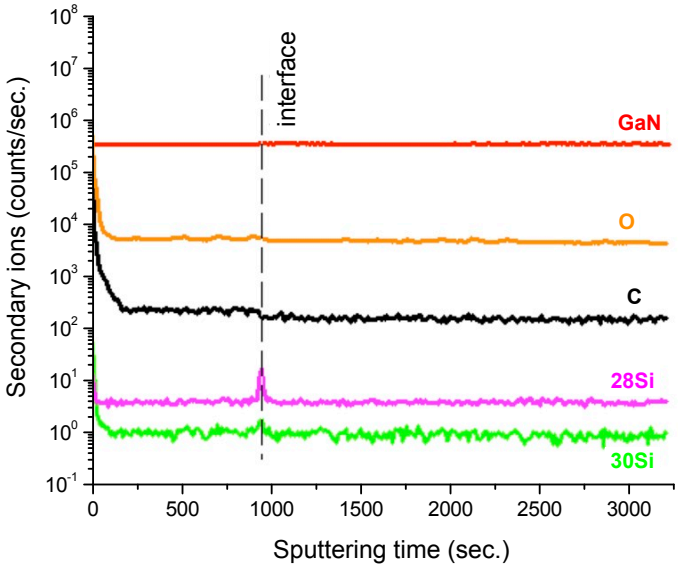

Figure 57: SIMS profiles of impurities concentrations in the T334 structure (measurements were done at a partner lab named GEMaC - CNRS Bellevue, France). In a dynamic mode, the sputtering time translates into depth and the number of counts per second of secondary ions represents their relative density at a given depth 3.2.3. A distinctive spike of Si is observed at the regrowth interface.

The profile of the element ^{28}Si gives evidence of a spike of impurity concentration

around the interface. Surface probing of the crater generated during SIMS analysis using a profilometer indicated the actual position of the spike which was 330 nm from the surface. This result agrees with thicknesses expected for this structure (see Fig. 51) and do correspond to the regrowth interface. The spike observed for the element ^{30}Si is less significant but is notably located at the same depth.

We performed simulations of a HEMT structure by adding a thin layer of impurities, i.e. typically a GaN layer 5 nm thick n-doped with a concentration of $10^{20}\,cm^{-3}$, that would lie at regrowth interface. This creates a quantum well that interfere with the 2DEG and evidently induces parallel conduction detrimental for HEMT operation. Hence, templates tend to be contaminated mostly by air exposure, which induces in turn parasitic conduction channel [112].

In light of results obtained with Series 1, we carried out experiments towards the optimization of the regrowth interface on templates by introducing an AlGaN layer.

6.3 Introduction of AlGaN in the buffer (second HEMT campaigns)

Structures grown in the second campaign are depicted in Appendix A as Series 2 batch (see Fig. 76). We decided to increase the aluminium composition to raise the piezoelectric field of the barrier and, hence, improve the confinement. Furthermore, in order to circumvent issues encountered with contaminants at the regrowth interface, we explored designs comprising an AlGaN layer right at the regrowth interface similarly to double-heterojunction HEMTs (or DH-HEMTs), since AlGaN growth was already studied. Structure T406 was the standard AlGaN/GaN HEMT, whereas others comprise an AlGaN layer in the GaN bulk. Typically, the AlGaN barrier layer had a thickness varied between 20 to 40 nm with a Al-mole fraction of 30%. Only structure T406 was based on a standard AlGaN/GaN design. Templates were from Lumilog, the same employed the Series 1.

6.3.1 XRD analysis

Optimizations described in previous Sections were put into use and XRD analysis is a mean to verify the good crystalline quality. Structural properties of grown layers were all analyzed through XRD in both real and reciprocal space. Figure 58(a) shows the X-ray diffraction spectrum of HEMT structure AlGaN/GaN T406. The main peak is the one from GaN and the larger one is due to the AlGaN barrier layer. Interference fringes related to thickness are indeed well defined, hence guaranteeing the good structural quality of the growth. In addition, the blue curve simulated with the XPert Epitaxy software was perfectly fitted the experimental red curve so as to determine compositions and thicknesses, which assesses structural and interfaces quality as well. The Al content of 26% in the barrier layer of structure T406 was confirmed this way as for values of other structures.

The X-ray diffraction spectrum of HEMT structure AlGaN/GaN/AlGaN T408 is exhibited in Fig. 58(b). Remarks made for T406 remains the same: firstly, results shows a good structural and interfacial quality with distinctive peripherical thickness-related interference fringes and, secondly, the additional peak of the AlGaN layer in the buffer (Al content of 7%) can be noticed close to the main GaN peak. Moreover, a reciprocal space mapping of structure T403, which has a similar design than T408, is shown in Fig. 58(c). Three clearly defined regions stand out from the mapping in the orientation (114). In the center, the main area is attributed to GaN and, perfectly aligned vertically, the 2 other peaks correspond to AlGaN. The smaller one just above it is due to the AlGaN layer in the buffer with an Al content of 4.3% and the bigger, further up, is related to the AlGaN barrier layer. The vertical axis at stake corresponds to plane (110) which implies that both AlGaN layers are 100% strained to be lattice-matched with GaN's lattice parameter.

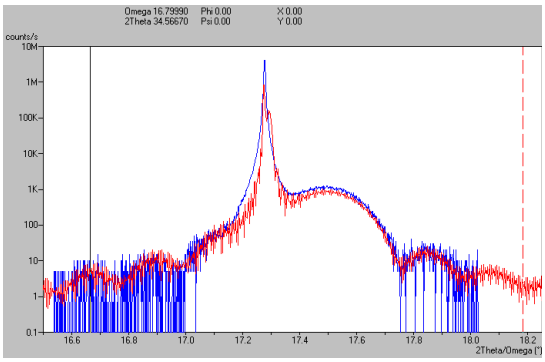

(a) XRD on T406.

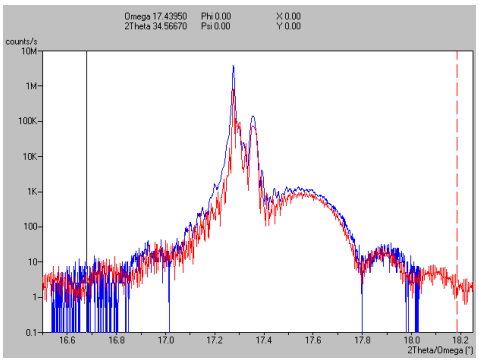

(b) XRD on T408

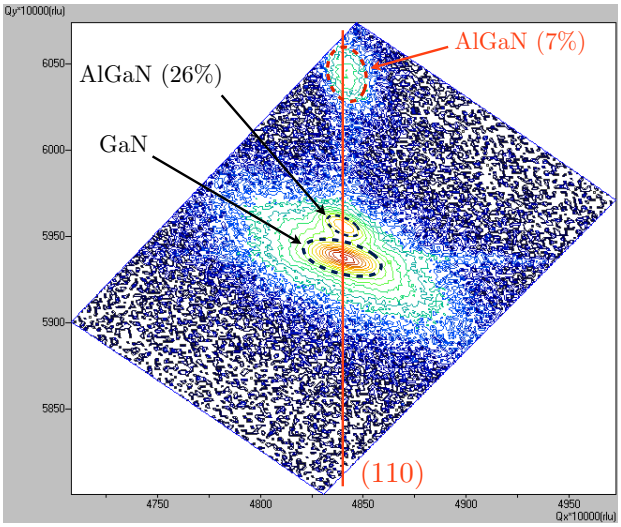

(c) RSM on T403

Figure 58: (a) X-ray diffraction spectrum of HEMT structure AlGaN/GaN T406 ; (b) X-ray diffraction spectrum of HEMT structure AlGaN/GaN/AlGaN T408 ; (c) reciprocal-space mapping (RSM) along 114 of HEMT structure AlGaN/GaN/AlGaN T403. The alignement of the different areas corresponding the different layers implies that all layers are fully strained on GaN.

6.3.2 AFM analysis

The surface morphology was investigated with AFM analysis to assess the influence of the introduction of an AlGaN layer in the buffer. Figure 59 reports images obtained. The morphology is 2-dimensional with distinctive atomic steps and terraces. The surface roughness was found between 2.7 and 3.7 nm RMS (R_q) for structures T406, T407 and T408. However, structures T403 and T409 exhibited values up to 15 nm RMS. The poor quality of these structures, compared to others, can be explained by their larger total thicknesses. Manifestly, the degradation of the surface originates in defects whose influence is enhanced as thickness increases.

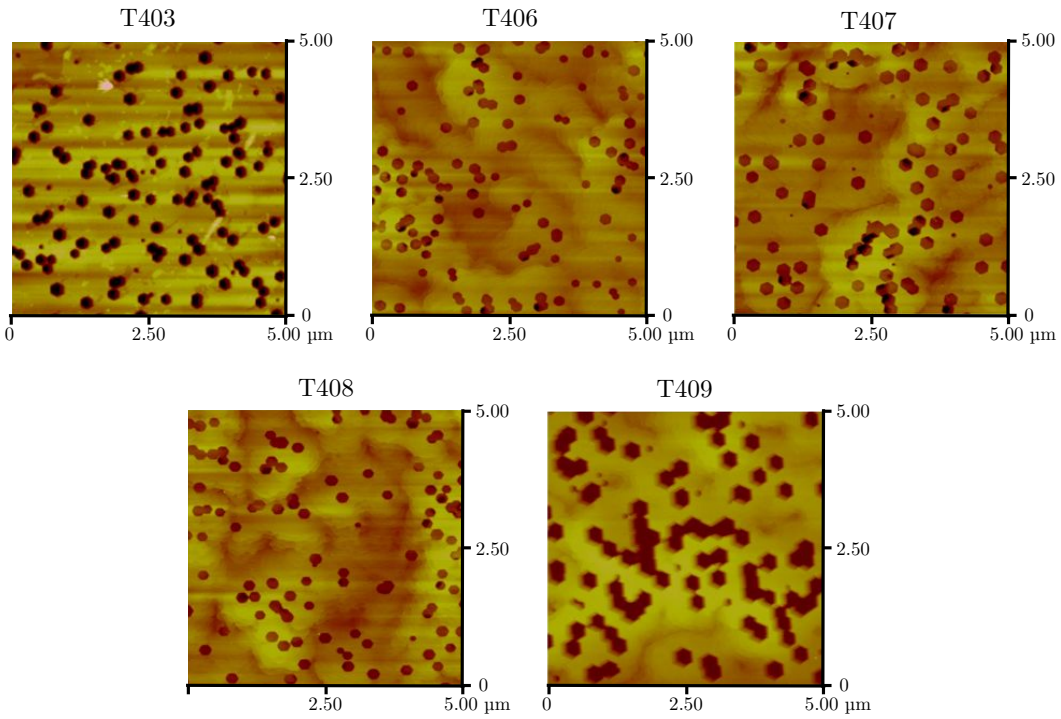

Figure 59: AFM measurements on Series 2 structures with a $5\mu m \times 5\mu m$ window.

We can notice in all pictures a high density of V-defects already observed in Series 1. The density is approximately $8 \times 10^8\,\mathrm{cm}^2$. As mentioned previously, V-defects originates from dislocations generated at the regrowth interface (as TDs).

6.3.3 Capacitance-voltage measurements

Capacitance-voltage (C-V) measurements allow to extract doping level and carrier density of the 2DEG, which are important characteristics to assess the performance of a HEMT structure, provided that the interface barrier/channel (i.e. AlGaN (barrier) / GaN) was good enough. C-V measurements were performed on all structures of Series 2 for a frequency range of 10-400kHz.

A discrepancy occurs between results of T406 and others comprising an AlGaN layer in the buffer. Fig. 60(a) shows C-V measurements on standard AlGaN/GaN structure T406 that are the best results of the series, evidently reflecting good interfacial and structural qualities. The sharp increase in the capacitance (i.e. the pinch-off) around -3 V indicates a dominant conduction at the interface, proof of a good confinement and low trap density. As illustrated in the Fig. 60(b), the residual capacitance after the pinch-off (voltages below -3 V) is very low for 10-400 kHz, close to 5 pF, which indicates a low density of traps in the buffer and a residual level below $10^{13}\,\mathrm{cm}^{-3}$. Furthermore, the density of carriers profile, deduced from C-V measurements, is displayed in Fig. 60(d) where we observe a sharp increase of the density close to the surface, which corresponds to the 2DEG. The density of carriers in that latter is estimated to $7.2 \times 10^{12}\,\mathrm{cm}^{-2}$. Besides, residual concentrations in the buffer are below $10^{16}\,\mathrm{cm}^{-3}$ at a depth of 2-4 μm, which is located at the interface GaN/Sapphire of the commercial GaN template.

Conversely, other structures such as T408 exhibit irregular results as shown in Fig. 60(c). Though a pinch-off is visible at high frequency for 400 kHz around -3 V, it is not the case at lower frequencies. Residual capacities beyond pinch-off (i.e. below -3 V) remain quite high and tend to increase with lower frequencies. This clearly reflects a high density of defects and leakage in the buffer.

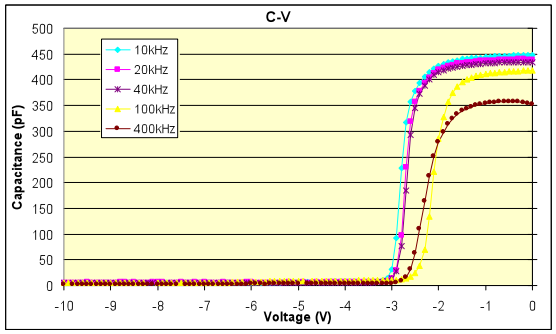

(a) C-V on T406.

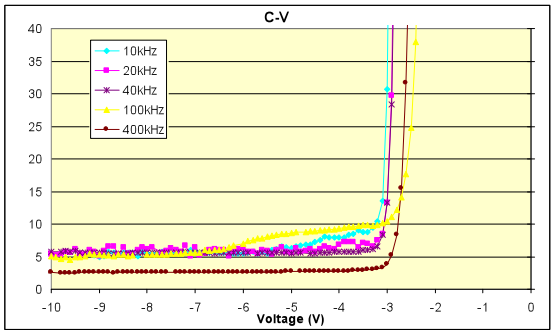

(b) C-V on T406 (zoom).

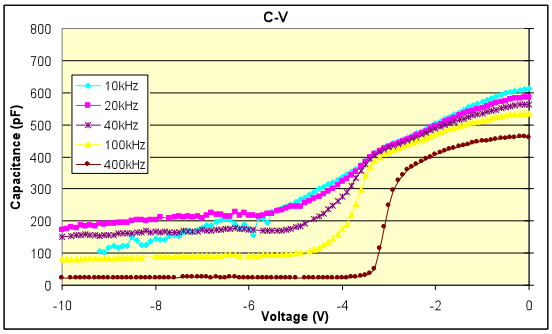

(c) C-V on T408.

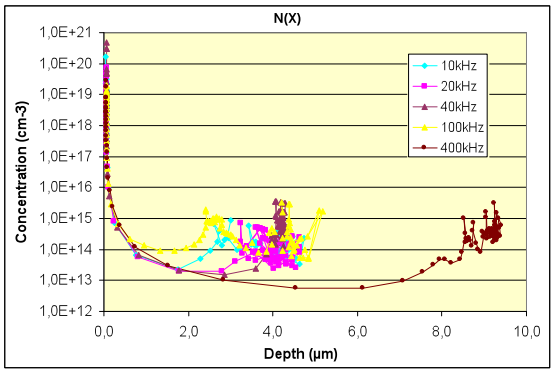

(d) Carrier density on T406.

Figure 60: (a) C-V measurements on structure T406 at different frequencies in 10-400kHz range ; (b) Zoom view of the residual capacitance in the buffer ; (c) C-V measurements on structure T408 at different frequencies in 10-400kHz range ; (d) Carrier density deduced from C-V measurements of structure T406.

6.3.4 SIMS analysis

To further investigate degradation observed in some structures of Series 2, we performed SIMS analyses as illustrated in Fig. 61. Carbon, oxygen, hydrogen and silicon, all negative ions, were detected using cesium primary ion beam (Cs^+). Alternately, an oxygen primary ion beam (O_2^+) was dedicated to the detection of positive ions such as magnesium, iron and zinc.

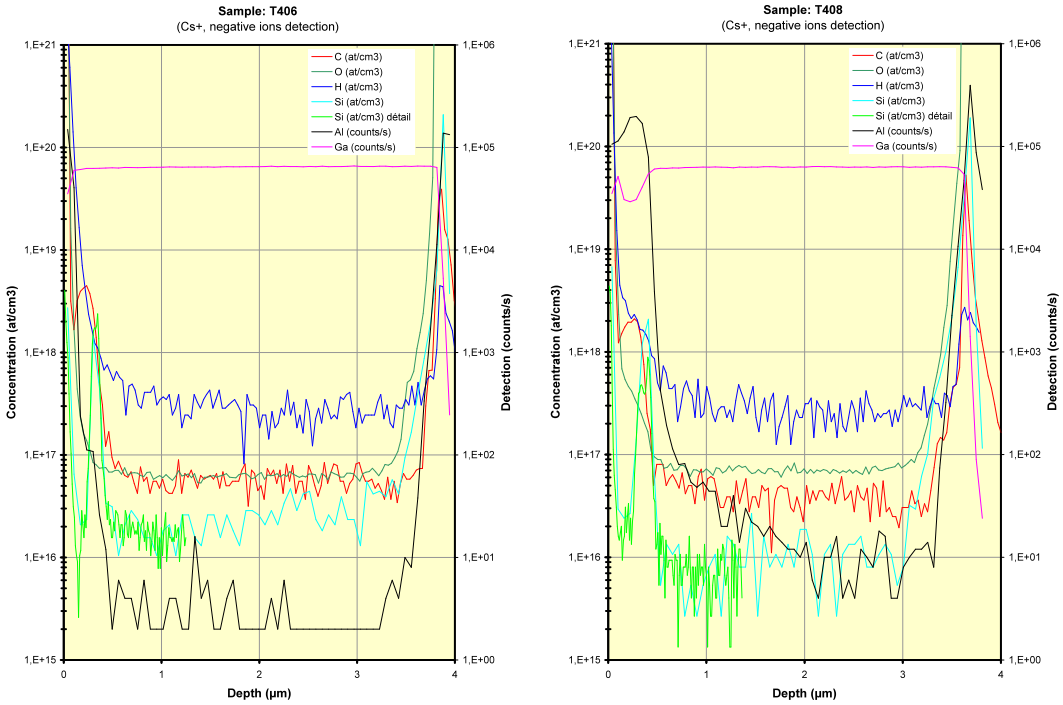

(a) SIMS on T406.

(b) SIMS on T408.

Figure 61: (a) SIMS depth profiles of HEMT structure AlGaN/GaN T406 with caesium primary ion beam ; (b) SIMS depth profiles of HEMT structure AlGaN/GaN/AlGaN T408 with caesium primary ion beam.

For all structures, we observe 2 relatively high peaks of carbon ($2to5 \times 10^{18}\,\mathrm{cm}^{-3}$) and silicon ($4\times10^{17}$ to $2\times10^{18}\,\mathrm{cm}^{-3}$) right at the depth corresponding to the regrowth interface. Moreover, carbon and silicon are close to $10^{16}\,\mathrm{cm}^{-3}$ within the GaN template. Only zinc concentration seems lower in the buffer of HEMT T406 compared to others.

6.3.5 Device results

We chose to process structure T406 only as it exhibited the best results. Thus, our partner at IEMN performed measurements using metal contact and the mobility of the 2DEG was found equal to 1500 $cm^2\ V^{-1}.s^{-1}$. This result is a typical state-of-the-art value demonstrating a good performance for a first HEMT structure grown by our lab.

Results of the previous series suggest that:

- a standard AlGaN/GaN HEMT structure was obtained with results close to typical performances reported in the literature,
- X-ray diffraction measurements showed very good structural quality with fully strained layers,
- the introduction of an AlGaN layer in the buffer was detrimental to interfacial quality as well as HEMT behavior due to traps and defects,
- impurities originating from the regrowth interface were still existing and not even the AlGaN layer suppressed their influence.

6.4 Reproducibility of standard HEMTs growth (third HEMT campaign)

The philosophy on the third campaign, whose structures are shown in Fig. 77 of Appendix A, was to assess our capability to grow standard AlGaN/GaN HEMT structures. Only two types of designs were selected: 3 structures identical to T406 of series 2, and 3 other structures similar to T406 but with a higher Al content in the barrier.

X-ray diffraction measurements on this series showed again very good structural quality. As previously, the AlGaN layer is fully strained to be lattice-matched with GaNs lattice parameter. Figure 62(a) shows results for structures identical to T406

and compared to that latter. AlGaN buffer and barrier layers peaks are very well defined. The excellent fit between experiment and simulation as well as Pendellosung fringes proves the very good structural quality of the whole structure.

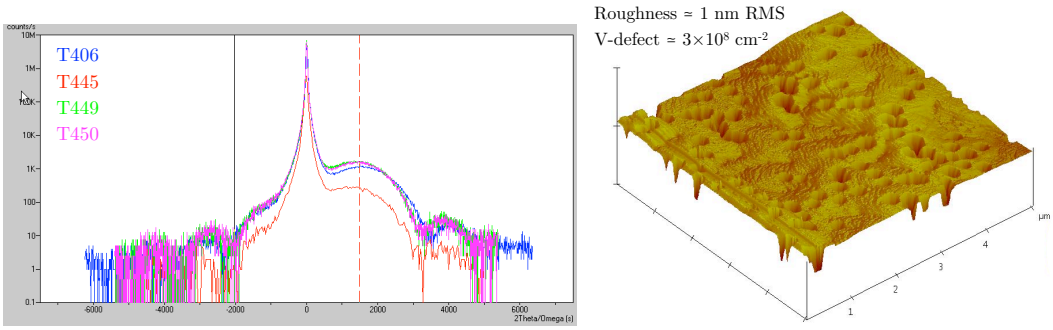

(a) XRD on Series 3.

(b) AFM on T445

Figure 62: (a) Compared 2theta/omega X-ray diffraction spectrum of HEMT structures AlGaN/GaN T406, T445, T449 and T450 ; (b) AFM measurements on structure T445 with a $5\mu m \times 5\mu m$ window showing a very smooth surface roughness of 1nm.

Regarding surface roughness, AFM measurements exhibited values between 1 to 4 nm RMS, but V-defects were still present with our typical density (see Fig. 62(b)).

C-V measurements have been performed by our partner from Thales at the 3-5 lab using mercury drop probes. Two structures showed good results: T445 and T448, comprising 25 % and 33 % of Aluminium, respectively. In Fig. 63, we can see a reasonably defined pinch-off in each C-V profiles with a very low capacitance after pinch-off. Besides, residual concentrations of carriers in the buffer is below $10^{15}\,\mathrm{cm}^{-3}$. It should be noted that the noise in concentrations observed in Figs. 63(b) and 63(d) occurs at a depth of 4 μm, for which the accuracy of data is not assessed.

Nevertheless, other structures did not reach similar satisfying performances. Results displayed in Fig. 64 for structures T449 and T450 (identical to T406) brings back the issue related to the regrowth interface. For both structure, the residual capacitance after pinch-off is quite high, clearly reflecting the presence of a large quantity of traps in the buffer. This assumption is verified by carrier density profiles exhibiting

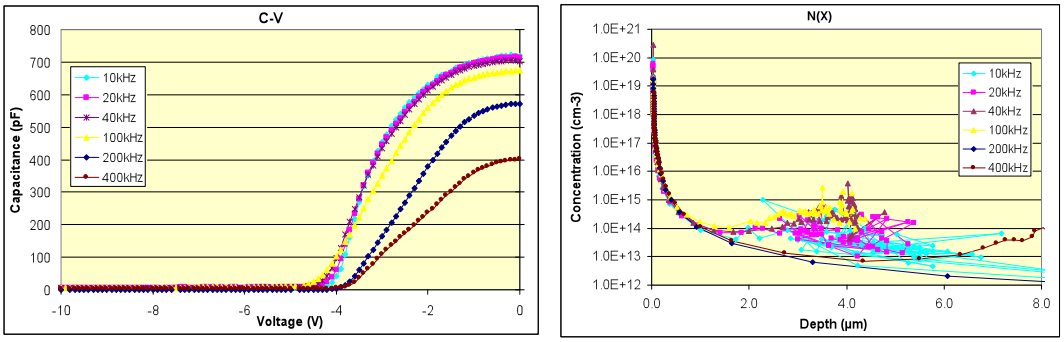

(a) C-V on T445.

(b) Carrier density on T445.

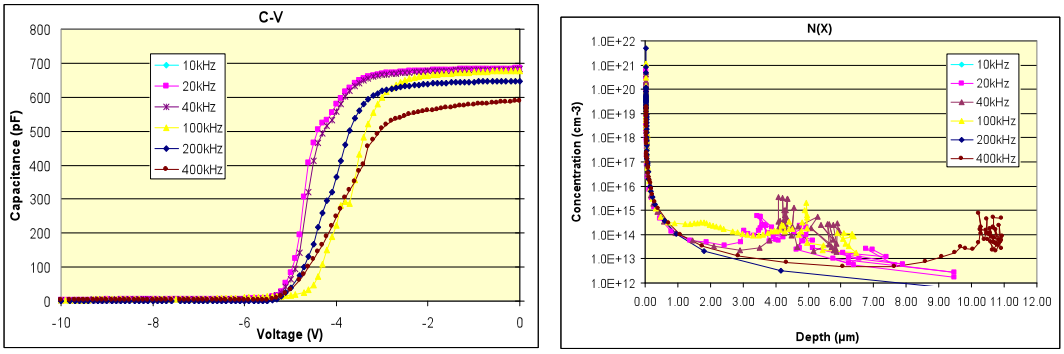

(c) C-V on T448.

(d) Carrier density on T448.

Figure 63: (a) C-V measurements on structure T445 at different frequencies in 10-400kHz range ; (b) Carrier density deduced from C-V measurements of structure T445 ; (c) C-V measurements on structure T448 at different frequencies in 10-400kHz range ; (d) Carrier density deduced from C-V measurements of structure T448.

a sharp increase at the regrowth interface certainly due to impurities already existing on the surface of the template prior to deposition.

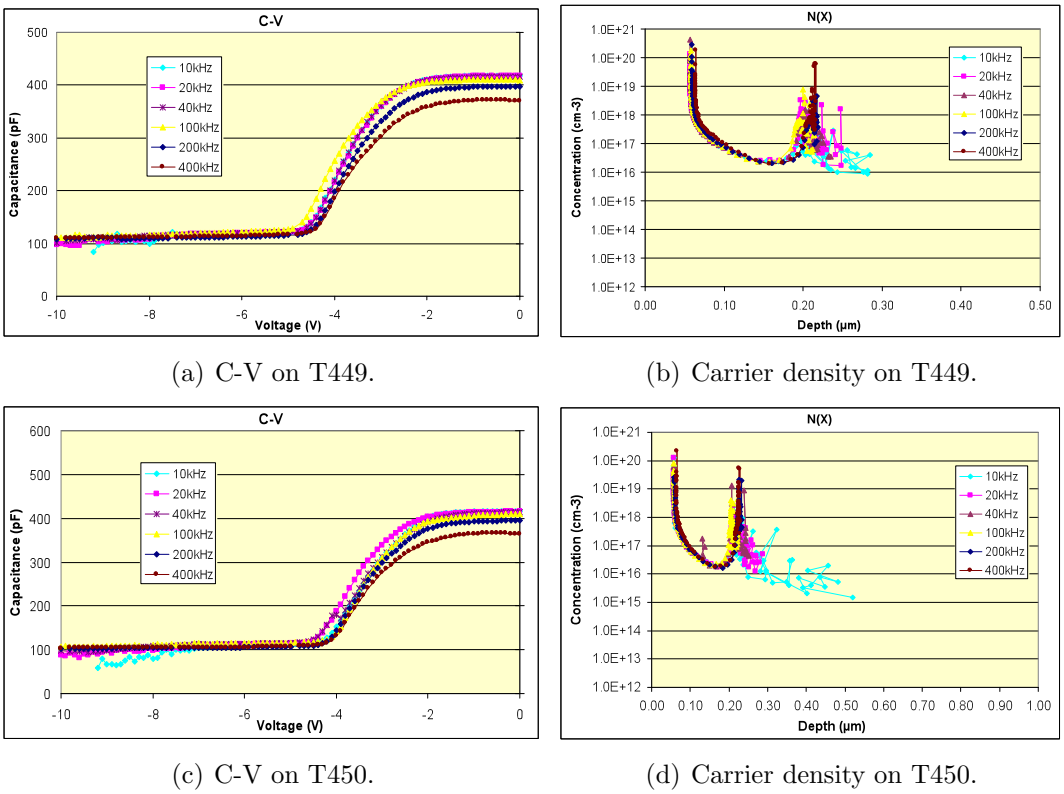

(a) C-V on T449.

(b) Carrier density on T449.

(c) C-V on T450.

(d) Carrier density on T450.

Figure 64: (a) C-V measurements on structure T449 at different frequencies in 10-400kHz range ; (b) Carrier density deduced from C-V measurements of structure T449 ; (c) C-V measurements on structure T450 at different frequencies in 10-400kHz range ; (d) Carrier density deduced from C-V measurements of structure T450.

Consequently, good results in agreement with previous results were obtained assessing our capability to reproduce them. The interface impurities impede though electrical behavior as observed on several structures.

6.5 Standard HEMTs growth on following series

For all subsequent series, a standard HEMT structure was grown for comparison purpose. Results obtained, and reviewed in the next Chapter, are in accordance with results presented above. However, we show that novel design incorporating BGaN layer can lead to improved performances with better confinement of the carrier and,

hence, higher mobility and lower sheet resistance.

CHAPTER VII

EXPERIMENTAL WORK: BORON HEMT STUDY

After a series of experiments with standard AlGaN/GaN HEMTs, we achieved device quality but demonstrated limitation due to leakage in the buffer.

Our goal now is to experiment novel designs realized with boron-based alloys. Eventually, the ultimate goal to be achieved is to evaluate the potential of BGaN back-barriers for standard AlGaN/GaN HEMTs following our simulations.

To this end, it is essential to conduct a research regarding thick layers of BGaN, dedicated to its growth as well as its characterization, in order to corroborate key simulation parameters characterizing this novel material.

In parallel, the second path is to investigate thin layers of BGaN and their employ in conventional AlGaN/GaN structures. Firstly, BGaN can be used as a back-barrier for which we need characterize its role and its impact on performance. Moreover, we need to determine the optimal thickness and distance from the channel leading to the best results. In this case, its role and performance must be determined. Secondly, another idea that arisen in the course of our experimentation is to use BGaN thin layer as a compensating layer at the regrowth interface.

7.1 Study of thick BGaN layers

7.1.1 Growth of BGaN layers

Several batches of BGaN layers were grown on 3.5 μm thick c-plane-GaN/ sapphire templates by MOVPE in our custom-made growth chamber. The parameters were kept similar to growths presented in Chapter 4 with N_2 as the carrier gas and trimethylgallium (TMG), triethylboron (TEB) and ammonia (NH3) as precursors for gallium, boron and nitrogen, respectively. The temperature of growth was 1000°C with a V/III ratio of 830 while the reactor pressure was at 133 hPa (100 Torr). To monitor the boron incorporation, we varied the molar ratio of TEB in the vapour phase (i.e. TEB/(TMG+TEB)). We employed HR-XRD $2\theta/\theta$ scans to determine more precisely boron contents of the BGaN samples. As a result, the composition of the samples was deduced from Vegards law using the following lattice parameters: $c_{BN} = 2.55\,\text{Å}$ and $c_{GaN} = 5.185\,\text{Å}$. In addition, AFM measurements were used to assess the good morphological quality of our structures.

7.1.2 Hall measurements on BGaN layers

In Chapter 4, we discussed the highly resistive characteristics of BGaN materials as demonstrated by our group. Our aim is therefore to confirm these results within the scope of this study. We performed Hall measurements on similar structures to assess this result. Three BGaN layers of 400 nm were grown on GaN templates with boron-mole fractions of 0.65, 0.86 and 0.95, respectively, along with a 450 nm thick reference structure with 0% of boron. The low values of boron incorporation, below 1%, are chosen to keep a good structural quality based on results reviewed earlier.

Structures were processed and tested by our partners at the IEMN. As structures containing boron happened to be very resistive, only sheet resistances could be deduced from Hall measurements performed. In addition, for comparison purpose, same measurements were carried out on AlGaN structures grown on GaN templates with

a reference structure with no aluminium, one comprising 7% of aluminium, and two others containing 25% of aluminium. Figure 65 reports results obtained on the two series of structures.

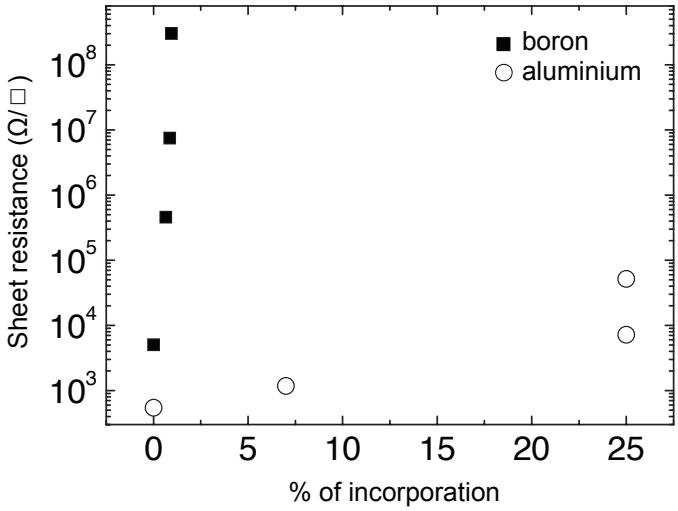

Figure 65: Resistivity in BGaN and AlGaN thick layers as function of boron or aluminium incorporation, respectively.

The drastic increase of the resistivity for BGaN samples, notably in comparison with AlGaN samples, supports results already published by our group [14] (see Section 4.4). It is most probably due to a passivation of dopants by boron within the GaN matrix. This effect, appearing more specifically for percentage below 1% of incorporation, could be exploited in device structures with thin BGaN films: the high resistivity encountered by electrons would serve as an efficient barrier to unwanted leaks.

7.1.3 Optical characteristics of BGaN layers

We characterized BGaN layers with room temperature measurements at 244 nm using the PL setup. It allowed us to determine the bandgap of BGaN layers and see how it corroborates results from our group regarding the existence of a bandgap bowing appearing for little boron alloying.

7.1.3.1 First batch

We performed measurements on two samples: one reference sample with no boron, and a second one comprising 0.89% of boron. The setup employed is the one described in Fig. 23. The input current powering the Ar-ion tube was at 40 A with output power of the 488 nm laser beam of 34 mW. We observe that all the illuminated samples show a distinctive yellow glow, which is characteristic of nitrides.

Figure 66 depicts photoluminescence spectra obtained. The two spectrum possess a distinctive peak, but the BGaN structure exhibits a lower intensity compared to the reference structure. A possible explanation is that the introduction of boron induces structural defects impeding luminescence [113].

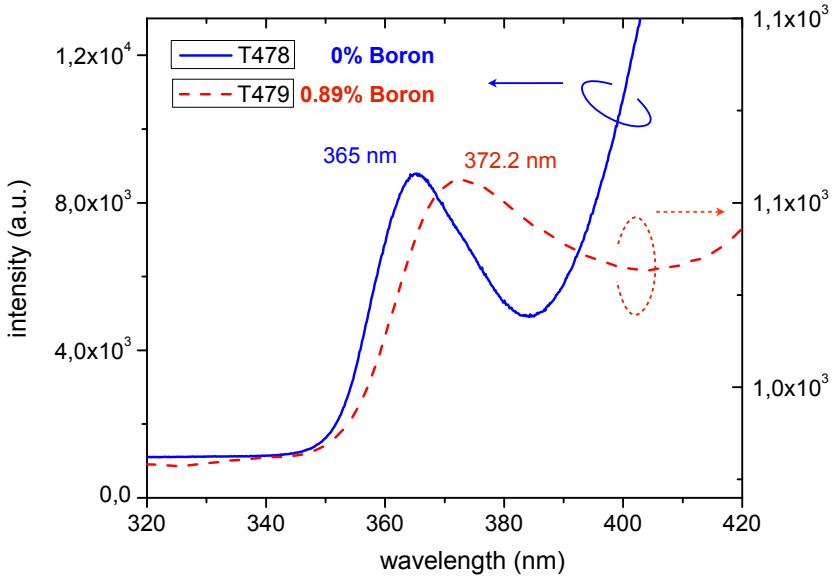

Figure 66: Photoluminescence at room temperature of BGaN structures of the first batch.

Furthermore, the peak of the reference structure corresponds manifestly to the first exciton A (see Section 2.1.1.2). Its theoretical value is situated at 3.49 eV whereas, here, its value is much lower, down to 3.39 eV (365 nm). Reportedly, variations are due to a biaxial strain of the structure along the *c-axis*, but also to the nature of the substrate, the growth temperature, the thickness, etc. [114].

Regarding the peak of the of BGaN sample T479, it should correspond to a boron-mole fraction of 0.89% which is deduced from simulated fitting of the XRD data. The theoretical bandgap value associated to this boron incorporation can be derived from Eq. 52. Thus, the computed value of 372.7 nm is to be compared to the peak observed in Fig. 66 for sample T479 which is at 372.2 nm. Interestingly, values are well matching to each other, hence corroborating results from BGaN bandgap bending [10].

7.1.3.2 Second batch

As second batch of samples had been measured with the PL setup. Structures T673, T674 and T675 are BGaN layers on 3.5 μm thick c-plane-GaN/ sapphire templates, with increasing boron-content, 350 nm thick. Though sample T673's boron content was evaluated at 0.48%, only a range of 0.5 to 1% was estimated for the other two structures.

Figure 67 shows photoluminescence spectra obtained at room temperature. All structure show a distinctive peak at 363 nm corresponding to the main exciton transition of GaN (exciton A).

For both samples T673 and T674, a secondary peak can be noticed around 370 nm that is partly hidden as it merges with the broadened main GaN peak. As the boron-content increases, the intensity of luminescence diminishes, most probably due to structural disorder. Hence, T675 exhibits a much less intense spectrum. The inset in Fig. 67, which zooms on this curve, allows to clearly see a distinctive second peak at 371.9 nm. Again, the corresponding boron-content value can be derived from Eq. 52, i.e. 0.8%. Not only is it in good agreement with an expected value above 0.5%, but it also concurs with the peak observed in the first batch (see Fig. 66), hence proving a good reproducibility of results.

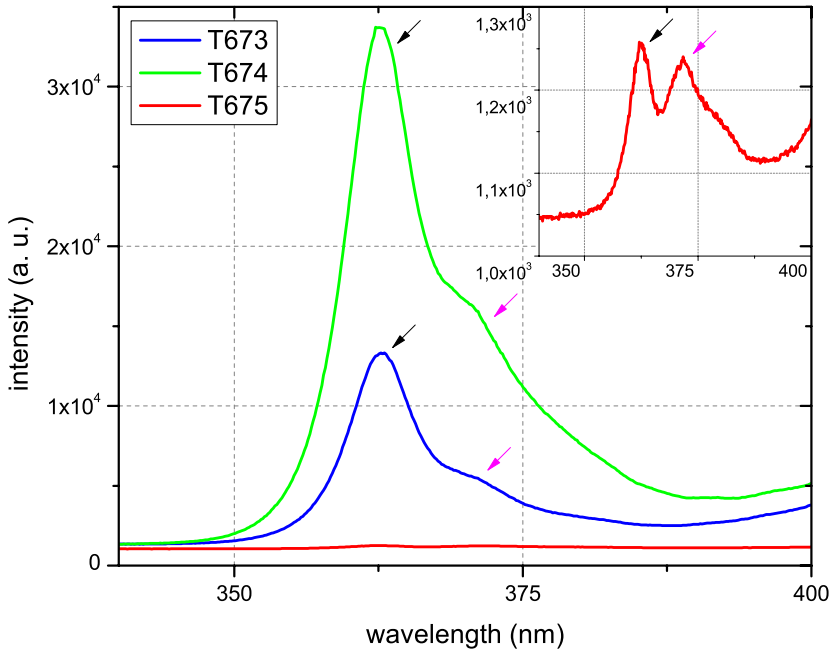

Figure 67: Photoluminescence at room temperature of BGaN structures of the second batch. Dark arrows point at the main exciton transition of GaN and magenta arrows point at the peak corresponding to BGaN.

7.2 Employ of thin BGaN layers

As seen in Chapter 5, we designed and simulated novel HEMT structures, based on a standard AlGaN/GaN stacking, with a thin BGaN layer. To assess our assumption that performances can be enhanced, several series of samples were manufactured, characterized and processed for device measurements. In this section, we focus our study on two series of samples where BGaN thin layers are used to serve two different purposes: either as a compensating layer at the regrowth interface (see Section 7.2.3 for explanations) or as a back-barriers to electrons.

7.2.1 Growths of Series 5 and 6

For Series 5 (see Appendix A), a reference structure, T572, was based on a standard AlGaN/GaN HEMT design exactly similar to T406. Moreover, the series is divided into two groups: structures T568 and T571 were meant for the employ of a BGaN layer

as a compensating layer (CL) at the regrowth interface (see Fig. 78) and structures T574-7 were used for the study of the BGaN back-barrier (BB) (see Fig. 79).

For the employ of a BGaN CL, as it is the first layer deposited, the thickness was supposed to be above 2 nm to go beyond the 3-dimensional growth occurring at the regrowth interface. Yet, we decided to keep the boron-content equal to 1 % to also avoid a 3-dimensional growth. Thus, the thickness was of either 2 or 4 nm (for T568 and T571, respectively).

Regarding the study of the BGaN back-barriers (or BB), two parameters were varied to optimize its effect on performances of the HEMT: firstly its distance from the channel (i.e. AlGaN/GaN interface) and secondly its thickness.

For Series 6 (see Fig. 80 of Appendix A), the reference structure, T602, was again based on a standard AlGaN/GaN HEMT design exactly similar to T406. In addition, an other standard HEMT structure,T603, was grown but, this time, with a higher Al-content in the barrier layer up to 30 %. Consequently, samples T604 and T605 were based on the same design, with 30 % of Al in the barrier, but with the introduction of a BGaN layer of either 1 or 2 nm. The distance from the channel was of 40 nm in both cases, similarly to T577.

7.2.2 Review of structural quality of Series 5 and 6

As we want to assess improvements brought by the introduction of a BGaN layer, we firstly need to ensure that no structural or morphological degradation is observed when compared to standard AlGaN/GaN structures using AFM and XRD analyses.

7.2.2.1 AFM analysis

AFM measurements were performed on Series 5 and 6 using the protocol described in Section 3.2.1.2. Table 5 presents results of Series 5. Compared to previous results of standard AlGaN/GaN structures of Chapter 6, surface roughness values are noticeably improved despite a V-defect density that remains in the same order of magnitude

Table 5: AFM measurements on Series 5 (all BB/CL layers comprise 1% of boron).

	no boron	with boron - CL		with boron - BB			
designation	T572	T568	T571	T574	T575	T576	T577
BB/CL thickness (nm)	-	2	4	2	1	1	1
R_q^{RMS} (nm)	0.85	3.455	> 5	2.062	1.257	2.646	1.817
V-defects density ($\times 10^8$ cm^{-2})	4.3	5.8	5.9	5.1	5.4	5.4	5.2

(see Section 6.3.2).

The introduction of a BGaN CL at the regrowth interface of structures T568 and T571 was rather detrimental to their surface quality in comparison with the standard structure T572. With R_q values beyond 3 nm, we can infer that the interface quality must be degraded when the bulk GaN was grown on top of the BGaN layer.

On the other hand, values obtained for HEMT structures comprising a BGaN BB, i.e. T574-7, are proof of a good quality and even slightly better than previously. However, no specific conclusion can be drawn when comparing structures, even sample T574, with thicker BB layer of 2 nm, does not exhibit a degraded surface roughness.

Concerning Series 6, results are displayed in Table 6. It can be observed distinctively that samples with a higher content of Al in the barrier exhibit lower surface roughness values. In addition, no distinctive degradation is observed with the introduction of a BGaN BB when comparing Figs. 68(a) and 68(c). Even structure T605, which has the thicker layer, has the best surface roughness value of the series. Finally, it should be noted that the V-defect density remains quite the same between T603 and T604 when comparing Figs. 68(b) and 68(d).

7.2.2.2 XRD analysis

On all structures of Series 5 and 6, XRD analysis showed good results with fully strained layers on GaN. As seen in Figs. 69(b) and 69(d), there is no distinctive

Table 6: AFM measurements on Series 6 (all BB layers comprise 1% of boron).

	no boron		with boron - BB	
designation	T602	T603	T604	T605
BB thickness (nm)	-	-	1	2
R_q^{RMS} (nm)	3.398	1.585	3.354	1.547
V-defects density ($\times 10^8$ cm^{-2})	4.1	6.1	5.2	5.1

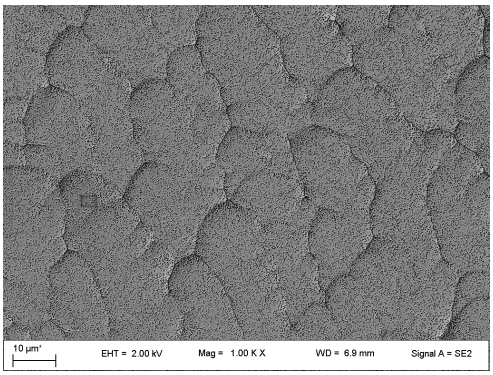

(a) T603: SEM image at μm-scale

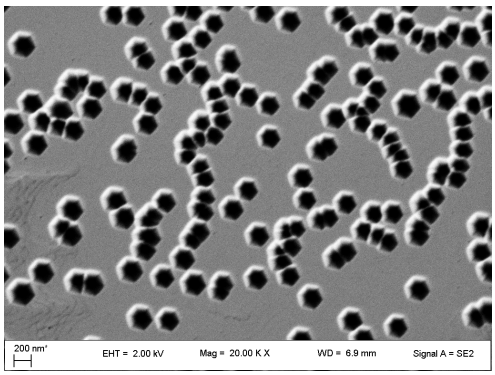

(b) T603: SEM image at nm-scale

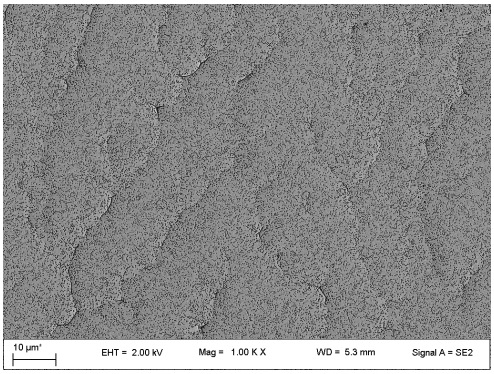

(c) T604: SEM image at μm-scale

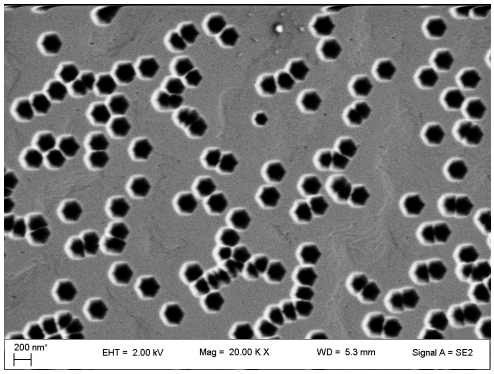

(d) T604: SEM image at nm-scale

Figure 68: SEM measurements on Series 6 structures with $100\mu m \times 100\mu m$ and $5\mu m \times 5\mu m$ windows, respectively.

discrepancy between RSM images of a standard AlGaN/GaN structure and one comprising a BGaN BB. The vertical alignment of the GaN and AlGaN related areas proves that layers are fully strained on bulk GaN.

Moreover, $\omega - 2\theta$ scans of structures T603 and T604, presented in Figs. 69(a) and 69(c), both exhibit well defined interference fringes corresponding to a good structural quality of the growth. Again, the introduction of BGaN did not impact results.

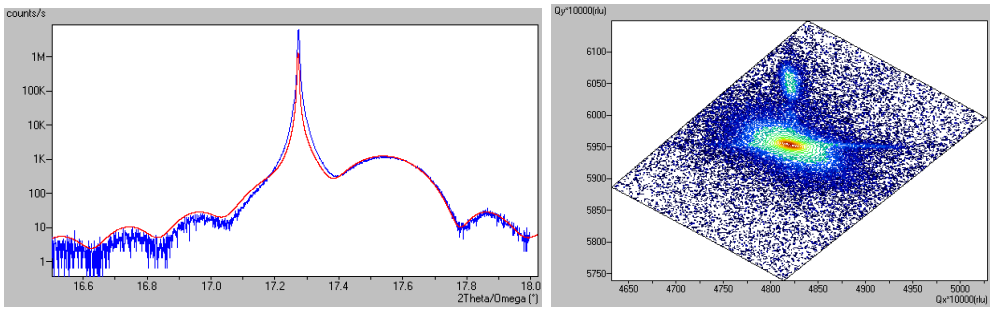

(a) XRD image of sample T603 (b) RSM image of sample T603

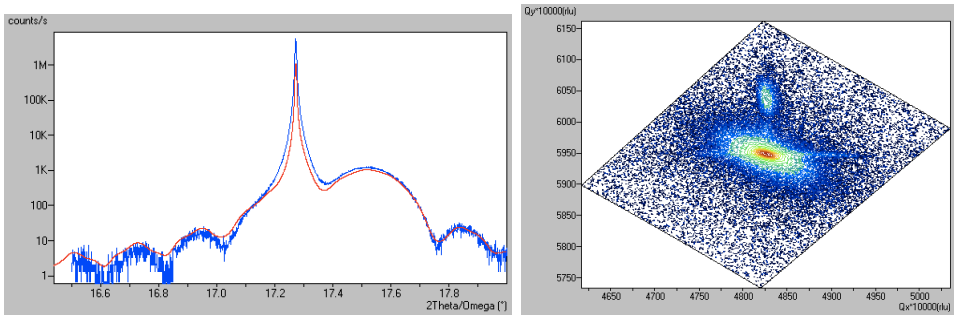

(c) XRD image of sample T604 (d) RSM image of sample T604

Figure 69: XRD and RSM measurements on Series 6 structures.

Nevertheless, the BGaN layer was not detected by XRD measurements. Considering the very low the boron-incorporation, its detection must depend on a threshold thickness usually reached with typical thick layers (above 300 nm). In fact, electrical behavior can reveal the effect of a BGaN CL or BB compared to a standard structure. To assess more deeply the existence of BGaN layers, we have to use more advanced characterization tools such as TEM.

7.2.3 BGaN as a compensation layer

Study on growth of standard AlGaN/GaN structures showed how detrimental impurities at the regrowth interface were for a proper HEMT operation. Another interesting way to exploit BGaN would be to have it right at the regrowth interface. In addition, we believe that results exposed earlier on the highly resistive behavior of BGaN advocate for the hypothesis that boron compensates impurities when incorporated in GaN. Consequently, a thin layer of BGaN can be introduced during growth, right on the template to prevent the formation of a unwanted parasitic channel.

Structures grown are depicted in Appendix A as the first part of batch Series 5 (see Fig. 78). The reference structure is the standard AlGaN/GaN HEMT structure T572 as it does not comprise any boron. The two other structures are based on the same design but with the introduction of a BGaN thin layer right at the regrowth interface. Thus, both have a compensating layer with a 1% of boron-content with either a 2 or 4 nm thickness (for T568 and T571, respectively).

Table 7 summarizes results obtained with mercury probe CV measurements. All structures possess a 25 % Al-content in barrier layer. The standard structure, T572, exhibits a HEMT behavior with results a little below, though, best performances reported in the previous chapter. Nevertheless, a slight improvement of the carrier density and, mainly, of the sheet resistance can be seen with structure T568 in comparison with the standard structure. This could be attributed to the effect of the BGaN CL, but results are too close to conclude.

Conversely, figures of merit for structure T571 unveil the deterioration of 2DEG with a lower pinch-off voltage and, most notably, a much higher sheet resistance. The confinement is worsen most probably because of degraded structural quality at the AlGaN/GaN interface. This conclusion is consistent with our previous studies establishing a critical thickness beyond which BGaN layers engender a 3-dimensional growth. Even though the growth remains 2-dimensional according to AFM results, we

Table 7: Data derived from CV measurements using mercury probes and comparing the standard AlGaN/GaN structure T572 to structures with a BGaN compensating layers (all BB/CL layers comprise 1% of boron).

	no boron	with boron	
designation	T572	T568	T571
% Al	25 %	25 %	25 %
CL thickness (nm)	-	2	4
Vp (V)	-1.5	-1.8	-1.2
$n_s \times 10^{12}$ cm^{-2}	3.6	4.3	3.6
R_{sh} (Ω/sq)	1500	1180	3130

can infer that a thick BGaN layer is not suitable for the growth of different materials on top of it.

7.2.4 BGaN as back-barrier

The second employ of a thin BGaN layer is as a BB within an AlGaN/GaN HEMT structure. The BGaN thin layer is now positioned inside the GaN buffer at a carefully chosen distance from the channel (i.e. AlGaN/GaN interface). As presented in Section 5.4.4, this relies on two distinctive effects: (i) the creation of electrostatic barrier through a discontinuity of the conduction band and, (ii) the introduction of a resistive barrier because of BGaN singular properties (see Section 7.1.2).

We performed electrical measurements to assess BGaN BB effect. Table 8 summarizes results obtained with mercury probe CV measurements for Series 5. Best performances are achieved with structure T575 and T577 with BGaN BB with 1 % of boron at a distance from the channel of 10 and 40 nm, respectively. Compared to the standard structure T572, the carrier density is higher in both cases and sheet resistance is notably reduced for T575. Besides, analysis of CV profiles, in terms of electrical behavior, show that the structure T577 exhibits a more defined pinch-off even at high frequency. However, no improvement can be seen with structures T574 and T576, corresponding to a distance from the channel of 20 nm, with thicknesses

Table 8: Data derived from CV measurements using mercury probes and comparing the standard AlGaN/GaN structure T572 to structures with a BGaN back-barriers in Series 5 (all BB layers comprise 1% of boron).

	no boron	with boron			
designation	T572	T574	T575	T576	T577
% Al	25 %	24 %	25,5 %	26 %	24,3 %
BB thickness (nm)	-	2	1	1	1
BB-channel distance (nm)	-	20	10	20	40
Vp (V)	-1.5	-1.5	-1.8	-1.2	-2
$n_s \times 10^{12}\,cm^{-2}$	3.6	3.6	4.3	2.9	4.8
R_{sh} (Ω/sq)	1500	1500	1270	2070	1550

of the BGaN BB of either 1 or 2 nm, respectively.

With respect to results above, we decided to increase the Al-content in the AlGaN barrier to improve performances and obtain a higher carrier density for Series 6. In addition, we chose to place the BGaN BB at a distance from the channel of 40 nm as structure T577. As seen from results displayed in Table 9, we can notice that the increase of the Al-content in the barrier (except T602) clearly translates into a much higher carrier density compared to previous series (at least 20 %). This result is echoed by an evident augmentation, in absolute values, of pinch-off voltages (2.5-3 V compared to 1.2-2 V for the previous series).

Most importantly, a significant enhancement of the figures of merit can be noticed for structures T604 and T605 in comparison with T603. The carrier density increases up to $7.26\times10^{12}\,cm^{-2}$ and the sheet resistance goes down to 699 Ω/sq, which brings us closer to state-of-the-art results (typically $1\times10^{13}\,cm^{-2}$ and 400 Ω/sq). The effect of the BGaN BB is demonstrated in this series through an amelioration of the confinement of carriers and a reduced leakage.

7.2.5 TEM measurements

To assess the existence of a BGaN layer within the GaN buffer, we analyzed precisely the composition of structure T574 and T575, both comprising a BGaN BB at a

Table 9: Data derived from CV measurements using mercury probes and comparing the standard AlGaN/GaN structures T602 and T603 to structures with a BGaN back-barriers in Series 6 (all BB layers comprise 1% of boron).

	no boron		with boron	
designation	T602	T603	T604	T605
% Al	22,5 %	31,7 %	30 %	30 %
BB thickness (nm)	-	-	1	2
BB-channel distance (nm)	-	-	40	40
Vp (V)	-2	-2.5	-3	-2.8
$n_s \times 10^{12}\,cm^{-2}$	4.84	6.05	7.26	6.8
R_{sh} (Ω/sq)	1700	1370	699	970

distance from the channel of 10 or 20 nm, respectively.

We therefore performed STEM-HAADF measurements after a FIB preparation of the samples along with the required protection of the surface. Figure 70 shows TEM images obtained for structures T574 and T575. For both cases, the theoretical distance from the channel of the BGaN BB has been inserted (in red). The light grey material corresponds to the GaN buffer, and dark grey one to AlGaN. The interface is abrupt which is a prerequisite for good HEMT performances. However, no defined BGaN/GaN interface is distinguishable. We can infer that BGaN layers are too thin, and possess a too low boron-content to be seen. In addition, we suspect a delay in boron incorporation during the growth that impedes the correct determination of the location of the BGaN layer.

As a consequence, it is difficult to distinctly display the presence of BGaN in our structure. Further investigations should be done with STEM-HAADF by adding in our structures marker layers to precisely localize the positioning of the BGaN layer and identify any growth delay occurring in our chamber.

Nonetheless, electrical performances reported above allow to discriminate standard structures from others comprising a BGaN layer. Even though the effect is moderate in Series 5, it is more obvious with Series 6. In order to alleviate doubts

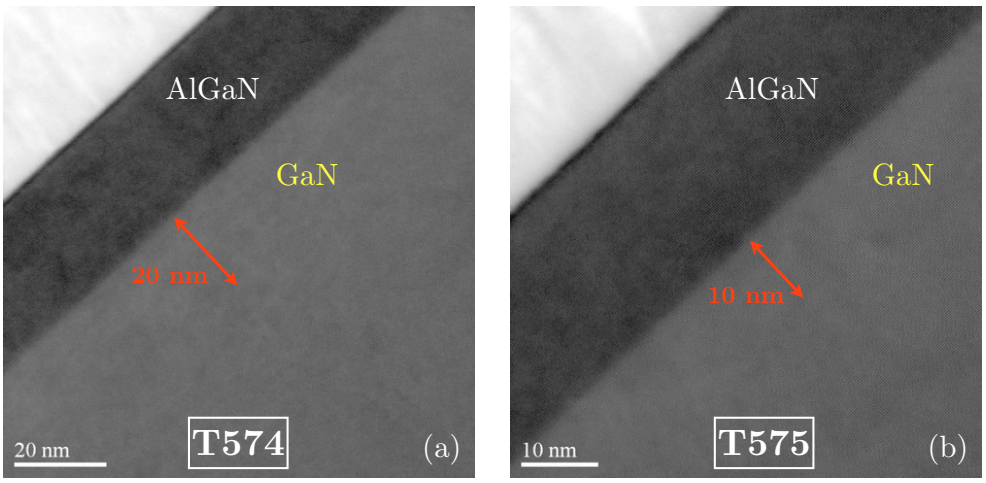

Figure 70: STEM-HAADF measurements on structures T574 and T575 comprising a BGaN BB at a distance from the channel of 10 or 20 nm, respectively. The theoretical distance from the channel of the BGaN BB is displayed in red. As the BGaN BB are too thin, they are not visible since the contrast limit is reached.

from previous conclusions, a supplementary campaign was carried out with Series 7.

7.3 Device results

Valuable information was derived from structural morphological analysis as well as measurements with using mercury probes. The preliminary results showed no distinctive degradation due to the introduction of BGaN but a significant improvement of transport properties compared to standard structures. However, accurate performances of a HEMT are assessed only when actual contacts are manufactured.

As a results, as we reached a growth *maturity* with a device quality because of our prior study on standard HEMT, Series 5 and 6 underwent state-of-the-art processing at our partner lab IEMN for further measurements. These latter have been processed and characterized and an exhaustive study can be found in M. Boucherit's thesis [115]. Results obtained are in good agreement with the preliminary analysis performed with mercury probe measurements. This technique, that is fast and easily carried out without any contact, exhibited similar trends and lead to analogous conclusions, hence supporting its reliability. The improvement of performance was again noticed with the introduction of a BGaN BB.

A seventh series of structures were grown as Series 7 (see Fig. 81 of Appendix A), also focusing on BGaN BB.

7.3.1 Series 7 - Introduction of a GaN cap layer

For Series 7, structure T744 and T745 are the standard structures with 26 % and 30 % of Al in the barrier, respectively, as a basis of comparison with other structures as well as other series. In addition, structure T747 comprises a BGaN BB for which the distance from the channel was chosen to be at 40 nm as best results were obtained for this design.

The issue related to a parallel conduction because of impurities at the regrowth interface was already reviewed earlier. Yet, measurements performed on previous Series 5 and 6 showed a similar behavior, to a lesser extent, despite no detection

of these impurities at the depth corresponding to the regrowth interface. Thus, we suspected a possible conduction through surface traps. It is well known that surfaces traps, embodied by charges located on top of the barrier layer, are detrimental to microwave performances. As illustrated in Fig. 71, during normal operation, i.e. when the gate is biased negatively and the drain positively, electrons located in the gate metal can reach deep donors existing on the surface by tunnel effect. Hence, they can get trapped, and the negative differential charging of deep donors leads to a counterpart reduction of electron density in the 2DEG, i.e. of the carrier density. In addition, the very same negative charge can accumulate close to the drain and create a *virtual gate* with a negative polarization that will deplete even more the 2DEG.

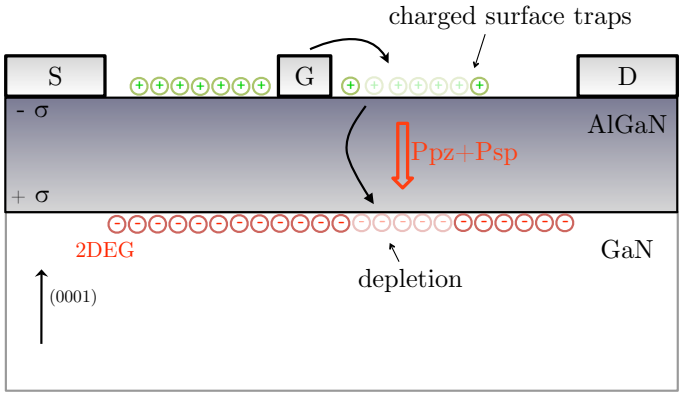

Figure 71: Schematic principle of surface traps formation.

Apart from surface passivation that is normal work during our process, we decided to add GaN caps to our structures [116, 117], consisting in a GaN layer grown on top of the barrier to mitigate the surface trap effect. Thus, within Series 7, structures T476 and T478 follow the same design as structures T475 and T477, respectively, but with the introduction of a 2 nm GaN cap layer.

7.3.2 Processing of devices

We processed our structures with our partner at IEMN to obtain an actual HEMT device. For precision below the micrometer, electron beam beam lithography was

employed. Within the scope of the project, several standard AlGaN/GaN structures from previous series were used for development. For Series 5, 6 and 7, the process steps were executed as follows:

Deposition of alignment marks: these marks are required to find one's way onto the surface of the structure, a Mo/Ni/Mo (20/40/70 nm) metallic deposition was selected to withstand high temperature thermal annealing.

Deposition of ohmic contacts and subsequent thermal annealing: so as to obtain sharp sides to avoid any source-gate short-circuit, ohmic contacts were defined using electron beam lithography, Transmission Length Method (TLM) contacts were manufactured this way.

Isolation by He^+ implantation: this step is necessary to isolate one HEMT to another within the same structure; for that, the technology was developed for nitrides with implantation of He^+ ions at different energies and doses with a prior masking of active areas with appropriate resins.

Deposition of the gate (with possible thermal annealing): regarding the metal deposition for the Schottky contact, Au/Ni/III-N or Au/Mo/Ni/III-N were employed as Ni was shown to be a better anchor layer on the AlGaN barrier. Moreover, to optimize microwave performances, state-of-the-art T-shaped gates were fabricated with a foot print from 50 to 500 nm, as illustrated in Fig. 72.

Surface passivation with an insulating dielectric: a dielectric bilayer SiO_2/Si_3N_4 (100/50 nm) was deposited by PECVD at 340° C to mitigate degradation of performances at high frequency operation.

As depicted in Fig. 72, V-defects are again visible on the structure. The choice of sub-micrometer gate length , despite manufacturing difficulties encountered due to V-defects, is because of high frequency performances achievable. This technique

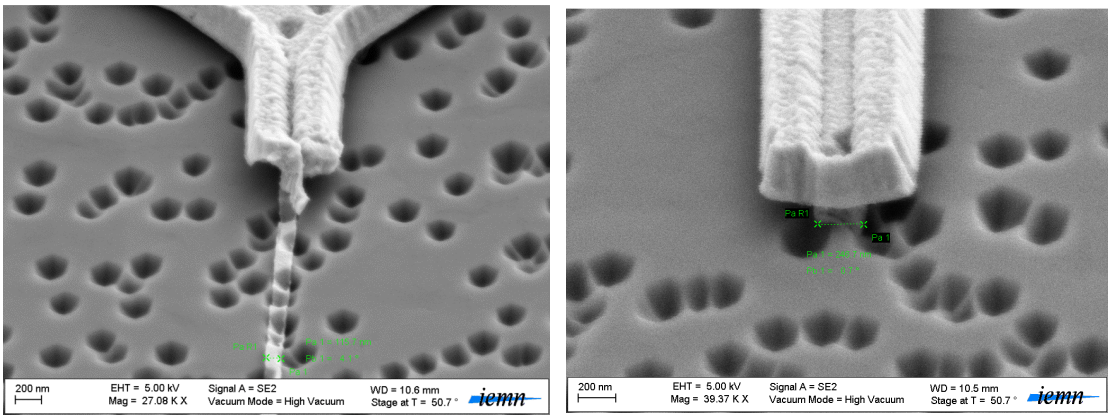

(a) 100 nm foot print (b) 250 nm foot print

Figure 72: FIB cross-sectional view of T-shaped gates manufactured with foot print size of (a) 100 nm and (b) 250 nm.

was developed originally on III-V semiconductors as GaAs [118] to accomplish high gain and low noise figure. A smaller gate foot print allows to obtain a reduced gate capacitance but leads to a higher gate resistance. We can circumvent this by using a *mushroom* shaped contact, which comprises a nanometer-scale gate length and a large upper-side cross-section area. For nitrides, a tri-layer resin combination technique is usually used to achieve this [119].

7.3.3 Characterization and preliminary results

We processed all structures according to the protocol above and Hall measurements were used to analyze transport properties. Experiments were performed under illumination and values displayed are averaged over several areas on a same sample (typically 13 points).

Table 10 presents results for Series 5. The process of structure T572 failed and no standard structure, belonging to the same batch, can be used for comparison. As mentioned above, we find quite similar trends than mercury probes measurements reported in Section 7.2.4. Nonetheless, sheet resistance values (R_{sh}) are significantly worsen and sheet carrier densities a little higher. As structure T575 exhibits best results, a preliminary conclusion highlights a preferable distance from the channel

Table 10: Data derived from Hall measurements, under illumination, on processed structures of Series 5 (all BB layers comprise 1% of boron).

designation	T574	T575	T576	T577
% Al	24 %	25,5 %	26 %	24,3 %
BB thickness (nm)	2	1	1	1
BB-channel distance (nm)	20	10	20	40
n_s $\times 10^{12}$ cm^{-2}	5.90	6.03	5.58	4.23
R_{sh} (Ω/sq)	1805	1076	1794	2964
μ_n (cm^2/V.s)	590	973	632	519

of 10 nm for the BGaN BB with a thickness limited to 1 nm. A closer BB to the 2DEG helps confinement by reducing the span of the triangular-like quantum well. In addition, moving to a 2 nm thickness induced manifestly a 2D/3D growth impeding structural quality of layers above, especially the AlGaN/GaN interface.

Nevertheless, improvements brought to our growths led to much better results. Our choice to keep the BGaN BB at a distance of 40 nm from the channel on ongoing series was motivated by preliminary results. Though, it was also preferred so as to have a large enough separation between the BGaN BB and the channel to ensure a good AlGaN/GaN interfacial quality. Transport properties of Series 6 are displayed in Table 11. Evidently, the increase of the Al-content in the barrier led to expected effects with higher carrier densities in the 2DEG. As all figures are improved, this allows us to clearly see improvements brought by the introduction of a BGaN BB in structures T604 and T605. The confinement of carriers is notably visible through a reduced sheet resistance and an increased mobility. Once more, a thickness of 2 nm of the BGaN BB seemingly degrades performances because of a lower structural quality.

As reviewed in Section 7.3.1, Series 7 focuses on 1 nm thick BGaN BB at a distance from the channel of 40 nm and introduces the GaN cap layer. Table 12 summarizes

Table 11: Data derived from Hall measurements, under illumination, on processed structures of Series 6 (all BB layers comprise 1% of boron).

	no boron		with boron - BB	
designation	T602	T603	T604	T605
% Al	22,5 %	31,7 %	30 %	30 %
BB thickness (nm)	-	-	1	2
BB-channel distance (nm)	-	-	40	40
$n_s \times 10^{12}$ cm^{-2}	4.05	6.93	7.26	7.71
R_{sh} (Ω/sq)	2018	1033	816	966
μ_n (cm^2/V.s)	770	875	1060	843

results obtained. It should be noted that structure T744 is not displayed as not relevant for comparison purposes (due to a lower Al-content). The improvements seen on growths of the previous series are here corroborated. To that, one should add that the standard structure T745 exhibits a better sheet resistance than T603 which has the same design. The introduction of a GaN cap layer to mitigate surface traps effect did ameliorate transport properties. Moreover, the highest performances seen so far correspond to structure T747 and are attributed to the BGaN BB with respect to T745. However, the GaN cap layer combined to the BGaN BB, as illustrated in structure T748, does not meet expectations. A possible explanation to this phenomenon lies in the structural quality as before. The increase of the thickness, and mainly the addition of different material layers by heteroepitaxy, bring out structural defects due to the BGaN layer.

Thus, measurements on HEMT devices allow to expose the improvement of transport properties of the 2DEG by the introduction of a BGaN BB within conventional AlGaN/GaN structures. To further support these interpretations, we performed DC and AC current-voltage measurements to evaluate performances for microwave operation.

Table 12: Data derived from Hall measurements, under illumination, on processed structures of Series 7 (all BB layers comprise 1% of boron).

	no boron		with boron - BB	
designation	T745	T746	T747	T748
BB thickness (nm)	-	-	1	1
BB-channel distance (nm)	-	-	40	40
GaN cap thickness (nm)	-	2	-	2
$n_s \times 10^{12}$ cm^{-2}	7.50	8.98	10	7.34
R_{sh} (Ω/sq)	851	643	603	1024
μ_n (cm^2/V.s)	906	1034	1097	843

7.3.4 Evidence of the effect of BGaN layers on microwave performance of conventional AlGaN/GaN HEMT

As seen in the previous Section, structure T748 of Series 7, comprising both a BGaN BB and a cap layer, did not exhibit satisfying results. We therefore focus our following study on comparing structures T745 and T747, both based on the same AlGaN/GaN standard design, but with a BGaN BB inserted in the GaN buffer of the last one.

First results of DC current-voltage characteristics between two electrodes deposited on the GaN buffer layer with and without a $B_{0.01}Ga_{0.99}N$ BB are shown in Fig. 73. We observe that the insertion of this ultra-thin BGaN BB in the buffer layer reduces the leakage current of an order of magnitude for a large electric field range. To further evaluate the influence of BGaN, we fabricated a set of epitaxial structures with and without a BGaN BB ultra-thin layer. We employed commercial GaN templates composed of an AlN/GaN nucleation layer on sapphire substrate and a 3.5 μm undoped GaN buffer. For the first structure presented here, the epitaxial growth started with a 400 nm GaN layer followed by a 1 nm $B_{0.01}Ga_{0.99}N$ BB, a 40 nm undoped GaN channel, and a 21 nm undoped $Al_{0.3}Ga_{0.7}N$ barrier layer (tAlGaN). The second structure was grown as a reference with the same epitaxy but with no BGaN BB. Surface roughness obtained by Atomic Force Microscopy exhibited similar values for both structures suggesting no deterioration with the introduction of

the BGaN layer. For device fabrication, the source and drain were defined by e-beam lithography. The metallization used was based on evaporated Ti/Al/Mo/Au (12/200/40/100nm) multilayer followed by a rapid thermal annealing at 900°C for 30 seconds under nitrogen atmosphere. The device isolation is obtained by He^+ ions multiple implantations. The T-shaped gates were defined by e-beam lithography with a tri-layer resist stack and the metallization used was based on evaporated Pt/Mo/Au (25/25/200 nm). Devices were passivated with a SiO_2/Si_3N_4 (100/50nm) bi-layer dielectric deposited by plasma-enhanced chemical vapor deposition at 340°C [120].

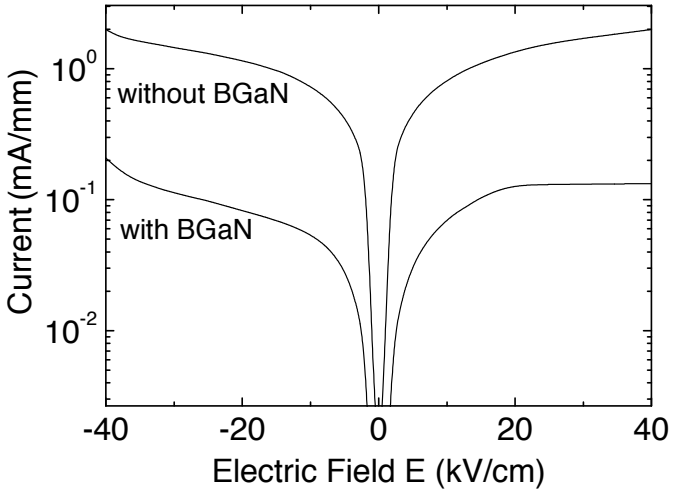

Figure 73: Current-Electric Field characteristics between two electrodes performed on GaN buffer layer without and with BGaN BB (GaN (40nm)/$B_{0.01}Ga_{0.99}N$ (1nm)/GaN buffer layer).

Hall measurements performed on the HEMT structures without and with a BGaN BB exhibited sheet carrier densities of $7.5\times10^{12}\,cm^{-2}$ and $1.03\times10^{13}\,cm^{-2}$, electron mobilities of 906 $cm^2.V^{-1}.s^{-1}$ and 1230 $cm^2.V^{-1}.s^{-1}$, and sheet square resistance values of 851 Ω and 604 Ω at room temperature, respectively. These results clearly establish a notable improvement of the carrier confinement with the introduction of the BGaN BB. As the electrostatic barrier of 1 nm is relatively small, this improvement can be attributed to the resistivity of the BGaN BB, probably due to the

decrease of the residual doping and the improvement of the material quality. This was confirmed by SIMS results obtained by H. Kim *et al.* [121] showing that the oxygen concentration in samples increases with the aluminum rate during the growth of AlGaN barrier layer, but drastically decreases when boron is incorporated.

For the HEMT including the BGaN BB, transmission line measurements showed a contact resistance of 0.56 Ω.mm, a specific contact resistivity of $6.1 \times 10^{-6}\,\Omega.\mathrm{cm}^2$, and a sheet square resistance of 635 Ω at room temperature. A barrier height of 1.27 eV associated with an ideality factor of η=1.2 was deduced from the forward characteristics of the Schottky contact. The reverse gate leakage was about 20 μA/mm at -10 V gate source bias. The breakdown voltage in transistor configuration was also greatly enhanced up to 190 V at pinch-off against 42V for the device without BGaN BB for a gate-drain distance L_{GD}=1μm. Under three terminal voltage measurement, I_{DS} is improved by around two orders of magnitude at pinch-off from 4×10^{-3} A/mm to 7×10^{-5} A/mm. Regarding gate current, the gate leakage current drops of one order of magnitude (4×10^{-7} A/mm) with the BGaN BB at V_{GS}=-6V and V_{DS}=10V.

All DC and small signal measurements were carried out with a gate width of 2×100 μm, a drain-gate spacing of 1 μm, a gate-source spacing of 0.5 μm, and a gate length (L_G) of 250 nm. The DC characteristics were measured with programmable alimentation multi-slots like *HP4142* or *Agilent 5270*. DC measurement performed on the HEMT with BGaN exhibited a maximum drain current density of 642 mA/mm at V_{GS}=0 V with an extrinsic transconductance (g_m) of about 137 mS/mm and for a gate bias V_{GS}=-3 V and for a drain bias V_{DS}=15 V. Small signal microwave measurements were also carried out on this transistor under probes. The calibration procedure was performed on wafer using a TRM method with a 40 GHz Power Network Analyzer type *E8363B*. The S-parameters are measured in the 25 MHz to 40 GHz frequency range. The extrinsic current gain cut-off frequency f_t and maximum oscillation frequency f_{max} values are 30 GHz and 55 GHz respectively at V_{DS}=15 V, V_{GS}=-4 V for

a structure including a BGaN BB, but only 9.7 GHz and 36 GHz for the reference structure without BGaN.

Pulsed measurements were carried out for different quiescent bias points to study the trap response to an applied electrical field: (V_{DS0}=0 V, V_{GS0}=0 V) giving the reference characteristics and (V_{DS0}=0 V, V_{GS0}=-8 V) showing the gate lag effect and (V_{DS0}=15 V, V_{GS0}=-8 V) showing the drain lag effect. The pulse duration was 400 ns with a duty cycle of 0.4%. Figure 74 shows an example of pulsed $I_{DS}(V_{GS},V_{DS})$ characteristics for two samples with and without a BGaN BB. In this case, the trapping phenomenon is reduced for the sample with BGaN BB, which exhibits excellent behavior at high frequency. At V_{DS0}=4 V, the current drop is 25.8% and 6.2% due to the gate and drain lag effects respectively.

The extrinsic current gain cut-off frequency response can be defined by:

$$f_t = v_{eff} \times (2\pi\ L_{G,eff})^{-1}, \tag{54}$$

where v_{eff} is the effective electron velocity and $L_{G,eff}$ is the effective gate length, with $L_{G,eff} = L_G + L_{GF}$ where L_{GF} is the fringing-field gate length. The electron velocities v_{e-eff} deduced from the extrinsic device measurement give 0.81×10^7 cm/s and 0.45×10^7 cm/s with and without a BGaN back-barrier, respectively. L_{GF} increases from 179 nm to 488 nm for structures with and without BGaN BB. This result shows that the presence of the BGaN BB layer significantly reduces the surface density of states compared to the reference structure due to a drop of O_N acting as N doping. These values are determined without de-embedding of the parasitic elements and must be compared with 1.24×10^7 cm/s from Jessen *et al.* [122], which demonstrated sheet resistances between 25 kΩ and 304 MΩ for bulk BGaN material with 400 nm thickness. But in this case, the growth was quasi-3D, which is incompatible with a transistor epitaxy. In our case, by including a 1 nm with 1% BGaN BB in the GaN buffer layer, the growth remains 2D and the sheet resistance increases from 25 kΩ up to 270 kΩ. These results show that BGaN BB improve the electrons confinement in 2DEG and

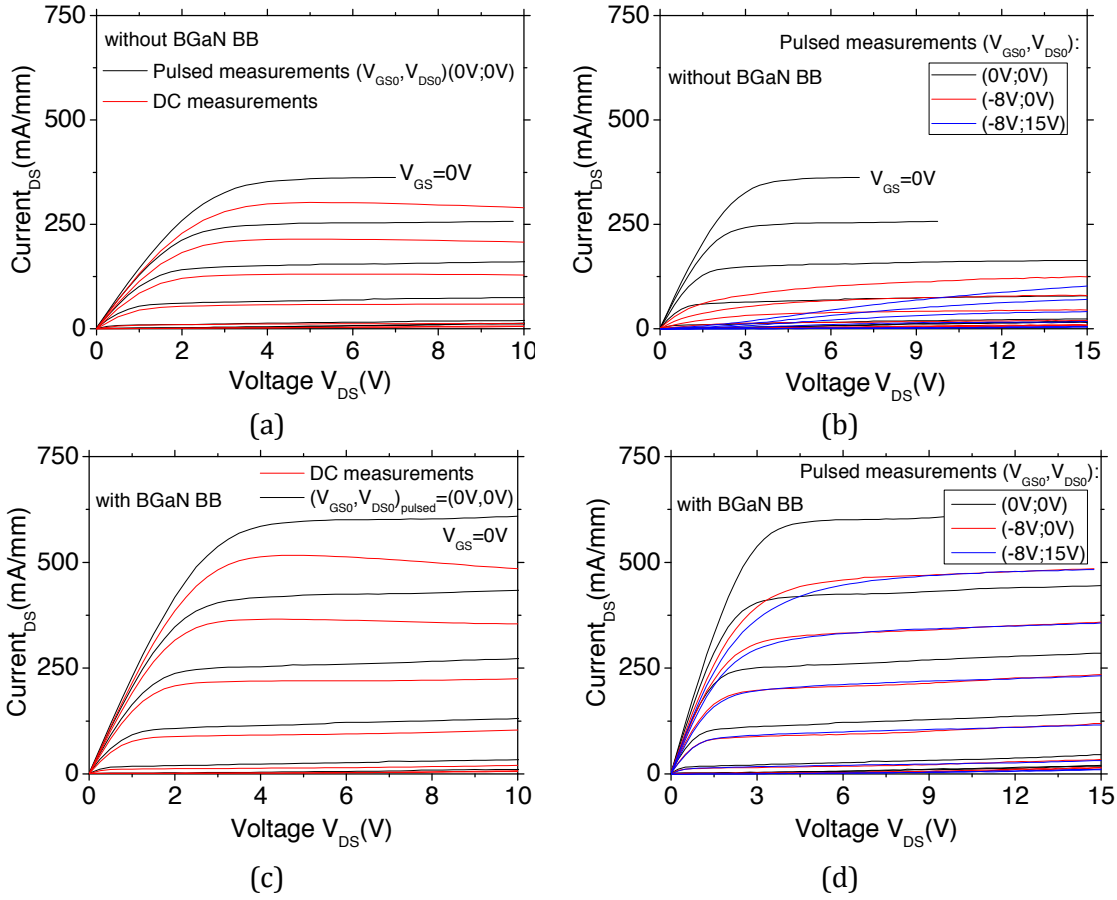

Figure 74: $I_{DS}(V_{GS})$ measurements on DC and pulsed regimes on a device without (a,b) and with (c,d) an ultra-thin BGaN BB barrier. (a,c) DC measurements and pulsed with quiescent point at (V_{GS},V_{DS}) : (0 V, 0 V); (b,d) DC measurements and pulsed with quiescent point at ((V_{GS},V_{DS}): (0 V, 0 V), (-8 V, 0 V), and (-8 V, 15 V).

could reduce both the oxygen impurities in the heterostructure and the structural defects in the GaN channel. The difference between our results and those of Jessen *et al.* [122] is due to the strong short-channel effects and the material quality (indeed, the $f_t \times L_G$ product is 7.5 (GHz$\times\mu$m) and the L_G/tAlGaN aspect ratio is about 12). An electrostatic analysis demonstrates that the leakage of electrons is reduced with the BGaN BB because of its high resistivity. Consequently, charge concentration in the 2DEG is more confined in the quantum well and, therefore, the density and the mobility are greater.

CHAPTER VIII

CONCLUSION

This final chapter summarizes our conclusions and future research.

8.1 Contribution

For advanced optoelectronics devices, the semiconductor industry has been driven by III-V materials whose superior physical properties and enhanced efficiency compared to silicon technology make them suitable for a continuously growing demand for higher performances. Nitride HEMTs exemplify this qualitative leap forward by offering unique power densities and operational efficiencies and a significantly improved compactness.

In this dissertation, we investigated the potential of BGaN material, through singular electrical and optical properties, and study their application for the amelioration of transport properties in conventional AlGaN/GaN HEMTs.

In Chapter 5, we developed the simulation of HEMT structures through a Schrödinger-Poisson solver. To extend this calculation to nitride semiconductors, we reviewed polarizations of materials of interest such as AlGaN or InGaN on bulk GaN, as it is the core phenomenon behind the filling of the 2DEG, and we eventually illustrated with examples of band structures calculated with our solver. In particular, we focused our attention on the effect of InGaN back-barriers on the confinement of carriers in conventional AlGaN/GaN HEMTs. We then showed how BGaN thin layers could serve the same purpose of limiting leakage in the buffer. To implement BGaN materials in our simulations, we examined key parameters, such as the bandgap and physical constants related to the polarization, and derived equations used for simulation. The simulation study performed from this provided evidence of the dual-purpose of

BGaN layers in GaN buffers of nitride HEMTs: they improve the confinement of the electrons in the 2DEG by creating an electrostatic barrier to electrons as well as a resistive layer as well, both effects preventing leakage in the buffer. Moreover, the growth of BGaN materials by MOCVD is done at a similar temperature than that of AlGaN and GaN materials. As a result, we expect higher structural and interfacial quality would be achieved, therefore improving the efficiency of the HEMT.

Chapter 6 introduced our experimental work and strategic growth of standard AlGaN/GaN HEMT structures. Despite V-defects appearance, morphological and structural analyses showed a good control of HEMT growth with low surface roughnesses and fully strained layers. As we used GaN templates for our samples, we brought adjustments to prevent the presence of impurities at the regrowth interface that are detrimental to performances. The study of subsequent campaigns allowed us to demonstrate the attainment of a device quality with a suitable reproducibility.

Chapter 7 built upon our simulations and our intent to determine the impact of BGaN layers on HEMT performances. We firstly detailed our research on thick BGaN layers, by means of electrical and optical analyses, in order to corroborate two key properties characterizing this novel material: its bandgap and its resistivity. Hall measurements supported results from our group that BGaN features a high resistivity for only a few percents of boron. In addition, we carried out photoluminescence experiments which agreed with the observation of a shift corresponding to a bandgap bowing of BGaN. We then studied results from several growth campaigns presenting designs for GaN based HEMTs with the introduction of BGaN back barrier layers. Eventually, we found that the use of ultra-thin BGaN back-barrier with a thickness of 1 nm and a boron content of 1% drastically improves the electron confinement in standard AlGaN/GaN HEMTs and the resistivity of GaN buffer layer as well. These improvements significantly enhance the DC and RF performances of the transistors. Thus, a thick layer of BGaN, with 1 to 5% boron content, creates an electrostatic and

resistive barrier to electrons between the channel including the 2DEG and the GaN buffer below. Compared to conventional AlGaN/GaN HEMTs, structures grown with BGaN back-barrier showed a significant improvement of static performances, transport properties, and trapping effects involving a limited current collapse in dynamic regime. A DC maximum current increase of 58.7% was observed.

This dual purpose of BGaN, being more suitable for MOCVD growth, shows that these innovative structures are very promising for high-power and high-frequency applications since an improved confinement of carriers can be obtained. As boron alloying in GaN layers significantly increases resistivity, BGaN can play a double-role as a back-barrier.

This research led to the publication of an article and the submission of a patent:

Dual-purpose bgan layers on performance of nitride-based high electron mobility transistors. V. Ravindran, M. Boucherit, A. Soltani, S. Gautier, T. Moudakir, J. Dickerson, P. L. Voss, M.-A. di Forte-Poisson, J.-C. D. Jaeger, and A. Ougazzaden. *Applied Physics Letters*, 100(24):243503, 2012.

Improvement of transport properties of HEMT transistors based on wide bandgap boron nitride semiconductors (III-B)-N. V. Ravindran, A. Ougazzaden, M.-A. di Forte-Poisson, A. Soltani, J.-C. D. Jaeger. Patent pending (reference n° 11 01167).

8.2 Perspectives

The following paragraphs highlight research guidance for future work related to this thesis.

8.2.1 Growth optimization

Our study of HEMT growth, performed for the first time in our lab, should be continued to find the most suitable parameters adapted to our growth chamber. Recent experiments carried out with hydrogen as a carrier gas showed remarkably good

quality with the absence of V-defects. Obtained structures devoid of V-defect could significantly ameliorate the quality of our structure, facilitate the process steps for device manufacturing and, hence, lead to better results.

It was shown that BGaN could be employed as a compensating layer at the re-growth interface of the template. Results obtained within the scope of this project were promising but concerned only a few structures. More experiments should be performed to optimize the growth conditions and preserve a 2-dimensional epitaxy prior to the GaN buffer growth.

While ensuring a device quality, our study regarding BGaN back-barriers should be completed to find: (i) the reasonable distance from the channel where it must be placed in a conventional AlGaN/GaN HEMT, and (ii) the optimal thickness of the layer. Hence, the elaboration of BGaN layers must be further improved as these characteristics are closely related to its improvement.

8.2.2 Choice of substrate

Results obtained with the introduction of boron-containing nitride materials are encouraging, but still need to be improved to compete with the state-of-the-art. Apart from growth optimizations, sapphire substrates used so far are not the most suitable choice for high frequency performance. Manufacturing devices on SiC substrates should definitely enhance behavior in pulsed regime.

In addition, most research nowadays are aimed at growing nitride structures on cheap silicon substrates. It would therefore seem wise to manufacture devices on silicon after a prior growth study of standard HEMT.

8.2.3 Characterization of BGaN

The existence of 1 or 2 nm thick BGaN layers in the buffer of our HEMT structures could not be clearly assessed by structural and microscopy analyses. X-ray measurements are not suitable to detect such thin layers with low boron incorporation.

Further TEM measurements should be performed but this time using markers such as AlGaN thin layers to precisely localized GaN/BGaN interfaces. This would also allow us to see if a incorporation delay occurs in our growth chamber. Within a single structure, a series of BGaN layer of increasing composition should be grown to observe any possible gradual composition of boron.

8.2.4 New designs

For the implementation of BGaN materials in simulations, further study could be done to know its fundamental parameters. Apart from polarization and lattice parameters, getting better knowledge of relevant properties such as the band offsets at BGaN/GaN interfaces is interesting to refine calculations. The conduction band offset has a direct impact on the interface barrier height, hence, on the influence of BGaN layers on the 2DEG carriers.

The solver used for this research allowed us to obtain band structures and derive hypothesis from them. As opposed to InGaN back-barriers, BGaN back-barriers' impact on improving the confinement could not be predicted simply by mean of an electrostatic analysis. The effect of a resistive layer such as BGaN could not be implemented and be part of the simulation to predict the level of its effect on preventing leakage of carriers. More advanced simulation tools could be used to take into account transport properties of the GaN buffer.

Finally, as explained previously, BGaN does not provide a spread-out electrostatic barrier to electrons because of its lattice parameter, which is smaller than that of GaN, in contrast with InGaN. Our group demonstrated the feasibility of the growth of the quaternary BInGaN [123]. By employing a BInGaN thin layer in the buffer of conventional AlGaN/GaN HEMTs, we could get both a resistive effect, already seen in BGaN, and a distinctive spread-out electrostatic barrier from InGaN. In Fig. 75, the orange area shows approximately the location of BInGaN in the bandgap vs

lattice parameter graph. If there is little boron alloying as in [123], we can reach alloys located on the right part of this area, i.e. for a lattice parameter larger than GaN.

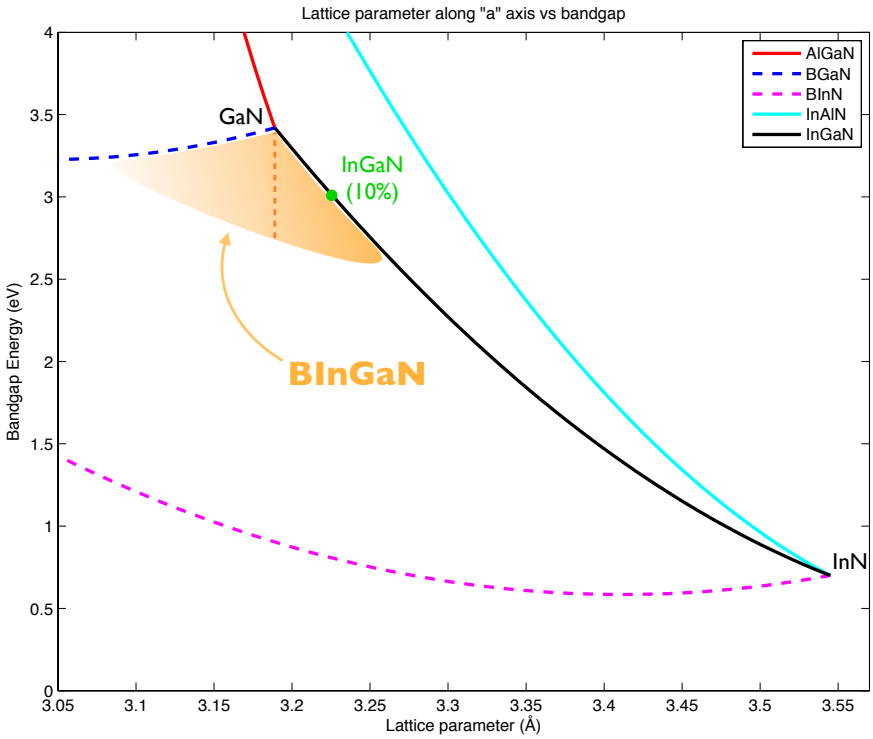

Figure 75: Bandgap versus lattice parameter - BInGaN.

A significant drawback will be the growth temperature of the BInGaN, which is, similarly to InGaN, quite low compared to GaN's growth temperature.

APPENDIX A

LIST OF HEMTS GROWN

Several series of structures were grown within the scope of this project. First series were aimed at obtaining a standard structure while subsequents ones explored new designs.

Series 1: The first series is shown in Figs. 51 and 52.

Series 2: The second series includes a standard AlGaN/GaN HEMT structure (T406) whereas others structures comprise an additional AlGaN layer at the regrowth interface.

Series 3: The third series is exclusively composed of standard AlGaN/GaN HEMT structures in order to reproduce and asses results achieved with structure T406.

Series 4: The fourth series is not depicted here as it consisted in one single AlN on GaN HEMT structure that did not exhibit a HEMT behavior.

Series 5: The fifth series includes one standard HEMT for comparison purpose along with 6 structures comprising a BGaN layers: 2 with a compensating layer and 4 with a back-barrier.

Series 6: The sixth series includes 2 standard HEMTs for comparison purpose along with 2 structures comprising a BGaN back-barrier. Apart from structure T602, the aim was to increase the Al content in the barrier up to 30%.

Series 7: The seventh series is very similar to the sixth series so as to assess results obtained. A standard structure and another comprising a BGaN back-barrier have been enhanced with an GaN cap layer.

T403	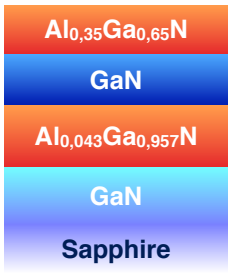	**Standard DH-HEMT** AlGaN (Al: 35%) 42 nm GaN 60 nm AlGaN (Al: 4.3%) 200 nm GaN bulk Sapphire
T406		**Standard HEMT** AlGaN (Al: 26%) 21 nm GaN 60 nm GaN (regrowth) 200 nm GaN bulk Sapphire
T407	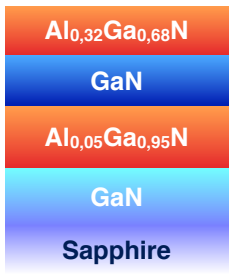	**Standard DH-HEMT** AlGaN (Al: 32%) 22 nm GaN 60 nm AlGaN (Al: 5%) 200 nm GaN bulk Sapphire
T408		**Standard DH-HEMT** AlGaN (Al: 31%) 22 nm GaN 60 nm AlGaN (Al: 7%) 200 nm GaN bulk Sapphire
T409		**Standard DH-HEMT** AlGaN (Al: 28%) 22 nm GaN 200 nm AlGaN (Al: 3.5%) 200 nm GaN bulk Sapphire

Figure 76: Structures of SERIES 2.

T445 T449 T450	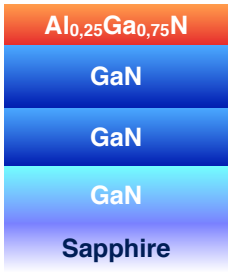	**Standard HEMT** AlGaN (Al: 25%) 21 nm GaN 60 nm GaN (regrowth) 200 nm GaN bulk Sapphire
T446 T447 T448		**Standard HEMT** AlGaN (Al: 33%) 21 nm GaN 60 nm GaN (regrowth) 200 nm GaN bulk Sapphire

Figure 77: Structures of SERIES 3.

T572		**Standard HEMT** AlGaN (Al: 26%) 21 nm GaN 61 nm GaN (regrowth) 200 nm GaN bulk Sapphire
T568	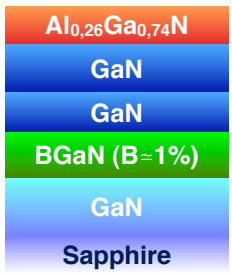	**BGaN compensating layer** AlGaN (Al: 26%) 21 nm GaN 60 nm GaN (regrowth) 200 nm BGaN (B: 1%) 2 nm GaN bulk Sapphire
T571	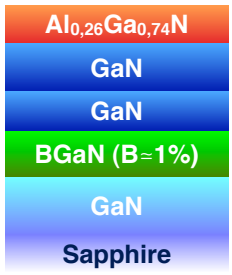	**BGaN compensating layer** AlGaN (Al: 26%) 21 nm GaN 60 nm GaN (regrowth) 200 nm BGaN (B: 1%) 4 nm GaN bulk Sapphire

Figure 78: Structures of SERIES 5 - First Part.

T574	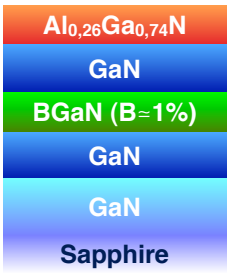	**BGaN back-barrier** AlGaN (Al: 26%) 21 nm GaN 20 nm BGaN (B: 1%) 2 nm GaN (regrowth) 239 nm GaN bulk Sapphire
T575	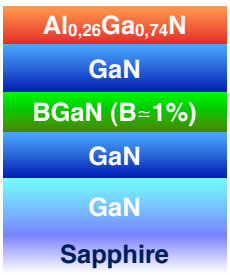	**BGaN back-barrier** AlGaN (Al: 26%) 21 nm GaN 10 nm BGaN (B: 1%) 1 nm GaN (regrowth) 250 nm GaN bulk Sapphire
T576	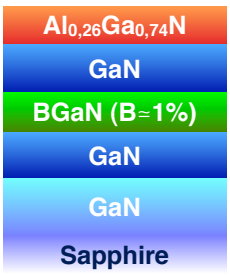	**BGaN back-barrier** AlGaN (Al: 26%) 21 nm GaN 20 nm BGaN (B: 1%) 1 nm GaN (regrowth) 250 nm GaN bulk Sapphire
T577	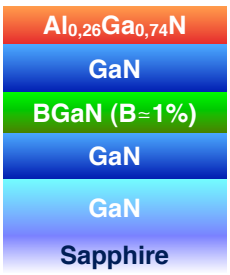	**BGaN back-barrier** AlGaN (Al: 26%) 21 nm GaN 40 nm BGaN (B: 1%) 1 nm GaN (regrowth) 220 nm GaN bulk Sapphire

Figure 79: Structures of SERIES 5 - Second Part.

T602	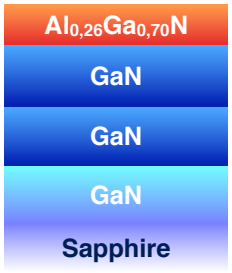	**Standard HEMT** AlGaN (Al: 26%) 21 nm GaN 61 nm GaN (regrowth) 200 nm GaN bulk Sapphire
T603		**Standard HEMT** AlGaN (Al: 30%) 21 nm GaN 61 nm GaN (regrowth) 200 nm GaN bulk Sapphire
T604	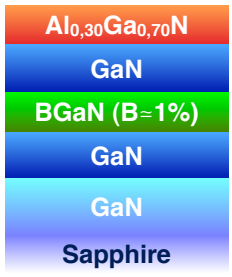	**BGaN back-barrier** AlGaN (Al: 30%) 21 nm GaN 40 nm BGaN (B: 1%) 1 nm GaN (regrowth) 220 nm GaN bulk Sapphire
T605	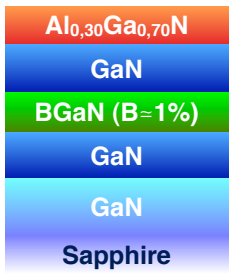	**BGaN back-barrier** AlGaN (Al: 30%) 21 nm GaN 40 nm BGaN (B: 1%) 2 nm GaN (regrowth) 220 nm GaN bulk Sapphire

Figure 80: Structures of SERIES 6.

T744	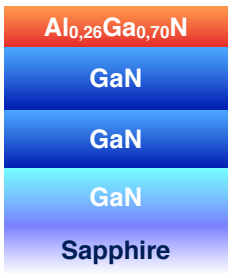	**Standard HEMT** AlGaN (Al: 26%) 21 nm GaN 61 nm GaN (regrowth) 200 nm GaN bulk Sapphire
T745		**Standard HEMT** AlGaN (Al: 30%) 21 nm GaN 61 nm GaN (regrowth) 200 nm GaN bulk Sapphire
T746		**Standard HEMT with cap** GaN (cap) 2 nm AlGaN (Al: 30%) 21 nm GaN 61 nm GaN (regrowth) 200 nm GaN bulk Sapphire
T747	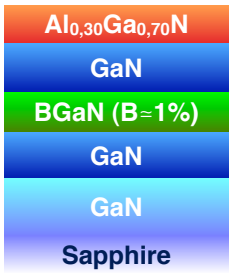	**BGaN back-barrier** AlGaN (Al: 30%) 21 nm GaN 40 nm BGaN (B: 1%) 1 nm GaN (regrowth) 220 nm GaN bulk Sapphire
T748	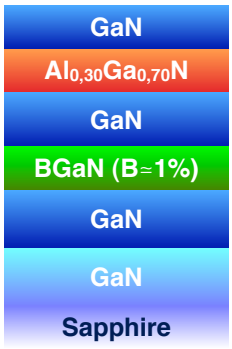	**BGaN back-barrier** GaN (cap) 2 nm AlGaN (Al: 30%) 21 nm GaN 40 nm BGaN (B: 1%) 1 nm GaN (regrowth) 220 nm GaN bulk Sapphire

Figure 81: Structures of SERIES 7.

APPENDIX B

AB INITIO CALCULATIONS PERFORMED ON NITRIDE COMPOUNDS

This Appendix presents *ab initio* calculations performed on GaN, AlN and BN by our partner from the LEM3 lab (or *Laboratoire d'étude des microstructures et de mécanique des matériaux*) at Metz, France. Simulations were performed using the projector augmented-wave (PAW) potentials method with either a local-density approximation (LDA) or a generalized gradient approximations (GGA). Data are compared to results reported by Shimada *et. al.* [17], Karch *et. al.* [18] and Kim *et. al.* [19]. Relevant elastic constants, Born effective charges and piezoelectric constants are reported for each material.

(Gpa)	$C_{11}+C_{12}$	$C_{11}-C_{12}$	C_{11}	C_{12}	C_{13}	C_{33}	C_{55}	C_{66}	B
GaN (PAW LDA)	513	233	373	140	105	411	97	116	206
GaN (PAW GGA)	448	216	332	116	85	364	91	108	178
Shimada (with corrections)			350	140	104	376	101	115	197
Shimada (without corrections)			420	110	66	448	119	156	197
Kim (FP-LMTO LDA)			396	144	100	392	91	126	207

	a (Å)	c (Å)	c/a	u	Zxx(Ga)	Zyy(Ga)	Zzz(Ga)	Z*(Ga)	Zxx(N)	Zyy(N)	Zzz(N)	Z*(N)
GaN (PAW LDA)	3,1263	5,1376	1,6433	0,3767	2,62	2,50	2,71	2,61	-2,62	-2,51	-2,72	-2,61
GaN (PAW GAA)	3,2124	5,2432	1,6322	0,3748	2,54	2,57	2,76	2,62	-2,56	-2,58	-2,77	-2,64
Karch	3,1430	5,1105	1,6260	0,3770	2,60	2,60	2,74	2,64				
Shimada	3,2100	5,2370	1,6315	0,3762			2,74					
Kim	3,1700	5,1300	1,6200	0,3790								

PIEZOELECTRIC TENSOR for field in x, y, z	(C/m^2)	GaN PAW LDA				
	XX	YY	ZZ	XY	YZ	ZX
x	0,00000	0,00000	0,00000	0,00000	0,00000	0,52349
y	0,00000	0,00000	0,00000	0,00000	0,52354	0,00000
z	0,45186	0,45186	-0,92765	0,00000	0,00000	0,00000

PIEZOELECTRIC TENSOR for field in x, y, z	(C/m^2)	GaN PAW GGA				
	XX	YY	ZZ	XY	YZ	ZX
x	0,00000	0,00000	0,00000	0,00000	0,00000	0,48659
y	0,00000	0,00000	0,00000	0,00000	0,48658	0,00000
z	0,47576	0,47576	-0,97120	0,00000	0,00000	0,00000

Figure 82: Relevant elastic constants, Born effective charges and piezoelectric constants calculated using the PAW method with either LDA or GGA for GaN. Data are compared to results reported by Shimada *et. al.* [17], Karch *et. al.* [18] and Kim *et. al.* [19].

(Gpa)	C11+C12	C11-C12	C11	C12	C13	C33	C55	C66	B
AlN (PAW LDA)	554	263	408	146	115	383	116	131	217
AlN (PAW GGA)	514	259	386	128	105	356	115	129	201
Shimada (with corrections)			398	142	112	383	127	128	212
Shimada (without corrections)			474	106	68	478	147	184	-
Kim (FP-LMTO LDA)			398	140	127	382	96	129	218

	a (Å)	c (Å)	c/a	u	Zxx(B)	Zyy(B)	Zzz(B)	Z*(Al)	Zxx(N)	Zyy(N)	Zzz(N)	Z*(N)
AlN (PAW LDA)	3,0888	4,9549	1,6041	0,3820	2,34	2,34	2,54	2,41	-2,48	-2,48	-2,66	-2,54
AlN (PAW GAA)	3,1277	5,0119	1,6024	0,3815	2,36	2,37	2,54	2,42	-2,52	-2,52	-2,67	-2,57
Karch	3,143	5,1105	1,626	0,377	2,53	2,53	2,69	2,58				
Pesin												
exp	3,11	4,9800	1,6									
Shimada	3,112	4,995	1,605	0,3811			2,67					
Kim	3,06	4,91	1,6									

PIEZOELECTRIC TENSOR for field in x, y, z	(C/m^2)	AlN PAW LDA				
	XX	YY	ZZ	XY	YZ	ZX
x	0,00000	0,00000	0,00000	0,00000	0,00000	0,35406
y	0,00000	0,00000	0,00000	0,00000	0,35405	0,00000
z	0,25626	0,25626	-0,38612	0,00000	0,00000	0,00000

PIEZOELECTRIC TENSOR for field in x, y, z	(C/m^2)	AlN PAW GGA				
	XX	YY	ZZ	XY	YZ	ZX
x	0,00000	0,00000	0,00000	0,00000	0,00000	0,33055
y	0,00000	0,00000	0,00000	0,00000	0,33055	0,00000
z	0,26836	0,26836	-0,41731	0,00000	0,00000	0,00000

Figure 83: Relevant elastic constants, Born effective charges and piezoelectric constants calculated using the PAW method with either LDA or GGA for AlN. Data are compared to results reported by Shimada *et. al.* [17], Karch *et. al.* [18] and Kim *et. al.* [19].

(Gpa)	$C_{11}+C_{12}$	$C_{11}-C_{12}$	C_{11}	C_{12}	C_{13}	C_{33}	C_{55}	C_{66}	B
BN (PAW LDA)	1163	855	1009	154	56	1111	349	428	407
BN (PAW GGA)	1086	813	949	136	68	1029	335	407	386
Shimada (with corrections)			982	143	74	1077	388	424	401
Shimada (without corrections)			998	127	73	1076	397	436	402
Kim (FP-LMTO LDA)			987	143	70	1020	369	422	395

	a (Å)	c (Å)	c/a	u	Zxx(B)	Zyy(B)	Zzz(B)	Z*(B)	Zxx(N)	Zyy(N)	Zzz(N)	Z*(N)
BN (PAW LDA)	2,5241	4,1767	1,6547	0,3742	1,84	1,84	1,91	1,86	-1,83	-1,83	-1,90	-1,85
BN (PAW GAA)	2,5545	4,2247	1,6538	0,3743	1,87	1,87	1,95	1,90	-1,86	-1,86	-1,94	-1,89
Karch	2,531	4,1939	1,657	0,3751	1,86	1,86	1,96	1,89				
Pesin	2,521	4,1143	1,632									
exp (soma)	2,558	4,2280	1,656									
Shimada	2,534	4,191	1,654	0,3738			1,89					
Kim	2,54	4,17	1,64	0,375								

PIEZOELECTRIC TENSOR for field in x, y, z	(C/m^2)		BN PAW LDA			
	XX	YY	ZZ	XY	YZ	ZX
x	0,00000	0,00000	0,00000	0,00000	0,00000	0,61579
y	0,00000	0,00000	0,00000	0,00000	0,61577	0,00000
z	0,50589	0,50589	-1,03714	0,00000	0,00000	0,00000

PIEZOELECTRIC TENSOR for field in x, y, z	(C/m^2)		BN PAW GGA			
	XX	YY	ZZ	XY	YZ	ZX
x	0,00000	0,00000	0,00000	0,00000	0,00000	0,61805
y	0,00000	0,00000	0,00000	0,00000	0,61805	0,00000
z	0,52215	0,52215	-1,07309	0,00000	0,00000	0,00000

Figure 84: Relevant elastic constants, Born effective charges and piezoelectric constants calculated using the PAW method with either LDA or GGA for BN. Data are compared to results reported by Shimada *et. al.* [17], Karch *et. al.* [18] and Kim *et. al.* [19].

REFERENCES

[1] M. A. Morgan, *Millimeter-Wave MMICs and Applications*. PhD thesis, California Institute of Technology, 2003.

[2] "Online Magazine of Mitsubishi Electric Semiconductors." http://www.mitsubishielectric.com/.

[3] H. Morkoç, *Handbook of Nitride Semiconductors and Devices: Materials properties, physics and growth*. Wiley-VCH, 2008.

[4] S. Bloom, G. Harbeke, E. Meier, and I. B. Ortenburger, "Band Structure and Reflectivity of GaN," *Physica Status Solidi (B)*, vol. 66, no. 1, pp. 161–168, 1974.

[5] S. Jain, M. Willander, J. Narayan, and R. Overstraeten, "III-nitrides: Growth, characterization, and properties," *Journal of Applied Physics*, vol. 87, no. 3, 2000.

[6] P. Gibart, "Metal organic vapour phase epitaxy of GaN and lateral overgrowth," *Reports on Progress in Physics*, vol. 67, no. 5, p. 667, 2004.

[7] "Webpage of the Millimeter-Wave Electronics Group at the Department for Information Technology and Electrical Engineering (D-ITET) at ETH Zürich." "http://www.mwe.ee.ethz.ch/en/about-mwe-group/research/vision-and-aim/high-electron-mobility-transistors-hemt.html".

[8] T. Aggerstam, *Gallium nitride templates and its related materials for electronics and photonic devices*. PhD thesis, KTH - Royal Institute of Technology - Stockholm, 2008.

[9] C. Brundle, C. Evans, and S. Wilson, *Encyclopedia of Materials Characterization: Surfaces, Interfaces, Thin Films*. Materials Characterization Series, Butterworth-Heinemann, 1992.

[10] A. Ougazzaden, S. Gautier, T. Moudakir, Z. Djebbour, Z. Lochner, S. Choi, H. J. Kim, J. H. Ryou, R. D. Dupuis, and A. A. Sirenko, "Bandgap bowing in BGaN thin films," *Applied Physics Letters*, vol. 93, August 2008.

[11] S. Gautier, C. Sartel, S. O. S. Hamady, N. Maloufi, J. Martin, F. Jomard, and A. Ougazzaden, "MOVPE growth study of $B_xGa_{(1-x)}N$ on GaN template substrate," *Superlattices and Microstructures*, vol. 40, pp. 233–238, October-December 2006.

[12] S. Gautier, *Élaboration par MOVPE des nouveaux matériaux B(Ga,Al)N pour les applications dans l'Ultra Violet et l'électronique de puissance*. PhD thesis, Université Paul Verlaine - Metz, 2007.

[13] S. Gautier, G. Patriarche, T. Moudakir, M. Abid, G. Orsal, K. Pantzas, D. Troadec, A. Soltani, L. Largeau, O. Mauguin, and A. Ougazzaden, "Deep structural analysis of novel BGaN material layers grown by MOVPE," *Journal of Crystal Growth*, vol. 315, pp. 288–291, Jan 2011.

[14] T. Baghdadli, S. Ould Saad Hamady, S. Gautier, T. Moudakir, B. Benyoucef, and A. Ougazzaden, "Electrical and structural characterizations of BGaN thin films grown by metal-organic vapor-phase epitaxy," *Physica Status Solidi (C)*, vol. 6, no. S2, pp. S1029–S1032, 2009.

[15] T. Palacios, S. Rajan, A. Chakraborty, S. Heikman, S. Keller, S. DenBaars, and U. K. Mishra, "InGaN back-barriers to increase the confinement of the 2DEG in AlGaN/GaN HEMTs," in *ONR/CANE Review*, 2005.

[16] P. Q. Miraglia, E. A. Preble, A. M. Roskowski, S. Einfeldt, and R. F. Davis, "Helical-type surface defects in GaN thin films epitaxially grown on GaN templates at reduced temperatures," *Journal of Crystal Growth*, vol. 253, pp. 16–25, June 2003.

[17] K. Shimada, T. Sota, K. Suzuki, and H. Okumura, "First-Principles Study on Piezoelectric Constants in Strained BN, AlN, and GaN," *Japanese Journal of Applied Physics*, vol. 37, pp. L1421–L1423, December 1998.

[18] K. Karch and F. Bechstedt, "Ab initio lattice dynamics of BN and AIN: Covalent versus ionic forces," *Physical Review B*, vol. 56, pp. 7404–7415, September 1997.

[19] K. Kim, W. R. L. Lambrecht, and B. Segall, "Elastic constants and related properties of tetrahedrally bonded BN, AlN, GaN, and InN," *Physical Review B*, vol. 53, June 1996.

[20] M. Grundmann, *The Physics of Semiconductors*. Springer, 2010.

[21] J. Golio and J. Golio, *The RF and microwave handbook*. No. vol. 1 in The RF and Microwave Handbook, CRC Press, 2008.

[22] S. Adachi, *Properties of Group-IV, III-V and II-VI Semiconductors*. Wiley Series in Materials for Electronic & Optoelectronic Applications, Wiley, 2005.

[23] U. K. Mishra, S. Likun, T. E. Kazior, and Y.-F. Wu, "GaN-Based RF Power Devices and Amplifiers," in *Proc. IEEE*, vol. 96, pp. 287–305, 2008.

[24] J. Piprek, *Nitride Semiconductor Devices: Principles and Simulation*. Wiley, 2007.

[25] Y. F. Wu, M. Moore, A. Saxler, T. Wisleder, and P. Parikh, "40-W/mm Double Field-plated GaN HEMTs," *Device Research Conference, 2006 64th*, pp. 151–152, June 2006.

[26] D. Fanning, A. Balistreri, E. Beam III, K. Decker, S. Evans, R. Eye, W. Gaiewski, T. Nagle, P. Saunier, and H.-Q. Tserng, "High Voltage GaAs pHEMT Technology for S-band High Power Amplifiers," in *Proc. CS Mantech*, p. 173, May 2007.

[27] J. Chung, W. Hoke, E. Chumbes, and T. Palacios, "AlGaN/GaN HEMT With 300-GHz f_{max}," *IEEE Electron Device Letters*, vol. 31, no. 3, pp. 195–197, 2010.

[28] T. Palacios, A. Chakraborty, S. Rajan, C. Poblenz, S. Keller, S. P. DenBaars, J. S. Speck, and U. K. Mishra, "High-power AlGaN/GaN HEMTs for Ka-band applications," *IEEE Electron Device Letters*, vol. 26, pp. 781–783

[29] G. Simin, X. Hu, A. Tarakji, J. Zhang, A. Koudymov, S. Saygi, J. Yang, A. Khan, M. Shur, and R. Gaska, "AlGaN/InGaN/GaN double heterostructure field-effect transistor," *Japanese Journal of Applied Physics*, vol. 40, pp. L1142–L1144, November 2001.

[30] L. Shen, S. Heikman, B. Moran, R. Coffie, N. Zhang, D. Buttari, I. Smorchkova, S. Keller, S. DenBaars, and U. Mishra, "AlGaN/AlN/GaN high-power microwave HEMT," *IEEE Electron Device Letters*, vol. 22, pp. 457–459, October 2001.

[31] I. Smorchkova, S. Keller, S. Heikman, C. Elsass, B. Heying, P. Fini, J. Speck, and U. Mishra, "Two-dimensional electron-gas AlN/GaN heterostructures with extremely thin AlN barriers," *Applied Physics Letters*, vol. 77, pp. 3998–4000, December 2000.

[32] S. Rajan, A. Chini, M. H. Wong, J. S. Speck, and U. K. Mishra, "N-polar GaN/AlGaN/GaN high electron mobility transistors," *Journal of Applied Physics*, vol. 102, March 2007.

[33] J. Kuzmik, A. Kostopoulos, G. Konstantinidis, J. Carlin, A. Georgakilas, and D. Pogany, "InAIN/GaN HEMTs: A first insight into technological optimization," *IEEE Transactions on Electron Devices*, vol. 53, pp. 422–426, March 2006.

[34] H. Sun, A. R. Alt, H. Benedickter, E. Feltin, J. F. Carlin, M. Gonschorek, N. R. Grandjean, and C. R. Bolognesi, "205-GHz (Al,In)N/GaN HEMTs," *IEEE Electron Device Letters*, vol. 31, pp. 957–959, September 2010.

[35] S. Nakamura, T. Mukai, and M. Senoh, "Candela-class high-brightness InGaN/AlGaN double-heterostructure blue-light-emitting diode," *Applied Physics Letters*, vol. 64, pp. 1687–1689, March 1994.

[36] H. Morkoc, S. Strite, G. B. Gao, M. E. Lin, B. Sverdlov, and M. Burns, "Large-bandgap SiC, III-V nitride, and II-VI ZnSe-based semiconductor device technologies," *Journal of Applied Physics*, vol. 76, pp. 1363–1398, August 1994.

[37] R. J. Trew, "Wide bandgap transistor amplifiers for improved performance microwave power and radar applications," in *Proc. MIKON-2004 Microwaves, Radar and Wireless Communications 15th Int. Conf*, vol. 1, pp. 18–23, 2004.

[38] O. Ambacher, J. Smart, J. Shealy, N. Weimann, K. Chu, M. Murphy, W. Schaff, L. Eastman, R. Dimitrov, L. Wittmer, M. Stutzmann, W. Rieger, and J. Hilsenbeck, "Two-dimensional electron gases induced by spontaneous and piezoelectric polarization charges in N- and Ga-face AlGaN/GaN heterostructures," *Journal of Applied Physics*, vol. 85, pp. 3222–3233, March 1999.

[39] W. R. Deal, "Solid-state amplifiers for terahertz electronics," in *Proc. IEEE MTT-S Int. Microwave Symp. Digest (MTT)*, pp. 1122–1125, 2010.

[40] S. T. Allen, W. L. Pribble, R. A. Sadler, T. S. Alcorn, Z. Ring, and J. W. Palmour, "Progress in high power SiC microwave MESFETs," in *Proc. IEEE MTT-S Int. Microwave Symp. Digest*, vol. 1, pp. 321–324, 1999.

[41] N. Singh, B. P. Wagner, D. J. Knuteson, M. E. Aumer, A. Berghmans, D. Thomson, and D. Kahler, "Semiconductor Heterojunction Device Based on SiC." US Patent No.: US 7,855,108 B2, December 2010.

[42] F. Bernardini, V. Fiorentini, and D. Vanderbilt, "Spontaneous polarization and piezoelectric constant of III-V nitrides," *Physical Review B*, vol. 56, no. 16, pp. 10024–10027, 1997.

[43] H. P. Maruska and J. J. Tietjen, "Preparation and properties of vapor-deposited single-crystal GaN," *Applied Physics Letters*, vol. 15, no. 10, p. 327, 1969.

[44] P. B. Perry and R. F. Rutz, "The optical absorption edge of single-crystal AIN prepared by a close-spaced vapor process," *Applied Physics Letters*, vol. 33, no. 4, pp. 319–321, 1978.

[45] K. Osamura, S. Naka, and Y. Murakami, "Preparation and optical properties of $Ga_{1-x}In_xN$ thin films," *Journal of Applied Physics*, vol. 46, no. 8, pp. 3432–3437, 1975.

[46] M. Trejo, G. H. Jessen, K. D. Chabak, J. K. Gillespie, A. Crespo, M. Kossler, V. Trimble, D. Langley, E. R. Heller, B. Claflin, D. E. Walker, B. Poling, R. Gilbert, G. D. Via, J. Hoelscher, J. Roussos, F. Ejeckam, and J. Zimmer, "Progress towards III-nitrides HEMTs on free-standing diamond substrates for thermal management," *Physica Status Solidi (A)*, vol. 208, no. 2, pp. 439–444, 2011.

[47] G. Martin, A. Botchkarev, A. Rockett, and H. Morkoc, "Valence-band discontinuities of wurtzite GaN, AlN, and InN heterojunctions measured by x-ray photoemission spectroscopy," *Applied Physics Letters*, vol. 68, pp. 2541–2543, April 1996.

[48] R. Dingle, H. L. Stormer, A. C. Gossard, and W. Wiegmann, "Electron mobilities in modulation-doped semiconductor heterojunction superlattices," *Applied Physics Letters*, vol. 33, no. 7, pp. 665–667, 1978.

[49] T. Mimura, "The early history of the high electron mobility transistor (HEMT)," *IEEE Transaction on Microwave Theory and Techniques*, vol. 50, no. 3, pp. 780–782, 2002.

[50] M. A. Khan, A. Bhattarai, J. N. Kuznia, and D. T. Olson, "High electron mobility transistor based on a $GaN - Al_xGa_{1-x}N$ heterojunction," *Applied Physics Letters*, vol. 63, no. 9, pp. 1214–1215, 1993.

[51] M. A. Khan, J. N. Kuznia, J. M. Vanhove, N. Pan, and J. Carter, "Observation of a two-dimensional electron gas in low pressure metalorganic chemical vapor deposited $GaN - Al_xGa_{1-x}N$ heterojunctions," *Applied Physics Letters*, vol. 60, pp. 3027–3029, June 1992.

[52] J. I. Pankove, S. Bloom, and G. Harbeke, "Optical-properties of GaN," *RCA Review*, vol. 36, no. 1, pp. 163–176, 1975.

[53] C. Wetzel, T. Suski, J. W. Ager, E. R. Weber, E. E. Haller, S. Fischer, B. K. Meyer, R. J. Molnar, and P. Perlin, "Pressure induced deep gap state of oxygen in GaN," *Physical Review Letters*, vol. 78, pp. 3923–3926, May 1997.

[54] J. P. Ibbetson, P. T. Fini, K. D. Ness, S. P. DenBaars, J. S. Speck, and U. K. Mishra, "Polarization effects, surface states, and the source of electrons in AlGaN/GaN heterostructure field effect transistors," *Applied Physics Letters*, vol. 77, pp. 250–252, July 2000.

[55] B. Jogai, "Influence of surface states on the two-dimensional electron gas in AlGaN/GaN heterojunction field-effect transistors," *Journal of Applied Physics*, vol. 93, pp. 1631–1635, February 2003.

[56] G. Koley and M. G. Spencer, "On the origin of the two-dimensional electron gas at the AlGaN/GaN heterostructure interface," *Applied Physics Letters*, vol. 86, p. 042107, January 2005.

[57] Y. Ohno, T. Nakao, S. Kishimoto, K. Maezawa, and T. Mizutani, "Effects of surface passivation on breakdown of AlGaN/GaN high-electron-mobility transistors," *Applied Physics Letters*, vol. 84, pp. 2184–2186, March 2004.

[58] O. Ambacher, J. Smart, J. R. Shealy, N. G. Weimann, K. Chu, M. Murphy, W. J. Schaff, L. F. Eastman, R. Dimitrov, L. Wittmer, M. Stutzmann, W. Rieger, and J. Hilsenbeck, "Two-dimensional electron gases induced by spontaneous and piezoelectric polarization charges in N- and Ga-face AlGaN/GaN heterostructures," *Journal of Applied Physics*, vol. 85, no. 6, pp. 3222–3233, 1999.

[59] R. Dimitrov, M. Murphy, J. Smart, W. Schaff, J. R. Shealy, L. F. Eastman, O. Ambacher, and M. Stutzmann, "Two-dimensional electron gases in Ga-face and N-face AlGaN/GaN heterostructures grown by plasma-induced molecular beam epitaxy and metalorganic chemical vapor deposition on sapphire," *Journal of Applied Physics*, vol. 87, no. 7, pp. 3375–3380, 2000.

[60] G. Stringfellow, *Organometallic Vapor-Phase Epitaxy, Second Edition: Theory and Practice*. Academic Press, 2 ed., 1998.

[61] A. Mircea, A. Ougazzaden, and R. Mellet, "Very uniform epitaxy," *Progress in Crystal Growth and Characterization*, vol. 19, no. 1–2, pp. 39–49, 1989.

[62] B. Monemar, "Fundamental energy gap of GaN from photoluminescence excitation spectra," *Physical Review B*, vol. 10, pp. 676–681, 07 1974.

[63] W. Grieshaber, E. F. Schubert, I. D. Goepfert, R. F. Karlicek, M. J. Schurman, and C. Tran, "Competition between band gap and yellow luminescence in GaN and its relevance for optoelectronic devices," *Journal of Applied Physics*, vol. 80, pp. 4615–4620, Oct 1996.

[64] R. Armitage, Q. Yang, and E. R. Weber, "Analysis of the carbon-related 'blue' luminescence in GaN," *Journal of Applied Physics*, vol. 97, p. 073524, Apr 2005.

[65] Y. H. Kwon, S. K. Shee, G. H. Gainer, G. H. Park, S. J. Hwang, and J. J. Song, "Time-resolved study of yellow and blue luminescence in Si- and Mg-doped GaN," *Applied Physics Letters*, vol. 76, pp. 840–842, Feb 2000.

[66] J. L. Bradshaw, R. P. Devaty, W. J. Choyke, and R. L. Messham, "Fabry-Perot cavity oscillations of an $Al_xGa_{1-x}As$ photoluminescence spectrum," *Applied Optics*, vol. 29, pp. 2367–2369, Jun 1990.

[67] L. Siozade, J. Leymarie, P. Disseix, A. Vasson, M. Mihailovic, N. Grandjean, M. Leroux, and J. Massies, "Modelling of thermally detected optical absorption and luminescence of (In,Ga)N/GaN heterostructures," *Solid State Communications*, vol. 115, pp. 575–579, 8 2000.

[68] G. Hernandez, *Fabry-Perot Interferometers*. Cambridge Studies in Modern Optics, Cambridge University Press, 1988.

[69] L. J. van der Pauw, "A Method of Measuring the Resistivity and Hall Coefficient on Lamellae of Arbitrary Shape," *Philips Tech. Rev.*, vol. 20, no. 8, pp. 220–224, 1958.

[70] X. Garros, C. Leroux, and J.-L. Autran, "An efficient model for accurate capacitance-voltage characterization of high-k gate dielectrics using a mercury probe," *Electrochemical and Solid-State Letters*, vol. 5, no. 3, pp. F4–F6, 2002.

[71] R. K. Hiremath, B. G. Mulimani, M. K. Rabinal, and I. M. Khazi, "Electrical characterization of a phenylacetylene-modified silicon surface via mercury probe," *Journal of Physics: Condensed Matter*, vol. 19, no. 44, p. 446003, 2007.

[72] A. V. Nabok, A. K. Hassan, A. K. Ray, and G. N. Toldi, "Electrical study of polyelectrolyte self-assembled films using mercury probe," *Materials Science and Engineering: C*, vol. 22, pp. 387–391, 12 2002.

[73] D. Schroder, *Semiconductor Material and Device Characterization*. Wiley, 2006.

[74] E. Nicollian and J. Brews, *MOS (Metal Oxide Semiconductor) Physics and Technology*. Wiley Classics Library, Wiley, 2002.

[75] V. K. Gupta, C. C. Wamsley, M. W. Koch, and G. W. Wicks, "Molecular beam epitaxy growth of boron-containing nitrides," *Journal of Vacuum Science and Technology B*, vol. 17, pp. 1246–1248, May-June 1999.

[76] S. Watanabe, T. Takano, K. Jinen, J. Yamamoto, and H. Kawanishi, "Refractive indices of $B_xAl_{1-x}N$ (x = 0–0.012) and $B_yGa_{1-y}N$ (y = 0–0.023) epitaxial layers in ultraviolet region," *Physica Status Solidi (C)*, vol. 0, no. 7, pp. 2691–2694, 2003.

[77] S. Sakai, Y. Ueta, and Y. Terauchi, "Band gap energy and band lineup of III-V alloy semiconductors incorporating nitrogen and boron," *Japanese Journal of Applied Physics*, vol. 32, pp. 4413–4417, October 1993.

[78] V. Vezin, S. Yatagai, H. Shiraki, and S. Uda, "Growth of $Ga_{1-x}B_xN$ by molecular beam epitaxy," *Japanese Journal of Applied Physics*, vol. 36, pp. L1483–L1485, November 1997.

[79] S. Ould Saad Hamady, T. Baghdadli, S. Gautier, M. Bouchaour, J. Martin, and A. Ougazzaden, "Raman scattering study of $B_xGa_{1-x}N$ growth on AlN template substrate," *Physica Status Solidi (C)*, vol. 5, no. 9, pp. 3051–3053, 2008.

[80] K. H. Ploog and O. Brandt, "Doping of group III nitrides," *J. Vac. Sci. Technol. A*, vol. 16, pp. 1609–1614, 05 1998.

[81] D. D. Koleske, A. E. Wickenden, R. L. Henry, and M. E. Twigg, "Influence of MOVPE growth conditions on carbon and silicon concentrations in GaN," *Journal of Crystal Growth*, vol. 242, pp. 55–69, 7 2002.

[82] J. L. Lyons, A. Janotti, and C. G. Van de Walle, "Carbon impurities and the yellow luminescence in GaN," *Applied Physics Letters*, vol. 97, p. 152108, October 2010.

[83] I.-H. Tan, G. L. Snider, L. D. Chang, and E. L. Hu, "A self-consistent solution of Schrödinger-Poisson equations using a nonuniform mesh," *Journal of Applied Physics*, vol. 68, pp. 4071–4076, October 1990.

[84] E. Schrödinger, "Quantisierung als eigenwertproblem," *Annalen der Physik*, vol. 385, no. 13, pp. 437–490, 1926.

[85] C. M. Krowne, "Semiconductor heterostructure nonlinear poisson equation," *Journal of Applied Physics*, vol. 65, pp. 1602–1614, February 1989.

[86] O. Kelekci, S. B. Lisesivdin, S. Ozcelik, and E. Ozbay, "Numerical optimization of In-mole fractions and layer thicknesses in $Al_xGa_{1-x}N$/AlN/GaN high electron mobility transistors with InGaN back barriers," *Physica B: Condensed Matter*, vol. 406, pp. 1513–1518, Apr 2011.

[87] Y. Deng, V. Adivarahan, and A. Khan, "Selective doping and optimization of InGaN channel and InGaN backbarrier in deep submicron GaN heterojunction field effect transistor with a recessed gate," *Semiconductor Device Research Symposium, 2007 International*, pp. 1–2, 12-14 Dec. 2007.

[88] S. Heikman, S. Keller, S. P. DenBaars, and U. K. Mishra, "Growth of Fe doped semi-insulating GaN by metalorganic chemical vapor deposition," *Applied Physics Letters*, vol. 81, pp. 439–441, July 2002.

[89] C. Poblenz, P. Waltereit, S. Rajan, S. Heikman, U. K. Mishra, and J. S. Speck, "Effect of carbon doping on buffer leakage in AlGaN/GaN high electron mobility transistors," *Journal of Vacuum Science and Technology B*, vol. 22, pp. 1145–1149, May-June 2004.

[90] H. Yu, S. B. Lisesivdin, B. Bolukbas, O. Kelekci, M. K. Ozturk, S. Ozcelik, D. Caliskan, M. Ozturk, H. Cakmak, P. Demirel, and E. Ozbay, "Improvement of breakdown characteristics in AlGaN/GaN/$Al_xGa_{1-x}N$ HEMT based on a grading $Al_xGa_{1-x}N$ buffer layer," *Physica Status Solidi (A)*, vol. 207, no. 11, pp. 2593–2596, 2010.

[91] A. P. Zhang, L. B. Rowland, E. B. Kaminsky, V. Tilak, J. C. Grande, J. Teetsov, A. Vertiatchikh, and L. F. Eastman, "Correlation of device performance and defects in AlGaN/GaN high-electron mobility transistors," *Journal of Electronic Materials*, vol. 32, pp. 388–394, May 2003.

[92] R. Chu, Y. Zhou, J. Liu, D. Wang, K. J. Chen, and K. M. Lau, "AlGaN-GaN double-channel HEMTs," *IEEE Transactions on Electron Devices*, vol. 52, no. 4, pp. 438–446, 2005.

[93] Y. Cordier, F. Semond, M. Hugues, F. Natali, P. Lorenzini, H. Haas, S. Chenot, M. Laugt, O. Tottereau, P. Vennegues, and J. Massies, "AlGaN/GaN/AlGaN DH-HEMTs grown by MBE on Si(111)," *Journal of Crystal Growth*, vol. 278, pp. 393–396, May 2005.

[94] E. Bahat-Treidel, O. Hilt, F. Brunner, J. Würfl, and G. Tränkle, "AlGaN/GaN/AlGaN double heterojunction HEMTs on n-type SiC substrates," *Physica Status Solidi (C)*, vol. 7, no. 10, pp. 2408–2411, 2010.

[95] C. Q. Chen, J. P. Zhang, V. Adivarahan, A. Koudymov, H. Fatima, G. Simin, J. Yang, and M. A. Khan, "AlGaN/GaN/AlGaN double heterostructure for high-power III-N field-effect transistors," *Applied Physics Letters*, vol. 82, pp. 4593–4595, June 2003.

[96] N. Okamoto, K. Hoshino, N. Hara, M. Takikawa, and Y. Arakawa, "MOCVD-grown InGaN-channel HEMT structures with electron mobility of over $1000cm^2/V.s$," *Journal of Crystal Growth*, vol. 272, pp. 278–284, December 2004.

[97] S. Gökden, R. Tülek, A. Teke, J. H. Leach, Q. Fan, J. Xie, Ü. Özgür, H. Morkoç, S. B. Lisesivdin, and E. Özbay, "Mobility limiting scattering mechanisms in nitride-based two-dimensional heterostructures with the InGaN channel," *Semiconductor Science and Technology*, vol. 25, p. 045024, April 2010.

[98] K. H. Lee, P. C. Chang, S. J. Chang, Y. K. Su, and C. L. Yu, "AlGaN/GaN high electron mobility transistors based on InGaN/GaN multiquantum-well structures," *Applied Physics Letters*, vol. 96, p. 212105, May 2010.

[99] T. Palacios, A. Chakraborty, S. Heikman, S. Keller, S. DenBaars, and U. Mishra, "AlGaN/GaN high electron mobility transistors with InGaN back-barriers," *IEEE Electron Device Letters*, vol. 27, pp. 13–15, January 2006.

[100] J. Liu, Y. Zhou, J. Zhou, K. M. Lau, and K. J. Chen, "AlGaN/GaN/InGaN/GaN DH-HEMTs with an InGaN notch for enhanced carrier confinement," *IEEE Electron Device Letters*, vol. 27, pp. 10–12, January 2006.

[101] J. Liu, Y. Zhou, J. Zhu, Y. Cai, K. M. Lau, and K. J. Chen, "DC and RF Characteristics of AlGaN/GaN/InGaN/GaN Double-Heterojunction HEMTs," *IEEE Transactions on Electron Devices*, vol. 54, pp. 2–10, January 2007.

[102] K. Shimada, T. Sota, and K. Suzuki, "First-principles study on electronic and elastic properties of BN, AlN, and GaN," *Journal of Applied Physics*, vol. 84, pp. 4951–4958, November 1998.

[103] F. Bernardini and V. Fiorentini, "Nonlinear macroscopic polarization in III-V nitride alloys," *Physical Review B*, vol. 64, p. 085207, August 2001.

[104] F. Bechstedt, U. Grossner, and J. Furthmuller, "Dynamics and polarization of group-III nitride lattices: A first-principles study," *Physical Review B*, vol. 62, pp. 8003–8011, September 2000.

[105] T. Matsuoka, N. Yoshimoto, T. Sasaki, and A. Katsui, "Wide-gap semiconductor InGaN and InGaAlN grown by MOVPE," *Journal of Electronic Materials*, vol. 21, pp. 157–163, February 1992.

[106] S. Nakamura, "GaN growth using GaN buffer layer," *Japanese Journal of Applied Physics*, vol. 30, pp. L1705–L1707, October 1991.

[107] S. M. Olaizola, S. T. Pendlebury, J. P. O'Neill, D. J. Mowbray, A. G. Cullis, M. S. Skolnick, P. J. Parbrook, and A. M. Fox, "Influence of GaN barrier growth temperature on the photoluminescence of InGaN/GaN heterostructures," *Journal of Physics D - Applied Physics*, vol. 35, pp. 599–603, April 2002.

[108] Y. Wang, X. J. Pei, Z. G. Xing, L. W. Guo, H. Q. Jia, H. Chen, and J. M. Zhou, "Effects of barrier growth temperature ramp-up time on the photoluminescence of InGaN/GaN quantum wells," *Journal of Applied Physics*, vol. 101, p. 033509, February 2007.

[109] C. Chen, H. Liu, D. Steigerwald, W. Imler, C. Kuo, M. Craford, M. Ludowise, S. Lester, and J. Amano, "A study of parasitic reactions between NH_3 and TMGa or TMAI," *Journal of Electronic Materials*, vol. 25, pp. 1004–1008, 1996.

[110] X. H. Wu, C. R. Elsass, A. Abare, M. Mack, S. Keller, P. M. Petroff, S. P. DenBaars, J. S. Speck, and S. J. Rosner, "Structural origin of V-defects and correlation with localized excitonic centers in InGaN/GaN multiple quantum wells," *Applied Physics Letters*, vol. 72, pp. 692–694, 02 1998.

[111] M. C. Johnson, Z. Liliental-Weber, D. N. Zakharov, D. E. McCready, R. J. Jorgenson, J. Wu, W. Shan, and E. D. Bourret-Courchesne, "Investigation of microstructure and V-defect formation in $In_xGa_{1-x}N$/GaN MQW grown using temperature-gradient metalorganic chemical vapor deposition," *Journal of Electronic Materials*, vol. 34, pp. 605–611, May 2005.

[112] J. P. Liu, J. H. Ryou, D. Yoo, Y. Zhang, J. Limb, C. A. Horne, S. C. Shen, R. D. Dupuis, A. D. Hanser, E. A. Preble, and K. R. Evans, "III-nitride heterostructure field-effect transistors grown on semi-insulating GaN substrate without regrowth interface charge," *Applied Physics Letters*, vol. 92, no. 13, p. 133513, 2008.

[113] M. A. Reshchikov and H. Morkoc, "Luminescence properties of defects in GaN," *Journal of Applied Physics*, vol. 97, pp. 061301–95, 03 2005.

[114] M. Tchounkeu, O. Briot, B. Gil, J. P. Alexis, and R.-L. Aulombard, "Optical properties of GaN epilayers on sapphire," *Journal of Applied Physics*, vol. 80, no. 9, pp. 5352–5360, 1996.

[115] M. Boucherit, *Etude et réalisation de dispositifs hyperfréquences sur matériaux grand gap : Diode à effet tunnel résonant $Al_xGa_{1-x}N/GaN/Al_xGa_{1-x}N$ et Transistor HEMT boré à base de nitrure de gallium.* PhD thesis, Université des Sciences et Technologies de Lille 1 - Lille, 2012.

[116] L. Shen, R. Coffie, D. Buttari, S. Heikman, A. Chakraborty, A. Chini, S. Keller, S. P. DenBaars, and U. K. Mishra, "High-power polarization-engineered

GaN/AlGaN/GaN HEMTs without surface passivation," *IEEE Electron Device Letters*, vol. 25, pp. 7–9, Jan 2004.

[117] R. Coffie, D. Buttari, S. Heikman, S. Keller, A. Chini, L. Shen, and U. K. Mishra, "p-capped GaN-AlGaN-GaN high-electron mobility transistors (HEMTs)," *IEEE Electron Device Letters*, vol. 23, pp. 588–590, Oct 2002.

[118] K. Onodera, K. Nishimura, S. Aoyama, S. Sugitani, Y. Yamane, and M. Hirano, "Extremely low-noise performance of GaAs MESFET's with wide-head T-shaped gate," *IEEE Transactions on Electron Devices*, vol. 46, pp. 310–319, Feb 1999.

[119] E. Y. Chang, K. C. Lin, E. H. Liu, C. Y. Chang, T. H. Chen, and J. Chen, "Submicron T-shaped gate HEMT fabrication using deep-UV lithography," *IEEE Electron Device Letters*, vol. 15, no. 8, pp. 277–279, Aug. 1994.

[120] M. Mattalah, A. Soltani, J. C. Gerbedoen, A. Ahaitouf, N. Defrance, Y. Cordier, and J. C. De Jaeger, "Analysis of the SiO_2/Si_3N_4 passivation bilayer thickness on the rectifier behavior of AlGaN/GaN HEMTs on (111) silicon substrate," *Physica Status Solidi (C)*, vol. 9, no. 3-4, pp. 1083–1087, 2012.

[121] H. Kim, F. Fälth, and T. Andersson, "Unintentional incorporation of B, As, and O impurities in GaN grown by molecular beam epitaxy," *Journal of Electronic Materials*, vol. 30, no. 10, pp. 1343–1347, 2001-10-01.

[122] G. H. Jessen, R. C. Fitch, J. K. Gillespie, G. Via, A. Crespo, D. Langley, D. J. Denninghoff, M. Trejo, and E. R. Heller, "Short-channel effect limitations on high-frequency operation of AlGaN/GaN HEMTs for T-Gate devices," *IEEE Transactions on Electron Devices*, vol. 54, pp. 2589–2597, Oct 2007.

[123] S. Gautier, G. Orsal, T. Moudakir, N. Maloufi, F. Jomard, M. Alnot, Z. Djebbour, A. Sirenko, M. Abid, K. Pantzas, I. Ferguson, P. Voss, and A. Ougazzaden, "Metal-organic vapour phase epitaxy of BInGaN quaternary alloys and characterization of boron content," *Journal of Crystal Growth*, vol. 312, no. 5, pp. 641 – 644, 2010.

VITA

Vinod Ravindran was born in Sucy-en-Brie, France. He received his engineering degree from Supélec (Paris, France) in 2007. He also holds a M.S. specialized in Opto-electronics from the University of Metz (Metz, France 2007) and a B.S. in Fundamental Physics from the University of Orsay (Paris, France 2006).

He received his Ph.D. from the Université of Lorraine in 2012, and his Ph.D. in Electrical and Computer Engineering from the Georgia Institute of Technology in 2013. His doctoral research was conducted on the European campus of Georgia Tech, Georgia Tech Lorraine (Metz, France) and was a joint research program with the French company Thales, a European leader in electronic systems for defense, aerospace and security. His research involved design and simulation of high electron mobility transistors based on novel materials.